学位論文

Effects of Anchored Polymers on Biomembranes

(生体膜に対するグラフト高分子の効果)

平成25年7月博士（理学）申請

東京大学大学院理学系研究科
物理学専攻

巫 浩
Wu Hao

The University of Tokyo

Doctoral Thesis

Effects of Anchored Polymers on Biomembranes

Author:
Hao Wu

Supervisor:
Hiroshi Noguchi

A thesis submitted in fulfilment of the requirements
for the degree of
Doctor of Philosophy

in

Department of Physics
Graduate School of Science

September 2013

Declaration of Authorship

I, Hao Wu, declare that this thesis titled, 'Effects of Anchored Polymers on Biomembranes' and the work presented in it are my own. I confirm that:

- This work was done wholly or mainly while in candidature for a research degree at this University.
- Where any part of this thesis has previously been submitted for a degree or any other qualification at this University or any other institution, this has been clearly stated.
- Where I have consulted the published work of others, this is always clearly attributed.
- Where I have quoted from the work of others, the source is always given. With the exception of such quotations, this thesis is entirely my own work.
- I have acknowledged all main sources of help.
- Where the thesis is based on work done by myself jointly with others, I have made clear exactly what was done by others and what I have contributed myself.

Signed: Wu Hao

Date: 06/09/2013

"Be curious. And however difficult life may seem, there is always something you can do and succeed at. It matter that you dont just give up."

Stephen Hawking

Abstract

The entropic effects of anchored polymers on various mechanical properties of single and multi-component membranes are systematically studied using simulations of a meshless membrane model combined with anchored linear polymer chains. Polymer-induced bending rigidity and spontaneous curvature of membrane are first revisited. For the simplicity, a cylindrical shape of membrane are chosen to investigate these two mechanical properties for anchored ideal and excluded-volume polymer chains, respectively. Our results on membrane with anchored ideal polymer chains agree with the previous linear partition function method and Monte Carlo simulation well. Our results on membrane with anchored excluded-volume polymer chains are well consistent with a previous scaling theory in a low density region, but in a high density part there is a difference between our simulation and scaling theory, due to the limitation of Taylor expansion on a non-small quantity.

In this PhD thesis, we specially pay attention to the effect of anchored polymers on the edge of a patch of strip membrane, as well as the interfacial line between two coexisting domains, both the strip shape and the circular shape, for the first time. It is found that both ideal and excluded-volume polymer chains can reduce the line tension of membrane edges, but excluded-volume chains reduce the line tension more due to the steric repulsion. A 3D lattice polymer model is employed to calculate the reduced weight ratio of linear ideal chains in the middle part and at the edge part. Based on the lattice model. Based on the 3D lattice model, a mean field theory is proposed for the edge line tension reduced by grafting ideal chains, which well reproduces our simulation results. The interfacial line tension between different membrane domains is also reduced by anchored polymer chains, for the strip and circular domains. It leads to microdomain separation. Different cases for the interfacial tension reduction are compared between the domains with and without anchored polymer chains. It is found that without anchored polymers, two domain phases always tend to mix with the interfacial line tension decreasing. However, instead of the mixing of two phases as seen in typical binary fluids, densely anchored polymers can stabilize small domains. At some critical density of anchored polymer chains, an intermediate state before microdomain separation are confirmed in the simulation. It leads the domain boundary increase, but without the separation occurring.

Acknowledgements

I first deeply thank my supervisor, Hiroshi Noguchi, for his support and supervision during the three-year PhD study. He introduced me into this fascinating and promising biomembrane field composed of membranes with anchored polymers. I benefited a lot from his rich research experience and rigorous working attitude. He also helped me much in my life to make me adapt to Japanese life quickly. The completion of this thesis cannot be done without his help.

I also acknowledge Hayato Shiba, who almost becomes my elder brother in Japan. He afforded a part of the responsibility of my tutor when I just arrived at Japan. Through him I learnt about many Japanese traditions. When I am in trouble, he often can give me a solution. After I independently finished my whole PhD work, he friendly checked all the simulation results. Because he has many-year experience in simulation, his confirmation makes me more confident to my doctoral work.

Moreover, I also would like to thank Wenxing Nie and Eggel Thomas, for their patient listening to my calculations on statistical field theory of fluctuating membranes, as well as Kumano san for the informative discussion on Kosterlitz-Thouless phase transition. Special thanks to Weiqin Liu for his earnest help and encouragement when I was in trouble, and Yi Wang for his great technical support.

Additionally, I hope to express my gratitude to Jianshu Cao, Hans-Günther Döbereiner, Jean-Baptiste Fouriner, Gerhard Gompper, Raymond Kapral, Ji-Hyun Kim, Shigeyuki Komura, Michael Kozlov, Yoshifumi Noguchi, Masaki Oshikawa, Pillip Pincus, Zhanchun Tu, Micheal Wortis, Xintian Wu, Miho Yanagisawa, and Rosemary Zhang. I benefited much from their informative discussions, which expand my academic horizons, on various kinds of interesting scientific problems.

Importantly, I am thankful to a Monbukagakusho Scholarship from Japanese Ministry of Education, Culture, Sports, Science, and Technology (MEXT) for my three-year PhD study.

I am also grateful to our group secretaries, Matsushita san and Tsuji san, for their kind care and help during my three-year life in Japan. I also have a special acknowledgement for Ishida san's kind help and warm encouragement to my PhD study.

Thanks for our group students, Sakashita san, Tarama san, and Nakagawa san to accompany me in the lab during my short but pleasant reminding PhD time, specially for Sakashita san and Nakagawa san as my cheering squad appearing at the doctoral defense.

At last, I also want to thank all the others, whom I did not mention here, that helped me in many other ways to make my PhD study smooth.

Contents

Declaration of Authorship i

Abstract iii

Acknowledgements iv

List of Figures ix

1 Research Motivation 1

2 Biomembranes and Lipid Membranes 4
2.1 Introduction of biomembranes . . . 4
2.1.1 Structures of biomembranes . . . 6
2.1.2 Chemical components of biomembranes . . . 8
2.1.3 Structures and functions of lipid rafts . . . 9
2.2 Lipid membranes in lab . . . 13
2.2.1 Phase separation on multicomponent membranes . . . 13
2.2.1.1 Phase diagram on membranes of ternary components . . . 14
2.2.1.2 Dependence of line tension on temperature . . . 16
2.2.1.3 Effect of surface tension on miscibility temperature . . . 18
2.2.2 Micro-segregation triggered by PEG-anchored lipids . . . 19

3 Theory and Simulation of Membranes and Polymers 22
3.1 Theory of membranes . . . 22
3.1.1 Helfrich curvature elastic free energy . . . 23
3.1.2 Monge representation for a patch of small curvature surface . . . 24
3.2 Multi-scale simulation of membranes . . . 25
3.2.1 Atomistic Molecular Dynamics for nanometer scales . . . 27
3.2.2 Coarse-grained off-lattice models for mesoscopic scales . . . 28
3.2.2.1 Explicit solvent model . . . 29
3.2.2.2 Solvent free model . . . 29
3.2.3 Continuous surfaces constructed by dynamic triangulation . . . 31
3.3 Physics of polymers . . . 33
3.3.1 Ideal chains . . . 34

3.3.2 Excluded-volume chains . . . 35
3.3.3 Polymer mushroom and brush . . . 36
3.4 Polymer-induced mechanical properties of membranes . . . 36
3.4.1 Mechanical properties induced by a single polymer . . . 36
3.4.2 Mechanical properties induced by polymer mushroom . . . 38
3.4.3 Mechanical properties induced by polymer brush . . . 39

4 Simulation of Biomembranes 45
4.1 Meshless biomembrane model . . . 45
4.1.1 Soft-core repulsive potential . . . 46
4.1.2 Multi-body attraction for solvent free . . . 47
4.1.3 Aplanarity curvature potential . . . 49
4.1.4 Chemical affinity potential between different particles . . . 51
4.2 Model biomembranes with linear flexible polymers . . . 52
4.3 Our simulation method . . . 53
4.3.1 Leapfrog integration . . . 53
4.3.2 *NVT* ensemble . . . 54
4.3.3 Brownian dynamics simulation . . . 55
4.4 Radial distribution function of meshless membrane systems . . . 56

5 Bending Rigidity and Spontaneous Curvature of Biomembranes 59
5.1 Axial force method . . . 60
5.2 Anchored linear polymers simulation . . . 62
5.3 Collective effects of anchored polymer layer . . . 62
5.3.1 Polymer effects in mushroom region . . . 67
5.3.2 Comparisons with the scaling theory in brush region . . . 68
5.4 Vesicle formation from stretched cylindrical biomembranes . . . 70
5.5 Summary for cylindrical biomembranes . . . 71

6 Edge Line Tension of Biomembranes 74
6.1 Simulation of strip biomembranes with two edges . . . 74
6.1.1 The effective line tension on the edge . . . 74
6.1.2 Anchored polymers on the strip of biomembranes . . . 77
6.1.2.1 Polymer distribution on the strip of biomembranes . . . 77
6.1.2.2 End-to-end distance of anchored polymers on the strip of biomembranes . . . 77
6.2 Theory for anchored ideal chains . . . 80
6.2.1 Lattice model for a restricted ideal chain . . . 80
6.2.2 Mean field theory for strip biomembranes with ideal chains . . . 85
6.3 Summary for strip biomembranes . . . 88

7 Interfacial Line Tension and Microdomain Separation on Biomembranes 90
7.1 Interfacial line tension between two coexisting domains . . . 90
7.1.1 The case of a strip domain . . . 90
7.1.2 The case of a circular domain . . . 91
7.2 Polymer-induced microdomain separation . . . 94
7.3 Summary for multi-component biomembrane patch . . . 97

8 Summary and Perspectives **99**
8.1 Summary 99
8.2 Perspectives 100

A Details of Scaling Theory Calculation **103**

B Details of Mean Field Theory Calculation **107**

C Standard Virial Calculation of Pressure in Molecular Dynamics **108**

Bibliography **110**

List of Figures

2.1 Main Structures of Animal and Plant Cells . . . 7
2.2 Fluid Mosaic Model . . . 7
2.3 Planar Biomembrane Patch . . . 9
2.4 Chemical Components of Phospholipids . . . 10
2.5 Schematic Picture of Lipid Raft Microdomains . . . 12
2.6 Typical Phase Diagram for Ternary Vesicles Containing Mixtures of DOPC/PSM/Cholesterol . . . 15
2.7 Dependence of Line Tension on Temperature . . . 17
2.8 Shift in Miscibility Temperature as a Function of Applied Tension . . . 19

3.1 Illustration of Membrane Simulations at Different Scales . . . 26
3.2 Coarse-grained Three-bead Model for Bilayer . . . 30
3.3 Dynamic Triangulated Surface for Membranes . . . 32
3.4 Entropic Effect of a Single Polymer on Membrane . . . 37
3.5 Blob Picture of a Polymer Brush on a Flat Surface . . . 40
3.6 Blob Picture of a Polymer Brush on a Spherical Surface . . . 41

4.1 Schematic Picture of Meshless Membranes . . . 46
4.2 Schematic Picture of Curvature Potential . . . 49
4.3 Schematic Picture of Lipid Composition Distribution on Ternary Bilayer . . . 51
4.4 Schematic Picture of a Biomembrane Patch . . . 52
4.5 Discretized Calculation of Radial Distribution Function . . . 57
4.6 Radial Distribution Function of Tensionless Membranes . . . 58

5.1 Snapshot of Cylindrical Biomembranes . . . 60
5.2 Plot of Axial Force of Cylindrical Membranes . . . 63
5.3 End-to-end Distance of Anchored Polymers . . . 64
5.4 Plot of Time-dependent End-to-end Distance of Two Anchored Polymers 65
5.5 Spontaneous Curvature and Bending Rigidity of Cylindrical Membranes . . . 66
5.6 Comparison of Our Simulation and Linear Theory . . . 67
5.7 Comparison of Our Simulation, Linear Theory and Scaling Theory . . . 69
5.8 Formation Process from Stretched Cylindrical Biomembranes to Polymer-anchored Vesicle . . . 71
5.9 Number of Polymer-anchored Vesicles Formed from Stretched Cylindrical Biomembranes . . . 72

6.1 Snapshot of Strip Membranes . . . 75
6.2 Plot of Line Tension and Different Lengths of Membrane Edge . . . 75
6.3 Relation of Line Tension and Anchored Polymer Density . . . 76

6.4 Polymer Density Distribution on Strip Membranes 78
6.5 End-to-end Distance Distribution for Ideal Chains on Strip Membranes . 79
6.6 End-to-end Distance Distribution for Excluded-volume Chains on Strip Membranes 81
6.7 Cubic Lattice Model for Polymers 82
6.8 Schematic Picture of a Restricted Lattice Polymer 83
6.9 Probability Ratio of a Restricted Ideal Chain 85
6.10 Schematic Picture of Anchored Polymer Distribution on Strip Biomembranes 86
6.11 Relation of Excess Polymer Density and Mean Polymer Density 87

7.1 Snapshots of Strip Domain and Circular Domain 91
7.2 Interfacial Tension Between Two Coexisting Domains 92
7.3 Sequential Snapshots of Domain Phase Transition 95
7.4 Domain Size and Shape Transition 96
7.5 Polymer Fraction of Mother Domain 98

8.1 Lipid-Cholesterol Affinities in DOPC/eSM/Chol and DOPC/DPPC/Chol Lipid Membranes 101
8.2 Microdomain Separation in 3D Multicomponent Vesicle with Anchored Polymers 102

Dedicated to my parents

Chapter 1

Research Motivation

Since the unicellular organism occurs on the earth, membranes just have become an indispensable constituent part of cells. Cell membranes are very crucial to living organisms. They are the barriers of cells and ensure cells to be relatively isolated individuals but still able to exchange some materials between the inner sides and outer surroundings through some special ways due to the fancy properties of membranes. Membranes usually consist of lipid bilayers mosaicks built of various kinds of proteins and anchored bio-sugar chains. They are also key factors to determine the shapes of many kinds of cells. For example, the biconcave discoidal shape of healthy red blood cells is regarded as a result of minimization of the free energy of membranes under the area and volume constraints because red blood cells have no complex inner structures.

In the past two decades, the lipid domains on cell membranes have always been a hot research topic and received much attention from physicists, chemists, and biologists. Our knowledge on the heterogeneous structure of biomembranes has been developed from the primitive fluid mosaic model [1] to the modern raft model [2, 3] for decades. It is considered that membrane proteins are not randomly distributed in lipid membranes but concentrated in local microdomains, called lipid rafts, with diameter of $10 \sim 100$nm [4–7]. The raft contains high concentrations of glycosphingolipids and cholesterol, and play important roles on many intra- and inter-cellular processes including signal transaction and membrane protein trafficking.

In the last decade, the phase separation in multi-component lipid membranes has been intensively investigated in three-component systems of saturated and unsaturated phospholipids and cholesterol [8–15]. Lipid domains exhibit various interesting patterns in μm scale, which can be reproduced by theories and simulations. Various shapes of lipid domains can be also formed in air-water interface [16–18]. However, the formation mechanism of microdomains in $10 \sim 200$nm scale has not been understood so far [19]. In

the lipid rafts, glycolipids have glycan chains. Recently, network-shaped domains and small scattered domains are observed in lipid membranes with PEG-conjugated cholesterol [20]. The effects of anchored polymers have been well investigated in the case of uniformly anchoring on membranes, but the effects on the lipid domains and line tension are not well investigated. In this paper, we focus on the effects of anchored polymers on properties of biomenbranes, in particular on lipid domains.

It is well known that anchored polymers modify membrane properties [21]. The polymer grafting induces a positive spontaneous curvature C_0 of the membranes and increases the bending rigidity κ. These relations are analytically derived using the Green's function method and scaling method [21–25] and confirmed by Monte Carlo simulations [26–28]. Experimentally, the κ increase is measured by micropipette aspiration of liposomes [29]. Polymer decoration can enhance the stability of lipid membranes. PEG-conjugated lipids can reduce protein adsorption and adhesion on cellular surfaces, whereby PEG-coated liposomes can be used as a drug carrier in drug-delivery systems [30, 31].

When vesicles are formed from the self-assembly of surfactant molecules via micelle growth, the vesicle size is determined kinetically by the competition between the bending energy and the line tension energy of the membrane edge [32–38]. Recently, Bressel *et al.* reported that the addition of an amphiphilic copolymer induces the formation of larger vesicles [39]. A polymer-grafting-induced liposome-to-micelle transition is also observed [21, 40, 41]. The line tension of the membrane edge is considered to be reduced by polymer grafting, but it has not been systematically investigated so far. In this study, we simulate the line tension of the membrane edge for anchored ideal and excluded-volume chains and analytically investigate the polymer effects on the line tension for ideal chains.

In order to simulate the polymer-grafting effects on biomembranes, we employ one of the solvent-free meshless membrane models [42, 43]. Since we focus on the entropic effects of polymer chains, the detailed structures of the bilayer can be neglected, and thus the membranes can be treated as a curved surface. In the meshless model, a membrane particle represents a patch of bilayer membrane and membrane properties can be easily controlled., and the parameters related to mechanical properties of membranes can independently change and can be adjusted in a wide range.

Starting with the next chapter, we will illuminate the topic of my thesis as the following sequences: In Chapter 2, some basic knowledge on biomembrane and lipid domains are introduced and then some important biochemical experiments on multi-component membrane with and without anchored polymers are introduced. In Chapter 3, we introduce some theoretical background on membrane and polymers, and specially on the

principle of the effects of anchored polymers on membrane. In Chapter 4, a coarse-grained biomembrane model is described in detail, and by combination with polymers, it allows us to study various properties of biomembranes, that means, membranes with anchored polymers. In Chapter 5, the bending rigidity and spontaneous curvature of membrane with anchored polymers are revisited. Detailed investigations are performed on ideal and excluded-volume polymer chains, respectively. In Chapter 6, we simulate the effect of anchored polymers on the edge of strip membrane by a coarse-grained MD simulation, and we proposed a mean field theory to deal with the case of ideal polymer chains. It also can describe the mushroom region for excluded-volume polymer chains. In Chapter 7, our study emphasis is shifted to interesting phenomena of microdomain separation and the corresponding interfacial line tension. We focus on the domain shape transition and microdomain separation. Since the behavior of a membrane patch of phospholipids and cholesterol is sufficiently complex, traditional detailed simulations over time-scales are not sufficient to in investigate raft formation and structure [44]. Our coarse-grained biomembrane model can overcome this shortcoming. We also pay attention to the polymer fraction of the mother domain. In Chapter 8, a brief summary and future prospectives of this topic are discussed. Some calculation details of the scaling theory and the mean field theory are written in Appendix A and Appendix B, respectively. The pressure tensor calculation commonly used in Molecular Dynamics and its derivation are described in Appendix C. The main results of this thesis is based on our papers [45–47].

Chapter 2

Biomembranes and Lipid Membranes

Cellular membranes in living cells are a complex and compound system, including various kinds of proteins and different lipid compositions, all of which have two types of lipids of saturated and unsaturated in terms of the configuration of the double bonds. Usually cell membranes consist of three classes of amphipathic lipids: phospholipids, glycolipids, and Cholesterols, where glycolipids are "decorated" by bio-sugar chains called glycolipids [48, 49]. The amount of each depends upon the type of cell, but in the majority of cases phospholipids are the most abundant. There are also some transmembrane proteins with anchored bio-sugar chains called glycoproteins [48, 49].

Biomimetic membranes or vesicles are usually used as useful tools to exert a series of biochemical experiments in lab. Artificially the experimentalists decorate membranes with short polymer chains, e.g. PEG chains. This provides simple model systems of biomembranes to study some interesting characters of biomembranes.

2.1 Introduction of biomembranes

Cells are the basic consistent units of the structures and functions of human bodies and all the other living organisms. All the in vivo physiological functions and biochemical reactions are carried out on the basis of the material in the cell and its synthetic and excretive substrate (such as the collagen and proteoglycans in the cell gap). Every kind of cells in animals and plants are encapsuled by a piece of thin biomembrane, which is called cell membrane or plasma membrane. It physically divides the intracellular cytoplasm and the extracellular environment of cells, and protect the inside, which contains the

life carrying components, from the outside. On the other hand, cell membranes have to ensure good transport between the inner and outer of the cell, thus, many ion channels, composed of proteins, are embedded in the membrane, so that various small molecules and ions can pass them through and nourish the cell.

Cells are the basic unit of structures and functions directly related to all life activities of human body and almost all the other living organisms. All physiological functions and biochemical reactions in the bodies are performed on the basis of the stromal of cells and their synthetic or excretive materials (such as, the collagen and proteoglycans in the cell gap). All animal and plant cells are encapsulated by a layer of thin membranes, called the cell membranes (biomembranes) or plasma membranes, which separate the cell internal contents from cell external environment (mainly extracellular fluid), so that cells can exist relatively independent of their surrounding environment. Obviously, if a cell wants to maintain normal life activities, not only its contents cannot be lost, but also its chemical composition must remain relatively stable, which requires a structure between the cell and its environment to play a role of the barrier. However, in the ongoing process of metabolism, the cells also need to get oxygen and nutrients from the outside, and expel cellular metabolites. The entry and exit of these substances both have to go through the cell membrane, which involves the process of transmembrane transport for the substances. Thus, the membrane must be a special structure with the function of a semipermeable membrane which allows certain substances or ions to selectively pass through, but can strictly limit the number of other substances into and out of the cells to maintain the stability of the material composition. Inside the cell there are some similar cell membrane structures, which constitute a variety of organelles, such as mitochondria, endoplasmic reticulum and other membranous parts, keeping them alive not only with the general existence of a barrier between the cytoplasm, but also with the transport of certain substances. In addition to the function of the material transport, the membranes have the functions of transmembrane information transfer and energy conversion, whose mechanism are decided by the membrane composition and molecular structure. In membrane compositions, lipid molecules mainly play a role of the "barrier", and special proteins in membrane are related to the transmembrane transport of matter and information and the conversion of energy.

One important problem, plaguing biologists for several decades, is whether there is the existence of the small domains composed of the aggregates of special kinds of lipids and proteins on biomembranes? From the point of view of simple model, the existence of this small area is possible. Gel-liquid phase separation is an example most easily understood[50]. In fact, it is also observed that the membrane structure encapsulating several cells and organelles inside is not uniformly formed by a simple component, but in which there are colorful complex structures like mosaic small areas [51]. For the past

decade, ones have found the tiny membrane lipid rafts scattering on the surface of cell membrane. This is the best evidence that small and specific functional areas do exist on cell membranes, and the membrane structure is indeed a complexity of structures. It also presents a major challenge for the future research of biomembranes.

2.1.1 Structures of biomembranes

Biomembranes are dominantly composed of phospholipids and various kinds of proteins and carbohydrate macromolecules inlaid thereon. Although different membranes from different sources contain varied proportions and compositions of various substances, but generally are mainly based on proteins and lipids, with only a small amount of carbohydrates. If they are calculated by weight, the weight of membrane proteins is about $1 \sim 4$ times of that of lipids, but the molecular weight of a protein is much larger than a lipid molecule, so membranes contain the number of lipids molecules much more than protein molecules, at least it also exceeds more than 100 times the number of protein molecules. Thus, we can image that scattered proteins float on the 2D lipid sea. Biomembranes play the roles of the division and the separation of cells and organelles, but they are also important parts related to a lot of activities of energy transformation and intracellular communication, as well as, have a large number of enzyme binding sites thereon. Cells, organelles, and their borders with the environment are all coated by the membrane structure in general. Organisms, except for some viruses, all have biomembranes. Eukaryotic cells (Figure 2.1 below), in addition to plasma membrane (also known as cell membrane), contain a variety of intramembrane systems, which separate organelles, including nuclear membrane, mitochondria membrane, endoplasmic reticulum membrane, lysosomes membrane, Golgi membrane, chloroplast membrane, peroxisome membrane, and so on [48]. Biomembranes have a kind of morphology of lamellar bilayer structure with a thickness of about 4 to 10 nm. Its compositions are mainly lipids and proteins, with a minor amount of saccharide is covalently bound to the lipids or proteins. Different biomembranes execute different physiological functions.

The existences and arrangement patterns of various molecules of substances in the membranes is the key factor to determine the basic biological characteristics of membranes. Molecular biology studies show that the special ordered arrangements of various membrane substances, especially biological macromolecules, in many kinds of biological structures are the bases for the realization of a variety of life phenomena. Although there are currently no convenient techniques and methods able to directly observe the molecular structure of the membranes, but based on some analyses and researches on characteristics of artificial membranes and biomembranes, since the 1930s ones proposed many

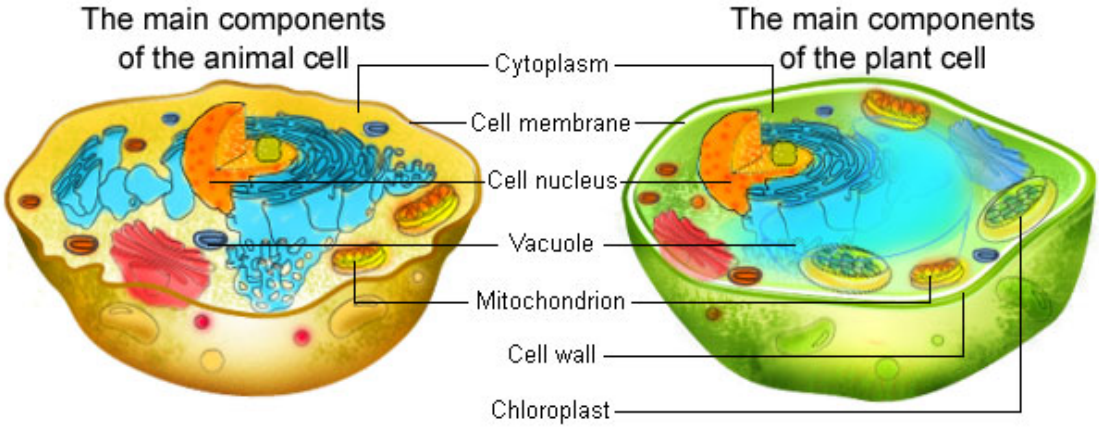

FIGURE 2.1: A schematic picture shows the main structures of animal and plant cells. Reprinted with permission from http://jpsy2011.blogspot.jp/2011/02/similarities-and-differences-between.html.

hypotheses on molecular structures of biomembranes , in which fluid mosaic model proposed by Singer and Nicolson's in 1972 [1], gaining many supports of experimental facts, is now widely recognized, as is shown in Figure 2.2.

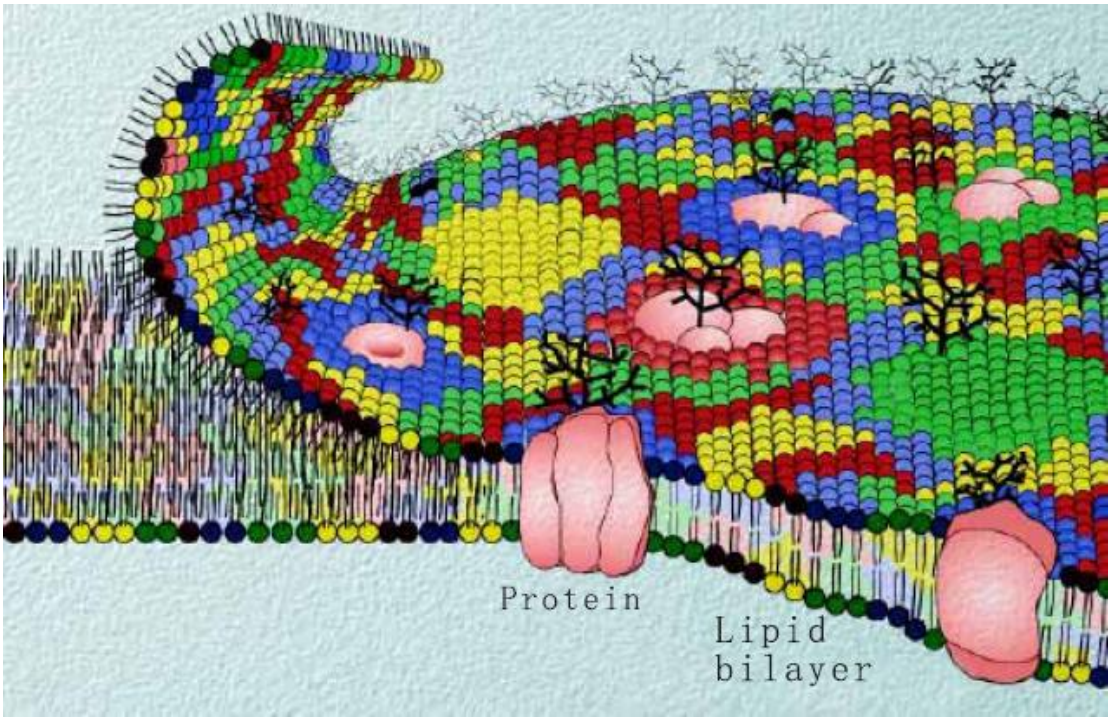

FIGURE 2.2: Singer and Nicolson's fluid mosaic model is shown. Reprinted with permission from Ref. [52].

Fluid mosaic model is a dynamic model, which emphasizes the continuum of phospholipid bilayer membrane, with protein molecules randomly dispersing in the lipid bilayer.

Experimental results indicate that the mobility of the lipids is a significantly basic property of membrane structure. The properties of biomembranes reflected in this structure model can be concluded into the following aspects:

1. Biomembranes are composed of complex mixtures of a variety of phospholipids and other amphipathic molecules. Different types of biomembranes have generally different compositions, which propbably form different subphase areas of different components on the plane of membranes.

2. In addition to the formation of the lipid bilayer of amphiphilic molecules (such as phospholipids), there are a considerable number of other membrane molecules on membranes. Specifically, many animal cells contain cholesterol molecules, whose amphiphilicity is weak, but can dramatically change the strength and permeability of biomembranes.

3. Biomembranes contain a certain amount of proteins of different types, called membrane proteins. Some of them insert into the membrane, while others completely pass through both sides of the membrane, called transmembrane proteins. These transmembrane proteins form the membrane pores through which the medium sizes of molecules can pass. In some cases, cells can pump molecules through this channel against chemical potential gradient.

4 Biomembranes are asymmetric, and have different chemical compositions on both sides

5 The outer membrane part contains various short-chains of polysaccharide. these chains become specifically amphiphiles – hydrophilic groups of glycolipids, or combined with membrane proteins covalently.

6. The inner membrane part can form the cytoskeleton connections with some kinds of protein networks of reversible actin polymerization. Membrane and cytoskeleton are connected as a single entity, so that cells are able to control the membrane curvature and flexibility, and further have the abilities of movement and division by manipulating the membrane shapes (Figure 2.3 below).

2.1.2 Chemical components of biomembranes

The main components of membrane lipids are phospholipids, accounting for more than 70 percent of the total amount of lipids, followed by cholesterol, generally less than 30 percent, and there is a small amount of sphingolipids. The basic structure of phospholipids: a hydrophilic polar head (a phosphate-binding molecule with a hydroxyl group is combined with a base) and a hydrophobic tail of fatty acyl chains (two hydroxyl groups of a glycerol molecule combine with two molecules of fatty acid). According to different bases,

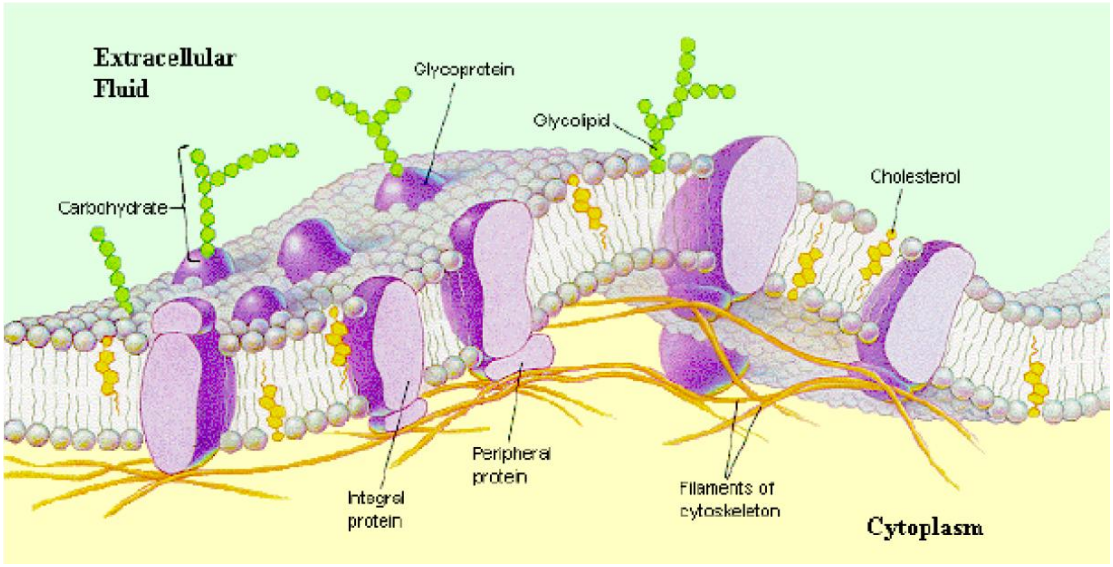

FIGURE 2.3: Schematic picture shows biomembrane patch with the junctions connected with cytoskeleton inside. Reprinted with permission from Ref. [53].

in the membrane of animal cells, there are mainly four phospholipids(Figure 2.4 shown): phosphatidyl choline, phosphatidyl ethanolamine, phosphatidyl serine and phosphatidyl inositol. Sphingolipids have the similar basic structure to phospholipids, but without glycerol. These amphiphilic characteristics maintain the structural stability of membranes. The hydrophilic head portion likes towards the aqueous phase, while the hydrophobic tails aggregate with each other to avoid the water. This kind of effect is so-called hydrophobic interaction. The bilayer arrangement of lipid molecules is essentially a kind of entropy effect [54], which satisfies the requirements of thermodynamic stability, and is the integrated result of the effects of the hydrogen bonding in a solution, intermolecular van der Waals forces, dispersion forces, etc.

The low melting point of lipids determines that lipid molecules in the membrane are generally in the liquid state under the condition of body temperature, i.e., membranes have a degree of fluidity. The thermodynamic stability and its mobility of lipid bilayers can explain why cells can withstand considerable tension and the shape deformation without the rupture, and even if the membrane structure may have some minor faults, they can automatically be fused and repaired, still maintain a continuous bilayer formation.

2.1.3 Structures and functions of lipid rafts

Since 1972, American scientists Singer and Nicolson proposed the fluid mosaic model of biomembranes [1], it has been more than 30 years. Although it is generally believed that some fundamental aspects of this model are still correct, but the lipid bilayer is

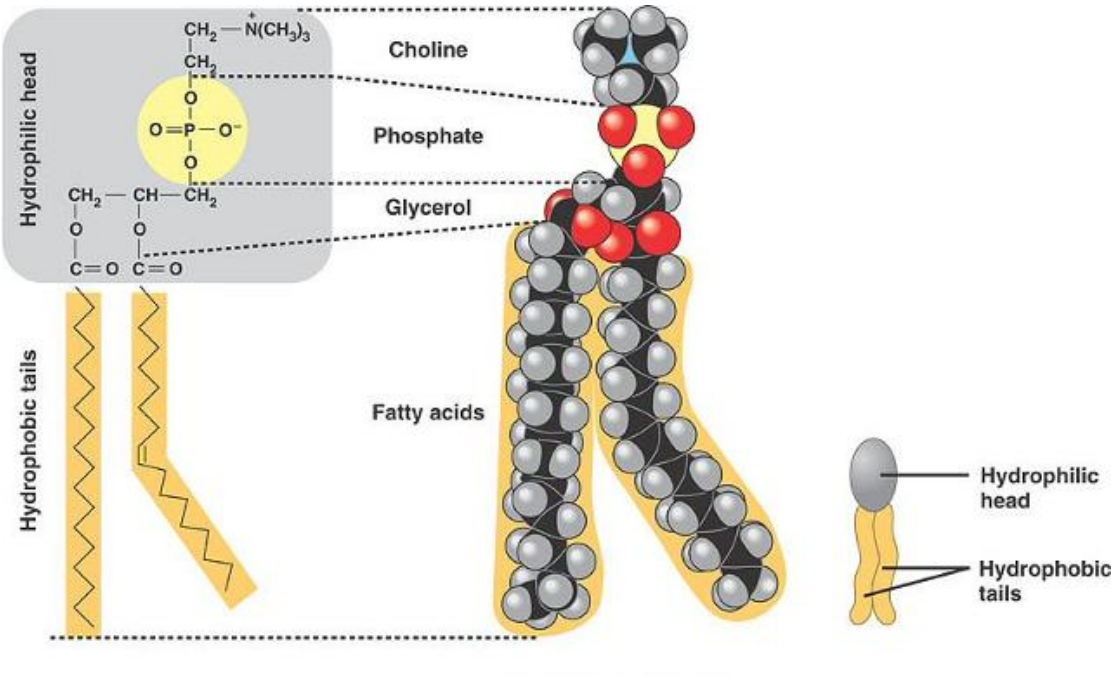

FIGURE 2.4: Chemical components of phospholipids. Reprinted with permission from http://www.glycoforum.gr.jp/science/word/glycolipid/GLD01E.html.

not actually a uniform two-dimensional fluid, some kinds of lipid molecules can form a relatively stable gel state or liquid-ordered state, but at that time enough considerations were not given to the inhomogeneities of biomembrane structure yet. As time goes on, people have come to realize the importance of the inhomogeneities, that is, the existence of microdomains on biomembranes. The heterogeneous membrane model hypothesizes the existence of domains of lipids in the liquid-ordered (l_o) phase surrounded by lipids in the liquid-disordered (l_d) phase. One kind of these microdomains is called lipid raft, which is proposed by German biologist Kai Simons in 1997 [2]. Simons and his colleagues used a mild non-ionic detergent to dissolve the cell membrane. This is a commonly used experimental method to isolate the structures of lipid rafts from the cell membranes. Under the condition of the detergent treatment, glycerol and phospholipids are removed from membranes, while the raft structures composed of sphingolipids and Cholesterol and the binding proteins are not soluble in the detergent. This structural part of membrane contains a large amount of lipids, and therefore has a relatively small density. It is separated by centrifuge, and polymerized together. Like this, a detergent-insoluble membrane is extracted. These decontamination insoluble membranes contain cholesterol and sphingolipids as the main membrane lipid compositions that, thus, create the concept of lipid rafts [55]. Lipid rafts are a kind of lipid microstructures different from caveolae on biomembranes (as Figure 2.5 shown), containing a certain amount of proteins and lipid molecules, where lipid molecules are mainly based on sphingolipids and

cholesterol, and the former including sphingomyelin and glycosphingolipids, whose main difference lies in the oligomeric sugar residues contained in the molecules. Generally speaking, the components of lipid rafts are rich in glycosphingolipids and protein receptors [5, 6, 56]. In the biochemical experiments, the size of lipid rafts has been defined as $10 \sim 200nm$ very recently [19], but many people also think that the size of lipid rafts may not be limited to this range. Lipid rafts are flat membrane structure. Generally they do not have the apparent structure of the fixed characteristics and basically keep the same morphology as the surrounding cell membrane, so they are generally not easy to be observed by the electron microscopy. Therefore, the main criteria for that lipid raft structure on cell membrane different from the surrounding cell membrane can be indicated by its morphological characteristics, but by its special lipid compositions. In addition to lipid raft composed of different compositions from the surrounding membrane, its binding proteins are not the same as the surrounding part, such as caveolin, flotillin, and some transmembrane proteins anchored on lipids of cell membranes, all of which are only located in the region of lipid rafts. While a considerable part of receptors on the cell membrane and their corresponding signaling protein molecules have also been found in lipid rafts [2].

Through the discovery and repeated identifications of lipid rafts, many lipid rafts should be much smaller than ones imagine. Therefore, biomembranes should be considered as an inhomogeneous supramolecular system with the compositions of lipids, proteins and carbohydrates, in which lipid membranes contain glycerides as its main component. while lipid rafts, including sphingolipids and cholesterol as the main ingredients, with different sizes are dispersed in the lipid membranes, therefore, the entire membrane is like a static mosaic composed of many microdomains [51]. However, lipid raft region contains more kinds of functional membrane proteins and a higher concentration of glycolipids than the membrane main body (Figure 2.5 below). Thus, Singer and Nicolson's fluid mosaic model needs some corrections. Because lipid rafts are not static, but dynamic, it increases the structure complexity and lateral heterogeneity of biomembranes.

These lipid rafts on membranes not only constitute the special structure of cell membranes, and more importantly, they are involved in many important physiological activities on cell membranes, such as, vesicle transport (endocytosis and exocytosis) on membranes, regulation of cell cholesterol balance, transmembrane conductance of cell signaling, and so on.

Currently our understanding for the structures and functions of lipid rafts is still very limited. Biologists, chemists and physicists hope that more clear information about the structures and functions of lipid rafts can be obtained from the experiments in the near future.

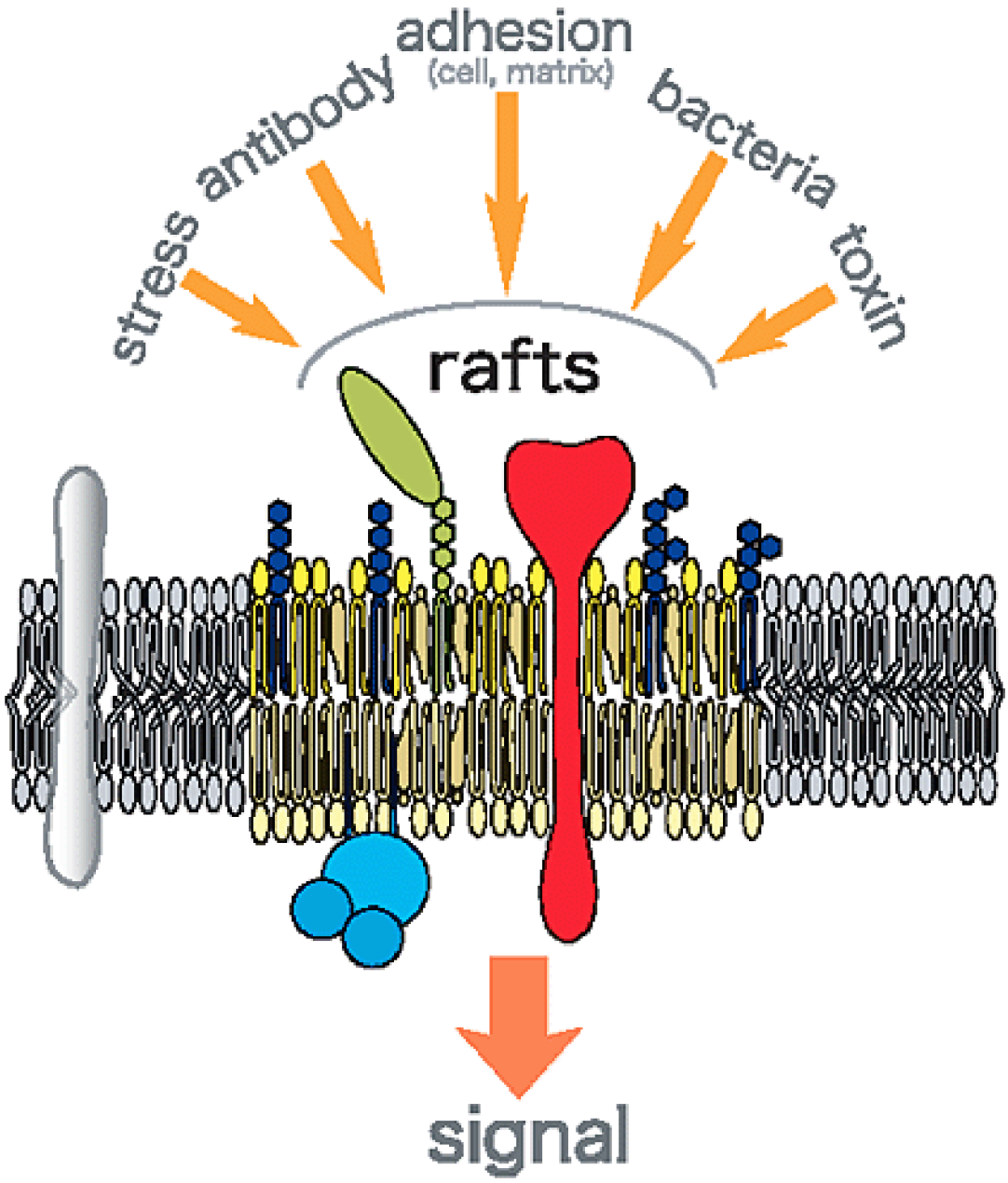

FIGURE 2.5: Schematic picture of lipid raft microdomains, where there are various membrane proteins performing physiological functions and signal transduction, as well as a higher concentration of glycolipids inside lipid raft domains than the membrane main body. Reprinted with permission from http://www.glycoforum.gr.jp/science/word/glycolipid .

In this section, we simply introduced biomembranes and some basic knowledge of lipid rafts. by learning about these, ones can deeply realize that some characteristics of biomembrane and their important roles for sustaining organisms. In the following sections we will introduce some important in vitro experiments on biomimic membranes, especially a recent experiment on microdomain sepration induced by PEG-anchored multi-component membrane. From the physical point of view, these experimental observations lead to this PhD study on polymer-anchored multi-component membranes.

2.2 Lipid membranes in lab

Since biomembranes are composed of mixtures of various different kinds of lipids and proteins, the investigations on more complex model systems are highly interesting. To obtain insight into the roles of membrane components, many groups have focused their efforts on making artificial membrane systems typically including ternary lipid species. A general focus is the long standing question on lipid-protein interactions. Another general one is the question on the membrane lateral heterogeneity, which is often characterized by the terminology, lipid rafts. To mimic real conditions of biomembranes, multi-component membranes, usually composed of ternary components, such as commonly DOPC/DPPC/Cholesterols, are applied to form optically observable μm scale domains. The l_o domains (experimentally called artificial lipid rafts) are rich in cholesterol and saturated lipids, and are thought to play an important role in regulation of cell processes. Although many controversial issues on the exact nature of lipid raft and its size and time scale are still existing, as well as ones debated if they are on earth some kind of non-equilibrium or equilibrium structures or whether they require a certain kind of mechanism, e.g. some specific proteins, to maintain themselves. Whatever the conclusions will be to these investigations, it is clear that the equilibrium measurement on optically observable μm domains in biomimetic model mixtures is always valuable to understand the mechanism and interaction existing on biological rafts from the molecular level, no matter what they will finally turn out to be. So it is certainly appropriate that the further study of lateral organization on multi-component membranes with anchored polymers is included in this thesis.

2.2.1 Phase separation on multicomponent membranes

To many biophysicists it seems intuitively obvious that the presence of various kinds of composition lipids and proteins in biomembranes can result in lateral heterogeneity of lipids and proteins [57]. The idea that specific lipids might be helpful to laterally organize membranes into discrete domains with different properties received only sporadic

attention over the past four decades [58, 59] until the past ten years which witnessed an explosion of interests and the studies of the raft paradigm. Like other scientific paradigms, raft may mean different things to different research groups. Nevertheless, lateral heterogeneity is definitely an important research focus in the field of biomembrane.

The free energy differences of the effective interaction between different lipid compositions is the main reason to lead to the lateral lipid heterogeneity [58, 60–64]. Some kinds of entropic components will be necessarily involved in these kinds of free energies which are, therefore, not able to be obtained by simple calculation of molecular energetics. In principle, they can be estimated by All-atom Molecular Dynamics [65], but as we will introduce in Chapter 3, this simulation method is very time-consuming to reach the equilibrium lateral distribution of lipid compositions. Unless ones can appropriately choose an effective initial distribution which is very close to the correct distribution. Another feasible way is to apply coarse-grained simulations [66–69], which have sufficient time to achieve the equilibrium state. Or ones also can use analytical methods in which infinite time is available [60, 61]. But in the latter two cases, the effective interaction have to be estimated correctly. One way is to obtain the correct effective interactions by adjusting them to be consistent with experimental phase diagrams [58, 60–64, 70]. It is also why the accurate equilibrium phase diagrams for multi-component vesicles and membranes are desirable, even if the transient states of lipid rafts may not be in the thermodynamic equilibrium [58]. Unless the tie-lines which indicate the compositions of coexisting phases are determined, the effective interactions are still unknown even if the regions of phase coexistence at large scale are gained by applying fluorescence spectroscopy.

2.2.1.1 Phase diagram on membranes of ternary components

In cell membranes, the common ternary components are phospholipid, cholesterol, and sphingomyelin, where phospholipid is unsaturated, sphingomyelin is saturated so that it have strong affinity to combine cholesterol molecules as the main ingredients of lipid rafts. In the lab, biochemical experimentalists usually applied artificial ternary lipid membranes of DPPC/POPC/Chol [14, 20, 71, 72], eSM/POPC/Chol [72] or PSM/POPC/-Chol [8, 73] to replace cell membrane components, in which DPPC, eSM and PSM are saturated lipids and can be experimentally prepared easily. The studies on phase separation on multicomponent membranes are valuable to study the lateral structure organization on cell membranes. The ternary diagram of the canonical raft mixture in the tensionless membrane state is often referred to in many references on phase separation of lipid mixtures. One most famous canonical raft diagram was built from fluorescence

imaging and NMR data [73]. So far the construction of the full phase diagram is still challenging experimentally, and also for theory and simulation.

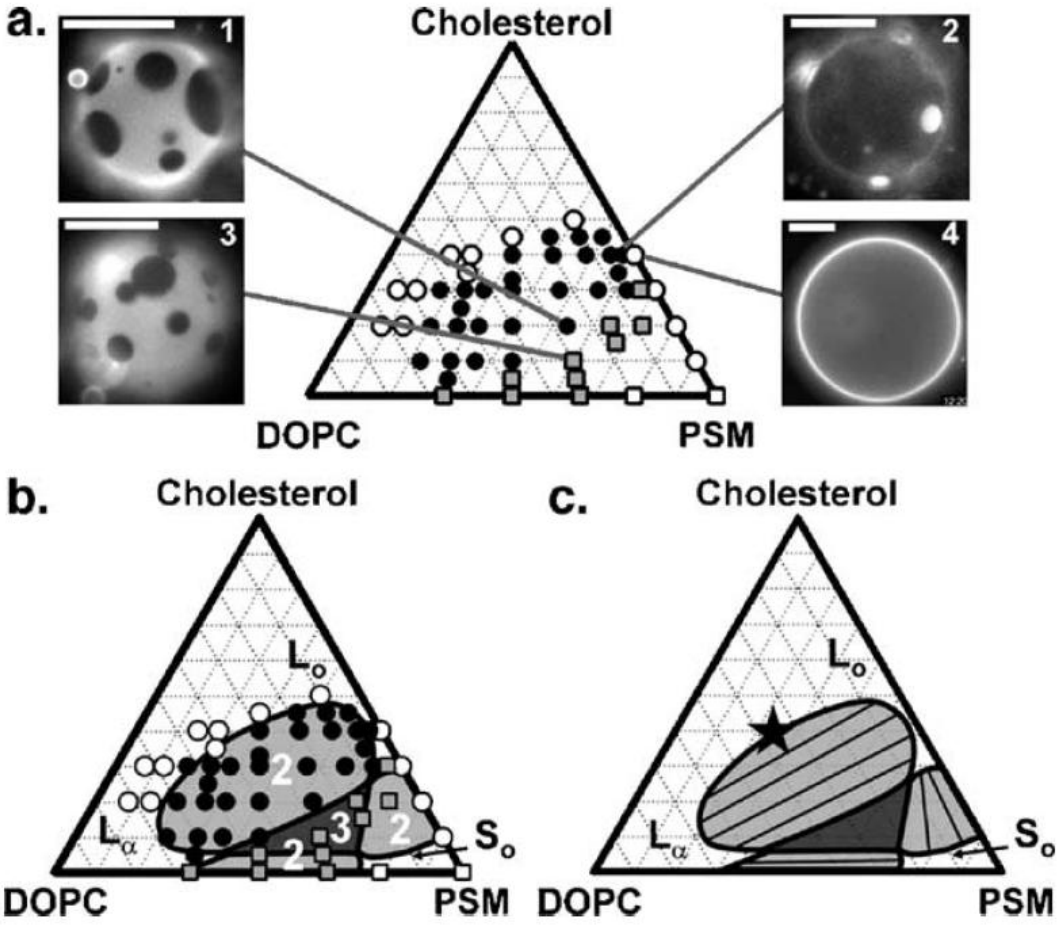

FIGURE 2.6: (a) Various coexisting phases observed by fluorescence microscopy of GUVs containing mixtures of DOPC, PSM, and cholesterol at 25°C. (b) Fluorescence microscopy data are consistent with a speculative underlying phase diagram including a region of three-phase coexistence. (c) Speculative location of tie-lines and a miscibility critical point (star). Reprinted with permission from Ref. [74]

Thermodynamically the tie-lines indicate the conditions where two phases can exist at equilibrium. Through following a tie line, one knows how the melting point or the miscibility transition point of a certain kind of composition lipids changes with pressure, membrane component ratios, temperature or some other experimental conditions. Under conditions one side or the other side of a tie-line means that a particular phase is stable. Tie-line determination is a hot topic of current studies on biomembranes [73–80]. It clearly decide the quantitative values of the effective interactions between different membrane components with their molar concentrations in the coexisting phases [73]. By comparing thermodynamic theories [60, 61] phase diagrams with tie-lines could provide

an estimate of the effective interaction free energies that may then be applied in coarse-grained Molecular Dynamics simulations [62, 64, 81] to provide approximations to the lateral distributions of membrane components. These lateral distribution conditions can then be chosen as the initial states of molecular dynamics simulations which could inversely be tested directly against experimental data. If such an interactive program is successful, this will massively improve our current understandings on lipid lateral heterogeneity.

A typical ternary phase diagram is shown in Fig. 2.6 (from Ref. [74]), where a solid l_o phase and a globally single fluid phase are locally triangularized as liquid disordered l_d and liquid ordered l_o due to a fluid-fluid coexistence (red) region ending in a consolute point close to the yellow dot. Both the solid (s_o) and liquid-ordered (l_o) phases appear dark by fluorescence microscopy in Fig. 2.6(a). s_o and l_o phases are distinguished based on lipid mobility.

Fig. 2.6 provided the speculative slopes of the tie lines for $l_d - l_o$ coexisting, $s_o - l_o$ coexisting and $l_d - s_o$ coexisting, respectively, as well as the three-phase coexistence state in the triangular three-phase region with a miscibility critical point (star) shown thereon. The recent work modified the boundaries of the three-phase and low cholesterol regions by adding X-ray data [58, 71], so that it can obtain the slopes of the two-phase tie lines with even greater accuracy than had earlier been obtained using NMR [75].

2.2.1.2 Dependence of line tension on temperature

Membranes composed of various ternary mixtures of saturated lipids, unsaturated lipids, and cholesterol undergo lateral phase separation into coexisting liquid phases at a miscibility transition. When artificial membranes are manufactured from a ternary lipid mixture at a critical composition, they undergo a miscibility critical point at the transition temperature. In the biophysical experiments, the critical temperature is typically comparable to the room temperature, thus, artificial multi-component membranes provide a good platform to perform a quantitative study of real biomembrane systems, where ones can regard it as a physical system that exhibit similar critical phenomena to the two-dimensional Ising universality class. As a critical point is approached from either the high or low temperature direction, the scale of fluctuations in lipid composition, scaled by the correlation length, diverges. Previously most of people working on multi-component membranes are only concerned with the ternary phase diagram of artificial membranes [8, 73, 73, 75–80, 83]. Recently some groups realized that as a critical point is approached, the domains of L_o phase in L_d phase will diminish, during this period then line tension between coexisting domains could play an important role [82].

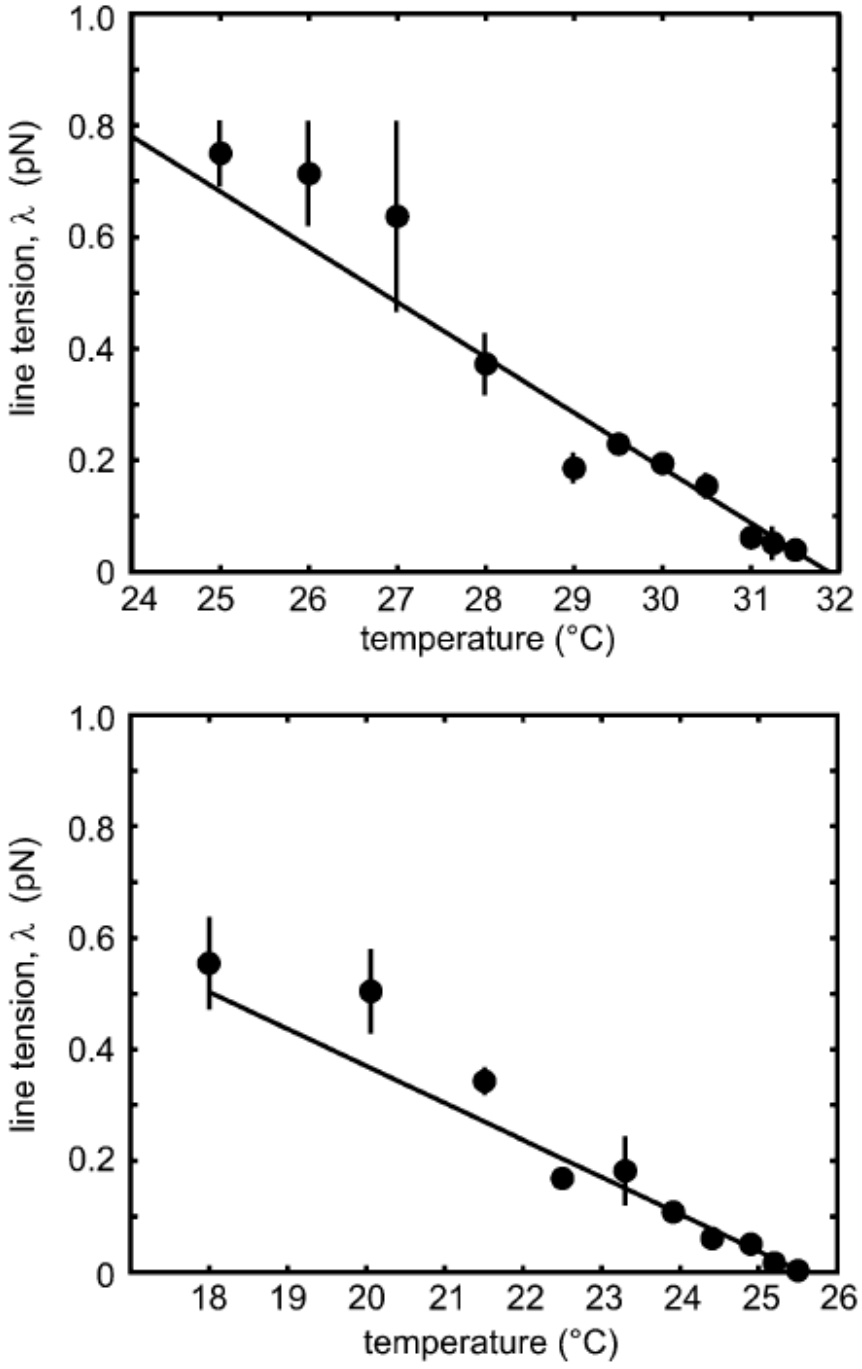

FIGURE 2.7: The upper and lower panels show line tension between coexisting domains with standard deviations obtained from two different vesicles, respectively, at various temperatures. The line tension can approximately be considered to decrease linearly with increasing temperature close to the miscibility critical point T_c. Standard deviations are found by comparing line tensions from more fluctuating domains visible. At some temperatures, only one domain was available and no standard deviation is shown. Reprinted with permission from Ref. [82].

Honerkamp-Smith and his colleges quantitatively evaluate the temperature dependence of line tension between liquid domains for the first time. They found when a critical point is approached from the low temperature direction, the line tension between two coexisting phases gradually decreases to zero.

In their recent experiment [82], all line tensions from one of two individual vesicles are collected and plotted in the upper or lower panel in Fig. 2.7. They estimated standard deviations by comparing line tensions obtained from two or more fluctuating phase domains visible in a single frame and/or breaking long movies into runs of 20 frames or greater. The two panels of Fig. 2.7 show the measurements of line tension for all domains at all temperatures of two different vesicles. They find that line tension decreases almost linearly to zero at the critical transition temperature. Their measured line tension values are valid only for temperatures within 10°C of the critical temperature due to the optical resolution limit. All the measurements have been done in the tensionless state of multi-component membranes.

2.2.1.3 Effect of surface tension on miscibility temperature

Another interesting experiment on biomimetic membranes recently has also been posed by Keller group [84]. They have further considered the effect of membrane-cytoskeletal interaction in real cell membranes, and the cytoskeletal part can provide some tension to the membrane part so that the membrane part is not tensionless. They tried to answer how membrane tension influences the miscibility temperature of lipid bilayers.

In their ternary lipid system, because the acyl chains of both DiPhyPC and DMPC are saturated, they chose ternary vesicle composition to be a $1:1:1$ molar ratio of diphytanoylphosphatidylcholine (DiPhyPC), dimyristoylphosphatidylcholine (DMPC), and cholesterol to minimize photo-oxidation and set the initial miscibility transition temperature T_{mix} near 30°C [84].

They microaspirate giant unilamellar vesicles to determine the effect of mechanical stress on the liquid/liquid miscibility temperature of a membrane composed of a ternary lipid mixture.

To measure the change of the miscibility transition temperature ΔT_{mix} versus the change of applied tension $\Delta\sigma$, the following procedures were followed:

1) Initial tension of $\sigma_1 > 1mN/m$ was employed to a giant unilamellar vesicle. The membrane was then in the stretched state.

2) The sample was heated above the miscibility temperature such that membrane domains disappeared.

3) Temperature $T_{\mathrm{mix},1}$, at which domains reappeared by cooling sample slowly, was measured.

4) Tension was tuned to a new value, σ_2.

5) Steps 2) and 3) were repeated to decide $T_{\mathrm{mix},2}$.

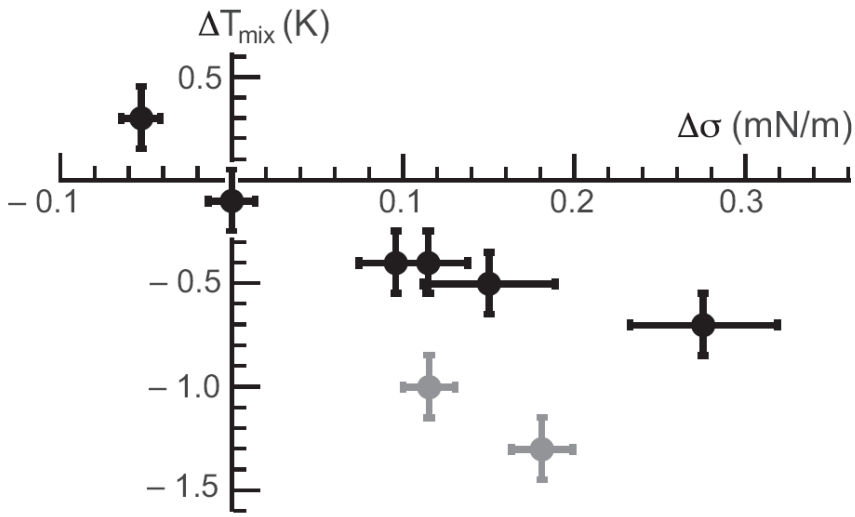

FIGURE 2.8: Measured shift in miscibility temperature, ΔT_{mix}, as a function of difference in applied tension, $\Delta\sigma$. Black and gray symbols are obtained using Rhodamine-DMPE and Rhodamine- DOPE fluorescent dyes, respectively. Reprinted with permission from Ref. [84].

They used eight experiments of the above type (see Fig. 2.8) to confirm that the increase of membrane tension decreases the miscibility temperature. In Fig. 2.8, the two gray points and the two black points with the largest values of $\Delta\sigma$ were from vesicles used in each of two experiments. They fit a straight line to quantify the effect of $\Delta\sigma$ on ΔT_{mix} for the black data points in Fig. 2.8 and obtained a slope of $-2.8 \pm 0.7 K/(mN/m)$. Because they only obtained a few of data points and no priori linear relationship between $\Delta\sigma$ on ΔT_{mix} existed previously, this slope value only could be understood as an order of magnitude but not as a precise value [84].

2.2.2 Micro-segregation triggered by PEG-anchored lipids

A more complex study of model membrane systems is the addition of various peptides or other macromolecules to lipid bilayers, such as PEG chains. The investigations on such systems could provide the answers to two general questions to us. One is how the additive influence the bilayer. Does the bilayer become stiffer? Could the additive change local spontaneous curvature or even induce the pore on the bilayer? How does

the additive affect the interfacial tension between two coexisting lipid domains in multi-component membranes? The other question asks inversely what are the effects of the bilayer on the additives. How does the bilayer restrict the conformation of the additives? And how does the additives anchor on the bilayer.

As we have introduced above, real cell membranes contain not only bare lipids, but also a large amount of bulky glycolipids, which play an indispensable role in cellular membranes. But so far little has been known about the effects of bulky glycolipids on the physicochemical properties of the membrane. Recently, Yanagesawa and coworkers have applied a kind of bulky lipids, that is, lipids anchored short polymer chains, e.g. PEGs, with different molecular weights. Their work tried to obtain some insights to the first category of the above questions on the effects of the additives on membranes.

For the desired experiment, they constructed poly(ethylene glycol)-conjugated cholesterol (PEG-Chol) as a model glycolipids to clarify the effects of bulky-head lipids on phase separation. The physical properties of lipid bilayers including PEG-lipids have been studied extensively. For example, PEG-lipids in a membrane reduce the main gel-to-liquid-crystal transition temperature of lipids [85], increase the bending rigidity [23–27, 86–90], and induce a finite spontaneous curvature [23–27, 88–91]. However, currently there are still no theoretical or experimental studies on the effects of PEG-lipids on phase separation in multi-component membranes. Therefore, they constructed poly(ethylene glycol)-conjugated cholesterol (PEG-Chol) as a model glycolipids to clarify the effects of bulky-head lipids on phase separation.

They first prepared a tranditional ternary GUV composed of DPPC, DOPC and Chol [10, 73]. It is recognized that tranditional ternary vesicles composed of DPPC, DOPC and Chol separate into the l_{d} and l_{o} phases, and form a mono-domain to minimize the line energy, that is, interfacial instability at domain boundaries [20]. This is classified as a first-order phase transition under the criterion of Landau.

Then, they gradually replaced Chol in the ternary GUVs with PEG-Chol. By comparing the domain patterns observed with and without PEG-Chol, they illuminate show here the occurrence of stable micro-domains in the molar fraction of PEG-Chol above a critical composition. The transition from global- to micro-segregation is interpreted in terms of the competition between two physical effects, i.e., polymer brush effects between the bulky-head groups of PEG-Chol and the cost of interfacial line tension along the domain boundaries, as will be illustrated in Chapter 7 in detail. Interestingly, near the critical micelle concentration of PEG-Chol, a network pattern of domains appears as an intermediate state in which small domains are connected to each other (see Fig. 4 in Ref. [20]). They further examined the stability of the network pattern by local heating using a focused laser, and confirmed that it exhibited an ability of self-recovery [20].

They also investigated the polymer length dependence of the micro-segregation of the big domain. They found that the anchored longer polymer (PEG) chains can induce the micro-segregation in a lower anchored density compared with the short PEG chains. In Fig. 5 a, b and c in Ref. [20] clearly show more and smaller scattered domains in vesicles composed of DPPC/DOPC = 1 : 1 plus 20% PEG2000-Chol emerge compared with the cases with the same concentration of PEG1000-Chol and PEG600-Chol. This agrees with the fact that critical micelle concentration (CMC) is decreased with an increase in the molecular weight of PEG. Therefore, it is most likely that when the mole fraction of PEG approaches the CMC, the increase in the free energy of PEG-Chol overcomes the cost of the line tension energy, and leads to a transition in the domain size.

Based on their observations, natural bulky-head lipids in cells may be helpful to stabilize the domain structure like a lipid raft. Their study may shed light on the intrinsic mechanism of the stabilization of nano-domain structures in cells containing large numbers of bulky-head lipids and proteins [20].

Chapter 3

Theory and Simulation of Membranes and Polymers

Membranes and polymers are supermolecular systems, which typically exist at the mesoscopic level, about μm. On one hand, such systems are big enough, dynamics and equilibrium structures of them have the mechanical properties stronger than $k_{\mathrm{B}}T$ and can exist at a relatively large scale and long time scale. On the other hand, the ones of such systems are small enough, they can be affected by thermal fluctuation, which can cause polymer configuration transition and membrane undulation, as well as self-assembly process of amphophilic molecules in solution. Theoretically the configuration of a long linear polymer chain satisfies Gaussian type of random walk theory for ideal chains and self-avoid walk theory for excluded-volume chains. After polymer theory was built up, people realized that membranes looked like two-dimensional versions of polymers. Since people had studied random polymers (Gaussian type), people wanted to study membranes as 2D random surfaces. Tensionless membranes at large scales are very good representations of random surfaces.

3.1 Theory of membranes

In this section, we introduce some fundamental knowledge on membrane theory describing membrane deformation and vesicle shape transition. At first, the famous Helfrich model based on local curvature energy is revisited. Then its Monge form on almost planar membrane patch is introduced by a small curvature expansion.

3.1.1 Helfrich curvature elastic free energy

In the fluid membrane state, the area of membrane is assumed as the constant, since no work is done to increase the area, which corresponds to surface tension. Thus, the only important quantity for the fluid membrane is the curvature. And because membrane is in the fluid state, the environment of pure membrane should be homogeneous and isotropic, and the energy functional of membrane should be a translational invariant, that is, the spatial position of membrane does not enter the Hamiltonian to change the membrane free energy [92].

Due to the large aspect ratio between the lateral dimension and the thickness as well as the small compressibility, a lipid membrane is usually regarded as an incompressibility elastic thin film in mechanics and a smooth surface in mathematics when we investigate its large scale behaviors. It is indeed true that the thickness of a patch of membrane is about four or five nanometers, so we can ignore the membrane thickness and consider a membrane patch or a vesicle as a open or closed 2D surface embedded into 3D space. In differential geometry, any surface can be locally described by its two vertical and orthogonal radii of curvature R_1 and R_2 (usually we choose the two principal curvatures for the convenience), from which we can further obtain the mean curvature:

$$H = \left(1/R_1 + 1/R_2\right)/2 \tag{3.1}$$

and the Gaussian curvature

$$K = 1/R_1 R_2 \tag{3.2}$$

If the environment of both sides of membrane is symmetric, that is, there is no different percentage of lipid compositions on both leaflets, and no different external interactive object or material attached on both sides, then we easily know the free energy should be symmetric and the curvature should be included in a quadratic form. The whole free energy of membrane can be described by the integral on the curvature over the membrane surface. And two prefactors κ and $\bar{\kappa}$, corresponding to the mean curvature and the Gaussian curvature, are introduced and called the bending rigidity and the Gaussian bending rigidity (or saddle-splay modulus), respectively. Then we can write down a curvature elastic free energy for a symmetric membrane or vesicle as follow:

$$F_{sym} = \int dA 2\kappa H^2 + \int dA \bar{\kappa} K \tag{3.3}$$

where the values of κ and $\bar{\kappa}$ can be extracted by the experiment, since κ is much higher than the thermal energy $k_B T$. For lipid bilayer, ones find κ is about $10 - 40 k_B T$, which

are quite depend on the kinds of lipids. But the Gaussian bending rigidity $\bar{\kappa}$ is difficult to measure since the second integral is a topological invariant, which is the consequence of Gauss-Bonnet Theorem. The parameter $\bar{\kappa}$ measures the energy change by the formation of handles.

To deal with some complicated cases of real cell membranes, a full form of the curvature elastic free energy is proposed by considering the asymmetric environment of membrane and introducing several additional terms as Lagrange multiples as follows:

$$F_{Hel} = \int dA 2\kappa \left(H - c_0\right)^2 + \int dA \bar{\kappa} K + \int dA \sigma + \int dV \Delta P + \int dL \gamma \quad (3.4)$$

where c_0 is call the spontaneous curvature of the membrane, which is used to describe the asymmetric degree of both sides of membrane. σ, ΔP, and γ are three Lagrange multiples, which can also be considered as the surface tension of membrane, the pressure difference between inside and outside a vesicle, and the line tension if there is a pore on membrane, respectively. This full form is also called Helfrich curvature elastic free energy, which was first proposed by Prof. W. Helfrch in 1973.

3.1.2 Monge representation for a patch of small curvature surface

Besides by using three independent orthogonal orientational coordinates x, y, and z, almost planar surfaces in 3D space can be described by two independent orthogonal orientational coordinates x and y along the surfaces and then a "height" $z = h(x, y)$ to describe the surface deformation or fluctuation [93], alternatively. Thus, the area element dA is given by

$$dA = \sqrt{1 + h_x^2 + h_y^2} dx dy \quad (3.5)$$

where the subscripts denote a derivative, e.g., $h_x = \partial h(x, y)/\partial x$. Thus, the normal on surface is given by

$$\hat{n} = \frac{\hat{z} - h_x \hat{x} - h_y \hat{y}}{\sqrt{1 + h_x^2 + h_y^2}} \quad (3.6)$$

We use a Monge representation on membrane surface with the displacement $h(x, y)$ which is oriented in the $h = 0$ plane. The mean curvature can then be given by

$$\begin{aligned} H &= \frac{(1+h_x^2)h_{yy} + (1+h_y^2)h_{xx} - 2h_x h_y h_{xy}}{2\sqrt{(1+h_x^2+h_y^2)^3}} \\ &= \nabla^2 h \left\{1 + \mathcal{O}\left[(\nabla h)^2\right]\right\} \\ &\approx \mathrm{tr}(h_{ij}) \end{aligned} \tag{3.7}$$

and the Gaussian curvature can then be given by

$$\begin{aligned} K &= \frac{h_{xx}h_{yy} - h_{xy}^2}{(1+h_x^2+h_y^2)^2} \\ &\approx \det(h_{ij}) \end{aligned} \tag{3.8}$$

Hence, based on Helfrich free energy, the Monge representation of a complete membrane patch can be written as

$$F_{Mon} = \int dA_\mathrm{p} \left[\frac{\kappa}{2}\left(\nabla^2 h - c_0\right)^2 + \bar{\kappa}\det(h_{ij})\right] + \int dA_\mathrm{p}\sigma\left(\nabla h\right)^2 \tag{3.9}$$

where $dA = \sqrt{1+(\nabla h)^2}dA_\mathrm{p}$, dA_p is called projected area or frame area, dA is real area.

3.2 Multi-scale simulation of membranes

With the fast development of the ability of modern computers, the recent advances of the studies of complex biological systems are more and more dependent on the computer simulation techniques. Polymers and membranes are supermolecules (many body systems) and both show universal collective behaviors at a mesoscopic level. Simulation skills can help us to investigate many large-scale thermodynamic properties of such meso-scale complex systems, for example, at the aspects of membranes, the liquid-solid like phase transition of lipid membrane from a fluid phase to a hexagonal phase and then to a gel phase, the l_d-l_o phase separation of raft domain formation in lipid mixtures, and the routes of the formation of vesicle fusion and fission, which are applicable to explore the drug encapsulation and drug delivery in body systems [94]. At the aspects of polymers, the coil-globular transition of charged polyelectrolytes, like DNAs, RNAs, or some kinds of chemical polymers, and the collapse transition of polymers.

Because collective behaviors exhibited by our study objects, polymers and membranes, involve many molecules, and bridge a large length and time scales, typically from nm to μm [43]. Therefore, the details of the local structures and short time dynamics of

such systems are often irrelevant so that ones can ignore molecular details of the built units of such systems when they hope to study the large scale collective phenomena. However, atomistic molecular dynamics is also important if ones pay attention to the detailed properties of particular lipid membranes, and the special interactions between lipid and membrane proteins.

Behaviors and processes of membranes involves several different scales of length, time and energy. As a result, various kinds of membrane models are devised and many new simulation techniques are proposed to investigate specific problems at different scales. In this section, we roughly classify them into three scales: microscopy, mesoscopy and continuous macroscopy , and concisely introduce the corresponding simulation models: atomistic Molecular Dynamics (MD) at a $10nm$ scale, coarse-grained methods (explicit-solvent and solvent-free) at a $1\mu m$ scale, and continuous triangular surfaces at a $10\mu m$ scale, which are intuitively shown in Fig. 3.1.

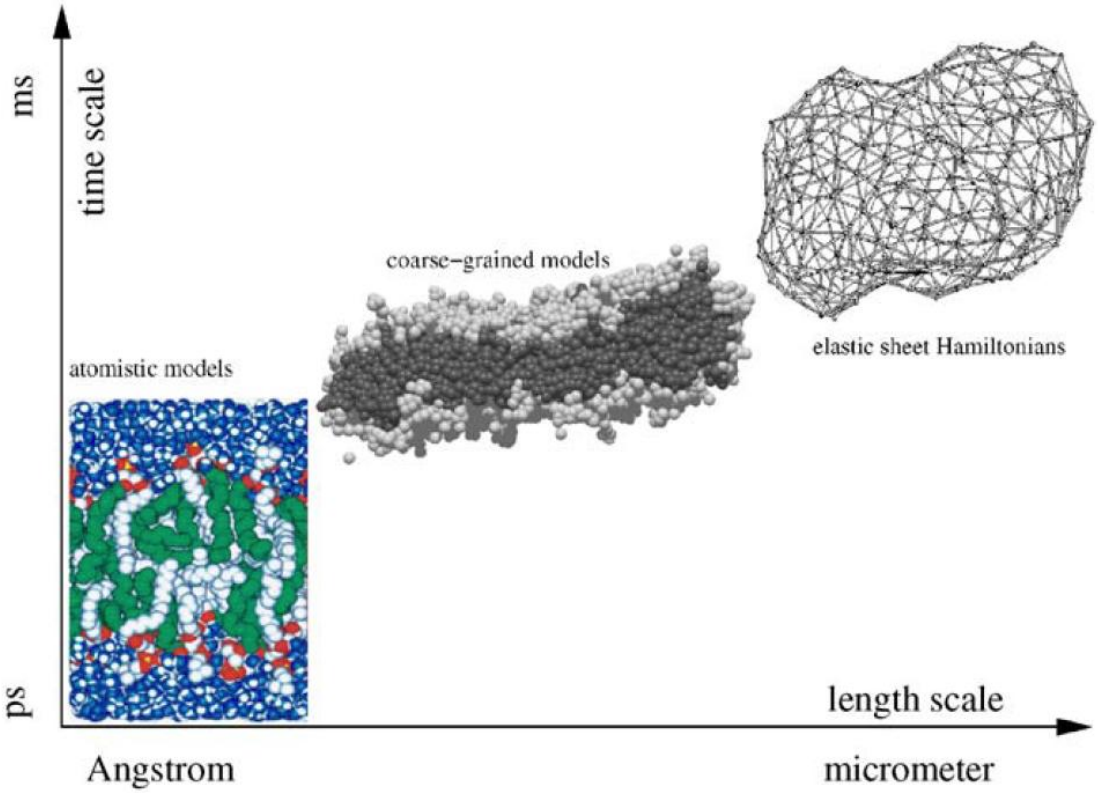

FIGURE 3.1: Three kinds of different scale simulation models are shown. The left snapshot is an atomistic MD simulation, the middle snapshot is a coarse-grained tensionless membrane patch, and the right one is a dynamic triangularization model. Reprinted with permission from Ref. [94].

3.2.1 Atomistic Molecular Dynamics for nanometer scales

Since even one lipid molecule consists of many different kinds of atoms, One mole of them contains $\mathcal{O}\left(10^{23}\right)$ particles, having a extremely huge number of freedom degrees in the extent of classical statistical physics. To be able to study reasonably such systems by Molecular Dynamics, some approximations are necessary. First of all, the freedom degree of electrons are not explicitly taken into account any more. Rather, they are dealt with within the framework of Born-Oppenheimer approximation. For example, it is assumed that the nucleus moves according to the laws of Newtonian mechanics and the electrons follow instantaneously. Although real microscopic world is not classical, classical and quantum statistical mechanics can lead to the same results if and only if the considered particles are stable, which means that typical scale of energy is so small that no bonds among particles are formed or broken. Under this condition, it is possible to find a classical interaction function, which can characterize the statistical properties of systems with the same level of accuracy as a full quantum-mechanical treatment.

A natural way is to derive a classical interaction function from the quantum Hamiltonian by averaging over all degrees of freedom of the electrons. But it is impossible and, thus, we rather use a tailored empirical interaction function instead. This interaction function is defined as a sum of potential energy terms and is called as a force field. The parameters of a force field are determined by comparison with the quantitatively reproduced values of the corresponding experiments which are desirable to simulate. In this sense, ones can construct many different kinds of force fields, whose function forms need to balance between the accuracy and the efficiency.

The first atomistic molecular dynamics method for lipid membranes was born in the early 1990s. It was only able to simulate a tiny patch of membrane bilayer, about $1nm$ and $0.1ns$ [95, 96]. Today there are several famous simulation packages of force fields, including the standard routes for MD simulations, existing to simulate membrane and proteins, such as, NAMD Molecular Dynamics Software (NAMD), the Groningen Machine for Chemical Simulation (GROMACS), Groningen Molecular Simulation (GROMOS), Assisted Model Building with Energy Refinement (AMBER), Large-scale Atomic/Molecular Massively Parallel Simulator (LAMMPS), and so on. The first three packages are suited to simulate lipid bilayers and proteins in the atomistic level, while the latter ones originate from polymer simulations but can also be applied to coarse-grain simulations of soft matters [94]. Differences among these packages are their own ways of information distribution in the processors, the force fields, and the advantages of use and availability of tutorials [94].

Atomistic force field inevitably include Coulomb interactions, which can be calculated by Ewald summation only for very small systems. To speed up this summation, particle-mesh-Ewald techniques which leads to a scaling of the order O(N ln N), with the number of charges, N, or fast multipole expansions which scale linearly with N are usually applied [94].

The advantage of atomistic simulation scheme exists in its detialed description of the microscopic dynamics of the constituents. Therefore, it allows us to explore kinetic processes, for example, the transmembrane transport of small molecules and the lateral diffusion of lipid molecules in the membrane. The MD simulations often use the time-reversible, symplectic Velocity Verlet or Leapfrog algorithms (shown in Chapter 4) and allow for multiple time step integration [94, 97].

An important aspect of atomistic simulations is that they could exhibit the details of the bilayer architecture (e.g., particular head group structure, length, and degree of saturation of the tails) with the corresponding physical properties (thickness, orientation of segments, and elastic moduli). Typically physical properties can be obtained by increasing the system size and simulation time. Ones also can observe the fluctuations of the bilayer membrane. From an analysis of the undulations of the local thickness, one obtains the bending rigidity and area compressibility of the membrane[111,112]. The left snapshot in Fig. 3.1 shows a typical atomistic simulations of a 1-stearoyl- 2-docosahexaenoyl-sn-glycero-3-phosphocholine (SDPC, $18:0/22:6$ PC) lipid bilayer.

3.2.2 Coarse-grained off-lattice models for mesoscopic scales

Although atomistic simulations could give us many valuable aspects about the local structural properties of lipid membranes, they cannot access the sufficient time and length scales for collective membrane phenomena at a larger scale. One way to overcome this shortcoming is to take the coarse-graining way. Coarse-grained models do not attempt to describe the large scale phenomena by starting from the smallest atomic length scale, but directly start from an appropriate mesoscale by using some empirical parameters which should agree with the experimental data. In such models, a small number of atoms are considered into one effective coarse-grained particle. These effective particles then interact by coarse-grained interactions, which typically do not include electrostatic and torsional potentials [94]. This dramatically speeds up the simulation and makes possible the study of collective phenomena for large-scale membranes

When ones enter the realm of coarse-grained models from ab initio simulations, they inevitably ask how to make the coarse-graining procedures and how to keep the relevant degrees of freedom and interactions so that the essential physics of the system can be

reproduced. These fundamental problems should be solved when a successful coarse-grained model is proposed.

3.2.2.1 Explicit solvent model

In this thesis, we only introduce off-lattice coarse-grained models, because without the constraints of the degree of motion freedom these models allow for more flexibility in describing the molecular geometry compared with the lattice models and they can be studied by Molecular Dynamics. Smit et al. [98] proposed a generic off-lattice coarse-grained model to simulate micelle formation, in which water and oil molecules are acted on by Lennard-Jones potentials, while the amphiphile is formed by a group of particles linked via harmonic springs. The hydrophobic beads consist a linear chain tail one by one, while all the hydrophilic head beads are linked to a single, central bead which is attached to one end of the tail. This characterizes the bulkiness of the lipid head. Goetz and Lipowsky constructed another model in which one amphiphiles are composed of a single head bead and four tail segments [99, 100]. A water molecule is represented by a single bead. The interactions between all the beads are Lennard-Jones-like with a cut-off at $r_c = 2.5\sigma$. The hydrophobic interaction between water and tail or head and tail is modeled via a repulsive soft potential. The potentials are truncated and shifted so that both the potential and the force are continuous at the cut-off. Beads in the amphiphile are linked via harmonic springs. Additionally a bending potential is also included to mimic the configuration of a lipid molecule. By increasing the bending coefficient, one can change the conformations from a very flexible lipid molecule to a rigid one. But since this coarse-grained explicit solvent models still have to deal with a large mount of water molecules, the computational speed is still not fast enough to study a larger scale membrane system. Thus, we only introduce such models briefly here. To achieve one faster simulation speed, solvent free models are desired.

3.2.2.2 Solvent free model

A further coarse-graining procedure is to remove the solvent particles but still holding their effects implicitly. Since the 2D membrane is embedded in a 3D space filled with the solvent, if ones investigate larger sizes of systems, the number of solvent particles increases much faster than the number of amphiphiles. However, the solvent actually only play a role to stabilize the bilayer membrane. The interaction between solvent and amphiphiles can be replaced by some effective interactions between the amphiphilic units. Therefore, ones can obtain a huge computational speed-up by eliminate the solvent.

Such implicit solvent models have been widely employed in polymer physics where the behavior of polymers in solvents of different qualities often is described by polymers in vacuum with effective interactions between the monomeric units. Attractive interactions correspond to a poor solvent and lead to a collapse of the polymer, while repulsive interactions correspond to a good solvent because the isolated polymer adopts a swollen, self-avoiding walk like shape.

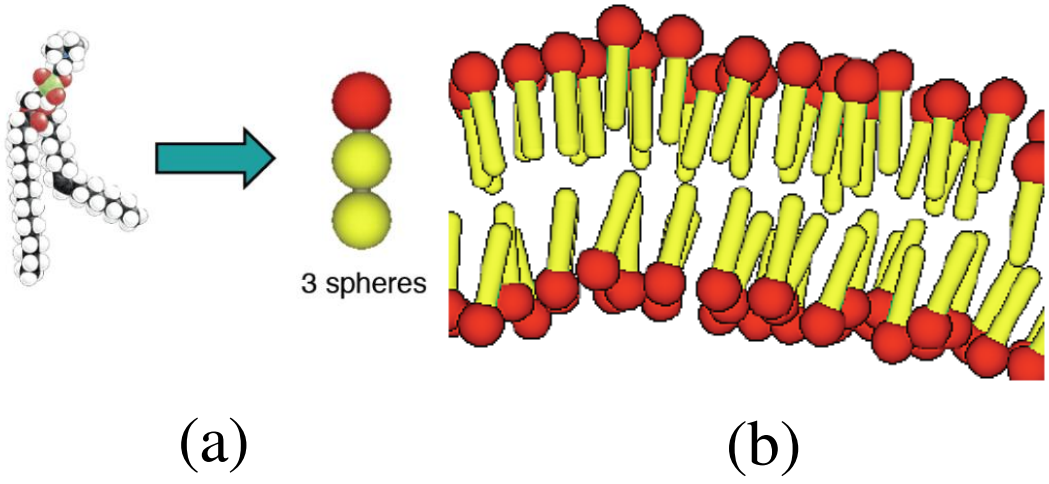

FIGURE 3.2: (a) An atomic amphiphilic lipid molecule can be coarse-grained to the one composed of the hydrophilic head (one red particle) and the hydrophobic tail (two yellow particles). (b) Snapshot of a patch of the bilayer constructed by the coarse-grained three-bead model.

Because the author is only familiar with some models proposed by Nougchi, we will only take his three-bead model as an example here. Noguchi and Takasu [101, 102] modeled one amphiphile molecule composed of three beads, a head and two tail beads (see Fig. 3.2). These beads interact via a rotationally symmetric but multi-body attractive potential for the hydrophobic tail beads is used to stabilize the membrane instead of the solvent effects. Particles repel each other via a soft core potential which defines the energy scale,ϵ, and the monomeric length scale, σ. The potential is of the form

$$U_{\mathrm{rep}}(r) \quad = \quad \epsilon \exp\left[-20(r_{ij}/\sigma - 1)\right] \tag{3.10}$$

and it is truncated and shifted at a cut-off 1.3σ. The multi-body potential takes the form

$$U_{\mathrm{hp}}(\rho)/\epsilon = \begin{cases} -0.5\rho & (\rho < \rho^* - 1) \\ 0.25(\rho - \rho^*)^2 - c & (\rho^* - 1 \leq \rho < \rho^*) \\ -c & (\rho^* \leq \rho) \end{cases} \tag{3.11}$$

with parameters $\rho^* = 10$ and $c = 4.75$ for the tail bead nearest to the head and $\rho^* = 14$ and $c = 6.75$ for the tail bead at the end [101, 102]. The function of a local density, ρ, quantifies the local number of hydrophobic particles in a small sphere around the reference particle at position, $\mathbf{r}$, according to

$$\rho_{i,j} = \sum_{i \neq i', j'=2,3} h(\left|\mathbf{r}_{i,j} - \mathbf{r}_{i',j'}\right|) \tag{3.12}$$

with

$$h(r) = \begin{cases} 1 & (r \leqslant 1.6\sigma) \\ \frac{1}{\exp[-20(r_{ij}/\sigma - 1.9)+1]} & (1.6\sigma \leq r < 2.2\sigma) \\ 0 & (2.2\sigma \leq r) \end{cases} \tag{3.13}$$

At small local densities, $\rho < \rho^* - 1$, the multi-body potential is linear in the density and, thus, represents a pairwise attraction between neighboring hydrophobic beads on different molecules. At higher densities, the attractive strength levels off and adopts a constant value independent of the local density. This feature avoids the collapse of the hydrophobic tails into extremely dense structures and thus prevents crystallization. This model are used to mimic the bilayer composed of two layers of amphiphilic molecules.

3.2.3 Continuous surfaces constructed by dynamic triangulation

Since membranes can be considered as 2D random surface, people tried to construct random triangulated models to model random fluctuating surfaces. A construction strategy and a typical snapshot are presented in the Fig. 3.3 (a) and (b). The vertices are connected by bonds. If the bond connection is fixed, the membrane only show elastic deformation that is characteristic of polymerized membranes. If the bonds are permitted to change during the simulation (dynamic triangulation) [103–108], one can mimic the membrane fluidity. The vertices are able to diffuse in this type of fluid membrane. The self-avoidance of the membrane is modeled by an excluded volume interaction between vertices. The strength and range of the excluded volume interaction and the interactions along bonds can be chosen in order to avoid crossings. Let $\mathbf{n}_i$ denote the normal to a triangle facet, i. The discretization of the mean curvature, $H = \mathbf{n} \cdot \Delta\mathbf{R}$ at vertex i takes the form

$$H_i = \frac{1}{\sigma_i}\mathbf{n}_i \cdot \sum_{j \in n.n.(i)} \frac{\sigma_{ij}}{l_{ij}} (\mathbf{R}_i - \mathbf{R}_j) \tag{3.14}$$

where the sum runs over all tethers ij that are connected to the vertex i. The length of such a tether is l_ij , $\sigma_{ij} = l_{ij}(\cot\Theta_1 + \cot\Theta_2)/2$ is the length of the corresponding bond

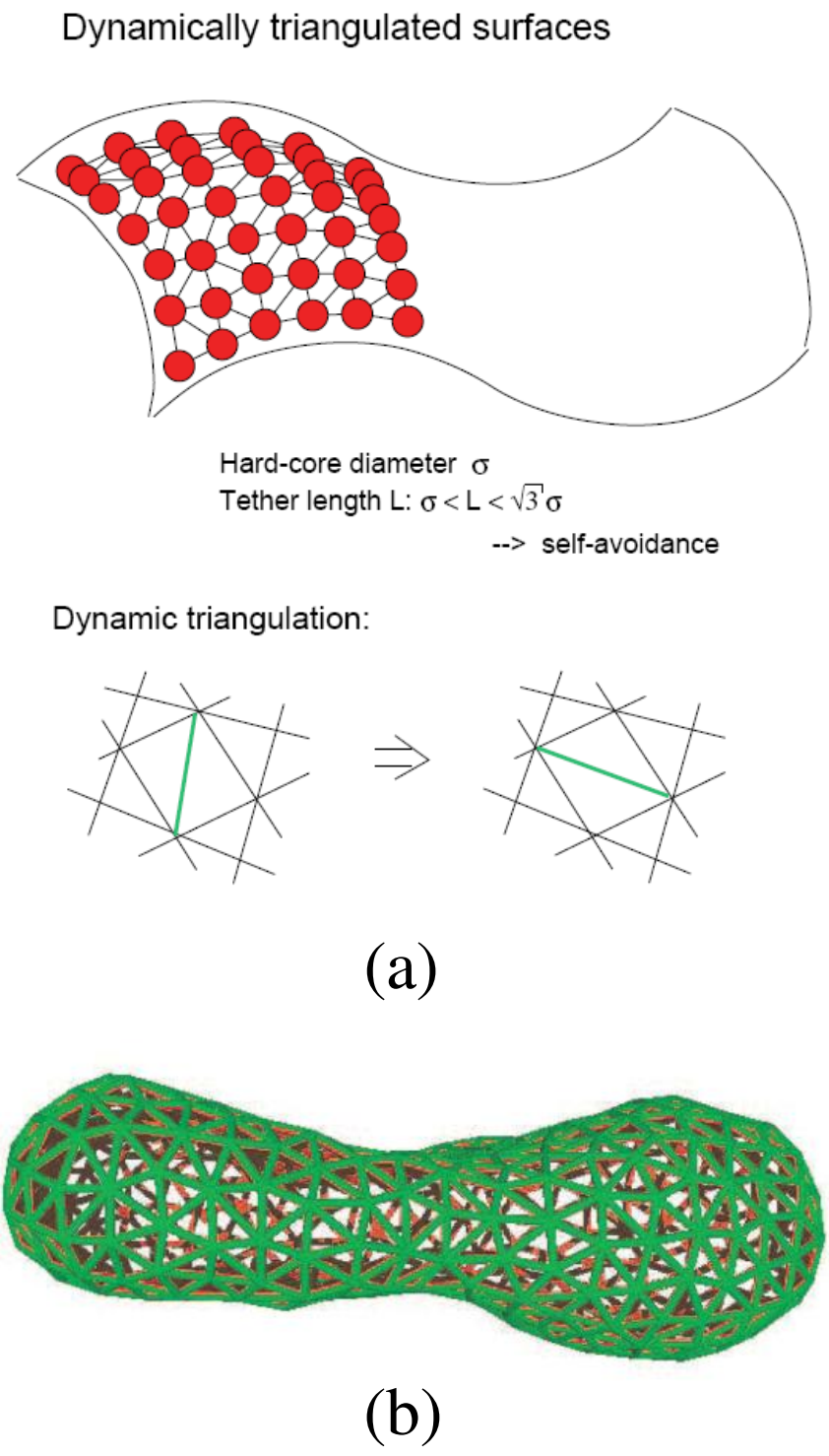

FIGURE 3.3: A dynamic triangulation model of a fluctuating surface is shown. (a) shows that hard spheres connected by bonds of maximum extension L are used to describe self-avoiding membranes. And the Monte Carlo step, which makes the triangulation dynamic, is required to model fluid membranes. While (b) is a snapshot for the dynamic triangulation of a red blood cell with the biconcave shape. Reprinted with permission from Ref. [103].

in the dual lattice which is created from the intersections of the perpendicular bisectors of the bonds. Θ_1 and Θ_2 are the angles opposite to the link ij in the two triangles that border the link. The quantity $\sigma_i = \frac{1}{4}\sum_{j\in n.n.(i)} \sigma_{ij} l_{ij}$ represents the area of the virtual dual cell. Using this expression and the fact that the local normal $\mathbf{n}$ is collinear to $\Delta\mathbf{R}$ in three dimensional space, one obtains the discrete Helfrich free energy with free surface tension as follows:

$$\mathcal{H} = \frac{\kappa}{2}\sum_i \frac{1}{\sigma_i}\left[\sum_{j\in n.n.(i)} \frac{\sigma_{ij}}{l_{ij}}(\mathbf{R}_i - \mathbf{R}_j)\right]^2 \tag{3.15}$$

where the integral over the Gaussian curvature is omitted because it is just a constant when the topology is conserved.

If all triangles are equilateral, $\sigma_{ij} = l_{ij}/\sqrt{3}$, Eq. (3.15) above reduces to

$$\begin{aligned}\mathcal{H} &= \frac{\sqrt{3}\kappa}{2}\sum_{\langle\alpha,\beta\rangle}(\mathbf{n}_\alpha - \mathbf{n}_\beta)^2 \\ &= \sqrt{3}\kappa\sum_{\langle\alpha,\beta\rangle}(1 - \mathbf{n}_\alpha\cdot\mathbf{n}_\beta)\end{aligned} \tag{3.16}$$

To study fluid membranes, the connectivity of the membrane vertices cannot be fixed during the simulation, otherwise this model cannot mimic the diffusion of lipids in the membrane. So the dynamic triangulation ensure the occurrence of the internal diffusion. The essential step of this dynamic procedure is shown in Fig. 3.3 (a). Among the four vertices of two neighboring triangles, the diagonal bond is switched from one of the two possible positions to the other. This bond-switching is allowed if the vertices remain connected to at least three neighbors after the switch. At the same time, an additional requirement is that the new connected bond length has to be smaller than the maximum bond length. The advantages of this Monte Carlo scheme are that it is local between only the vertices of two neighboring triangles, and it guarantees the whole triangulation network still to be 2D connected [103].

3.3 Physics of polymers

A real polymer is a macromolecule composed of thousands of small molecules.It is chemically a group or mixture of compounds consisting of repeating structural units, which are covalently connected, created by a series of polymerization processes. Generally, the backbone structure of polymers is supported by carbon atoms C-C. The simplest example of polymers is polyethylene. In physics, for the simplicity, ones assume a model

polymer chain consist of a large number of the same kind of monomers (homopolymer) or different kinds of monomers (heteropolymer or block polymer).

The mesoscopic length is significant to understand soft matter, such as polymers. Thus, we can deal with polymer problems by using some suitable coarse-grained methods, but without considering every details, e.g. the chemical components, in their atomistic level from the view of point on the modeling construction theory. It makes that ones do not have to study from the characters of the construction units of polymer chains, thus, physicists can predict many universal characters from the topological properties of polymers, considered as a piece of disjoint string, at large scale. As a result, ones can understand a large number of related characters of polymers by only their geometric structure and statistical properties, but not their energetic quantities.

3.3.1 Ideal chains

A single polymer chain can be characterized by a simplest model, the freely joint chain model. Each monomer is considered as a point-like particle and linked by a bond with a length b, which is called Kuhn length. The probability distribution of one single bond is given by

$$p\left(\mathbf{r}_{n+1}-\mathbf{r}_{n}\right)=p\left(\left|\mathbf{R_n}\right|\right)=\frac{\delta\left(\left|\mathbf{R_n}\right|-\mathbf{b}\right)}{4\pi b^{2}} \tag{3.17}$$

where $\mathbf{r}_n$ is the spatial position of the n-th monomer.

An important quantity is the end-to-end vector $\mathbf{R}_{\mathrm{e}}$ of the polymer chain. It can be used to evaluate the relative spatial position of the first and the end monomers of a polymer chain. Since it points all directions with equal probability, the average end-to-end vector is zero, that is, $\langle\mathbf{R}_{\mathrm{e}}\rangle=0$. However, the interesting quantity is the average of the squared end-to-end vector as given by

$$\langle\mathbf{R}_{\mathrm{e}}^{2}\rangle=\langle(\sum_{\mathrm{n}}\mathbf{R}_{\mathrm{n}})^{2}\rangle=Nb^{2} \tag{3.18}$$

The end-to-end distance can be defined as [109]

$$R_{\mathrm{e}}=\sqrt{\langle\mathbf{R}_{\mathrm{e}}^{2}\rangle}=b\sqrt{N} \tag{3.19}$$

We define the mean square radius of gyration ${R_{\mathrm{g}}}^2$ of the polymer as

$$\langle R_{\mathrm{g}}^{2}\rangle \;=\; \frac{1}{N}\sum_{\mathrm{n}=1}^{N}\langle(\mathbf{R}_{\mathrm{n}}-\mathbf{R}_{G})^{2}\rangle \tag{3.20}$$

where $\mathbf{R}_G$ is the position of the center of mass of the polymer chain:

$$\mathbf{R}_G = \frac{1}{N}\sum_{\mathrm{n}=1}^{N}\mathbf{R}_{\mathrm{n}} \tag{3.21}$$

For a linear Gaussian polymer, R_{g}^2 is easily evaluated as follows:

$${R_{\mathrm{g}}}^2 = \frac{1}{6}\langle \mathbf{R}_{\mathrm{e}}^2 \rangle = \frac{1}{6}Nb^2 \tag{3.22}$$

Thus, R_{g} is given by $R_{\mathrm{e}}/\sqrt{6}$ for a linear Gaussian polymer chain.

Both radii of end-to-end distance R_{e} and gyration R_{g} can be applied to measure the polymer size.

The above calculations are based on random walk in 3D space without any constraint. Ones call this kind of polymers as ideal polymer chains.

3.3.2 Excluded-volume chains

In solvent-free polymer simulations, ones usually consider the non-bonded long range interactions between the monomers as well as between monomers and solvent particles, the available space for the polymer chain is approximately replaced by the introduction of an excluded volume. In this type of models, each polymer monomer cannot be regarded as a point-like particle, but occupies a certain spatial volume. Such polymer chain is a self-avoiding walk obtaining a more extended conformation compared with a freely joint chain model. So we easily understand that the size of an excluded-volume polymer chain should be elongated larger compare with an ideal polymer chain due to the steric repulsion. This is reflected in a larger scaling exponent which now becomes $\nu = 0.6$ (a more exact numerical calculation gave us $\nu = 0.588$ [110]). The excluded volume effect can be involved into a model by a repulsive potential, U_{rep}, which describes the interactions between non-connected units along the chain and prevents them from overlapping. Besides this short range steric repulsion, the effective interaction between two monomers also include a long range attraction. If we denote r as the distance between two monomers, the interaction potential between them can be written to be $\sim 1/r^6$ [111]. A very popular potential which models the combination of these two effects is just the Lennard-Jones potential [112]:

$$U_{\mathrm{LJ}}(r_{ij}) = 4\epsilon\left[\left(\frac{\sigma_{\mathrm{LJ}}}{r_{ij}}\right)^{12} - \left(\frac{\sigma_{\mathrm{LJ}}}{r_{ij}}\right)^{6}\right], \tag{3.23}$$

where $r_{ij} = |\mathbf{r}_i - \mathbf{r}_j|$ is the distance between the ith and jth units, σ_{LJ} is a measure of the effective size of a monomer and ϵ is the Lennard-Jones parameter characterizing the strength of the interaction. A large ϵ for the inter-bead potential represents that the polymer tends to effectively minimize its interface with the solvent and such polymer solution is in a bad or poor solvent condition and conversely for a small ϵ, regarded as a good solvent condition.

This type of more practical model is called excluded-volume chains, which is constructed on the basis of the self-avoiding walk.

3.3.3 Polymer mushroom and brush

The above theoretical models primarily show a free polymer molecule in solution, but in many practical applications of interest, the polymer inevitably has an end anchored with a surface. A single flexible polymer chain or a dilute polymer-chain layer in a good solvent at equilibrium forms a structure often called a "mushroom. For polymers anchored at a high density, a mushroom conformation will be suppressed into a brush, describing the more stretched-out conformations due to excluded volume forces. In terms of the mean field theory by de Gennes [113], the equilibrium height, h_0, of a polymer brush layer on the flat surface in a good solvent is proportional to N

$$h_0 = N\Gamma^{1/3} \tag{3.24}$$

where Kuhn length is set to 1, and Γ is the surface coverage. In Section 3.4.3 we will see the derivation of Eq. (3.24).

3.4 Polymer-induced mechanical properties of membranes

3.4.1 Mechanical properties induced by a single polymer

Due to the constraint from membrane substrate, a polymer with an end anchored onto a surface will involve a loss of configuration entropy of the polymer chain. In Fig. 3.4, we show a schematic picture where a flexible polymer is linked to a patch of 2D membrane. Then three kinds of shapes of the membrane patch could be induced: cone, spherical cap, and catenoid. In the idealized situation of a flat substrate, the polymer is confined to the half-space and, thus, loses entropy because it cannot explore the half-space on the other

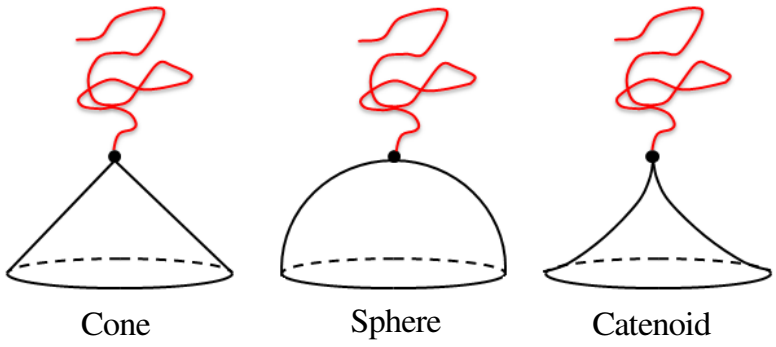

FIGURE 3.4: Schematic picture of anchored-polymer-induced entropic effects on membrane, three possible membrane deformations induced by a flexible anchored polymer are shown.

side of the substrate [114]. In order to anchor the polymer on the surface it is necessary to compensate the entropic effect by a chemically induced energy gain due to the grafting. If this energy is smaller than the entropy loss, the polymers will leave away from the surface. Conversely, if the energy is large compared to the entropy decrease, polymers will stay at the surface for a long time. For a large reservoir of polymers, in principle, this anchoring will lead to very large coverage densities. However, for large densities the steric interaction of the polymer chains provides an additional entropy decrease which balances the anchoring energy and leads to an equilibrium coverage density of polymers on the surface. The situation is similar if the polymers are anchored on the membrane. If the membrane is initially flat, the anchoring energy in the lipid bilayer has to compete with the entropy decrease. Since the membrane is a flexible object, the anchoring of the polymer leads to a change in the membrane shape in such a way that the membrane bends away from the polymer. Consequently the polymer obtains more configuration space.

Generally the effect of the addition of macromolecules to membrane systems can be described by the effective elastic moduli, which is the summation of bare membrane elastic moduli and excess elastic moduli as follows:

$$\begin{aligned} c_0 &= c_{0,\mathrm{mem}} + \Delta c_0 \\ \kappa_{\mathrm{eff}} &= \kappa_0 + \Delta\kappa \\ \bar{\kappa}_{\mathrm{eff}} &= \bar{\kappa}_0 + \Delta\bar{\kappa} \end{aligned} \tag{3.25}$$

where $c_{0,\mathrm{mem}}$, κ_0, and $\bar{\kappa}_0$ are the elastic moduli for pure membranes.

If one considers the curvature of the membrane to be small one can expand the polymers entropy difference by using the membrane curvature, and the flat situation in powers of the curvature up to second order, which leads to [23]

$$\Delta S_{\mathrm{p}} = b_1 R_{\mathrm{e}} H + b_2 \left(R_{\mathrm{e}} H\right)^2 + b_3 R_{\mathrm{e}}^3 K \tag{3.26}$$

When we solve the problem for a polymer anchored on a flat surface, on a sphere and on a cylinder, we can obtain three prefactors up to the second order expansion of the curvature [23, 24]

$$b_1 = \sqrt{\frac{\pi}{6}},\ b_2 = -\left(\frac{\pi}{12} + \frac{1}{6}\right),\ b_3 = \frac{1}{6} \tag{3.27}$$

Since the first coefficient b_1 is positive the polymer gains entropy if the membrane bends away from it. Calculation of the spontaneous curvature c_0 leads to

$$c_0 \approx T \frac{b_1}{4\kappa_{\mathrm{eff}} R_{\mathrm{e}}} \approx 0.18 \frac{T}{\kappa_{\mathrm{eff}} R_{\mathrm{e}}} \tag{3.28}$$

where T is the temperature measured in energy units and the curvature is defined as positive if the membrane bends away from the polymer.

3.4.2 Mechanical properties induced by polymer mushroom

There are two cases for the formation of polymer mushroom. One is formed by ideal polymer chains without caring the anchored polymer density, the other is formed by excluded-volume chains at the low enough densities which have to make sure that anchored polymers do not overlap with each other. For the region of polymer mushroom, we can extend the above theoretical predictions for a single idea polymer chain to describe the effective mechanical properties of membranes by introducing a lateral area A in order to guarantee the correct units of the mean curvature H and spontaneous curvature c_0. Thus, we have

$$A c_0 = \frac{k_{\mathrm{B}} T}{4\kappa_{\mathrm{eff}}} \sqrt{\frac{\pi}{6}} R_{\mathrm{e}} \tag{3.29}$$

Because the anchored polymer density σ is considered as $1/A$, we obtain

$$\begin{aligned} \kappa_{\mathrm{eff}} c_0 &= \frac{k_{\mathrm{B}} T}{4} \sqrt{\frac{\pi}{6}} \sigma R_{\mathrm{e}} \\ &\approx 0.18 k_{\mathrm{B}} T \sigma R_{\mathrm{e}} \end{aligned} \tag{3.30}$$

Following the similar procedures, we can obtain [26, 115]

$$\begin{aligned} \Delta\kappa &= \frac{k_{\mathrm{B}}T}{6}\left(1+\frac{\pi}{2}\right) \\ &\approx 0.21 k_{\mathrm{B}}T\sigma R_{\mathrm{e}}^2 \end{aligned} \tag{3.31}$$

$$\begin{aligned} \Delta\bar{\kappa} &= -\frac{k_{\mathrm{B}}T}{6}\sigma R_{\mathrm{e}}^2 \\ &\approx -0.17 k_{\mathrm{B}}T\sigma R_{\mathrm{e}}^2 \end{aligned} \tag{3.32}$$

where σ is the number density of chains per membrane area, and three coefficients 0.18, 0.21, and -0.17 are estimated by theory. The more exact expressions, including the polymer contour length, are obtained by Monte Carlo simulation [26, 115]

$$\begin{aligned} \kappa_{\mathrm{eff}}c_0 &= a_{\mathrm{sp}}k_{\mathrm{B}}T\sigma R_{\mathrm{e}} \\ \Delta\kappa &= a_{\kappa}k_{\mathrm{B}}T\sigma R_{\mathrm{e}}^2 \\ \Delta\bar{\kappa} &= a_{\bar{\kappa}}k_{\mathrm{B}}T\sigma R_{\mathrm{e}}^2 \end{aligned} \tag{3.33}$$

with

$$\begin{aligned} a_{\mathrm{sp}} &= 0.1801(1-0.369N^{-1/2}) \\ a_{\kappa} &= 0.2130(1-0.870N^{-1/2}) \\ a_{\bar{\kappa}} &= -0.1682(1-1.179N^{-1/2}) \end{aligned} \tag{3.34}$$

For the low density of anchored excluded-volume polymer chains, the expressions have the same forms as Eqs (3.33), and the exact coefficients are written as

$$\begin{aligned} a_{\mathrm{sp}} &= 0.1679(1-0.391N^{-1/2}) \\ a_{\kappa} &= 0.1997(1-0.972N^{-1/2}) \\ a_{\bar{\kappa}} &= -0.1532(1-1.221N^{-1/2}) \end{aligned} \tag{3.35}$$

3.4.3 Mechanical properties induced by polymer brush

When the mean distance between the anchor points of excluded-volume polymer chains is less than the radius of the polymer coil, the polymers will overlap and form a so-called polymer brush due to the steric confinement by the neighboring chains. In the region of polymer brush, we need to calculate the polymer-induced mechanical properties of membrane by using a scaling theory based on the blob picture (as shown in Figs. 3.5 and 3.6).

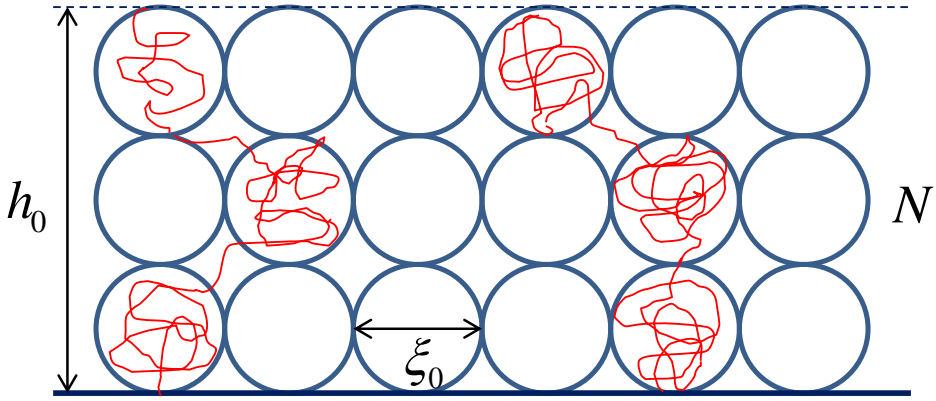

FIGURE 3.5: Scaling picture of a polymer brush on a flat surface is shown. The height of the brush layer on the flat surface is h_0, and each blob contains N segments. The distance between two nearest blobs are ξ_0.

The distance between the grafting points is denoted by ξ_0. Then it is convenient to introduce a reduced surface coverage Γ given by

$$\Gamma \equiv \left(\frac{b}{\xi_0}\right)^2 \tag{3.36}$$

which gives us a dimension less number of polymer chains per unit area, and b represents a generic kuhn length of a polymer chain mentioned in Section 3.3.1. The reduced overlap coverage scales as $\Gamma \sim N^{-2\nu}$.

On a flat surface shown in Fig. 3.5, each blob is of radius ξ_0 and contains $N_1 = (\xi_0/b)^{1/\nu}$ segments. The height of polymer brush layer on the flat surface is denoted by h_0, then the blob number is h_0/ξ_0, and the layer segment satisfies

$$N = h_0 \left(\frac{\xi_0}{b}\right)^{1/\nu} \frac{1}{\xi_0} \tag{3.37}$$

Thus, we obtain

$$h_0 = bN\Gamma^{(1-\nu)/2\nu} \tag{3.38}$$

when $\nu = 0.6$ for excluded-volume chains, the above expression can be written as $h_0 = bN\Gamma^{1/3}$, which just reflects a scaling relation Eq. (3.24) obtained by de Gennes.

We have to expand the scaling argument for a brush anchored on spherical and cylindrical surfaces to obtain the bending rigidity and spontaneous curvature. Let us denote the size of blobs by ξ_s and ξ_c for spherical and cylindrical surfaces, respectively. In the first layer the surface area is given by $S(r) \approx X\xi_i(r)^2$, where X is the number of anchored polymer chains, i = s and c for spherical and cylindrical geometries.

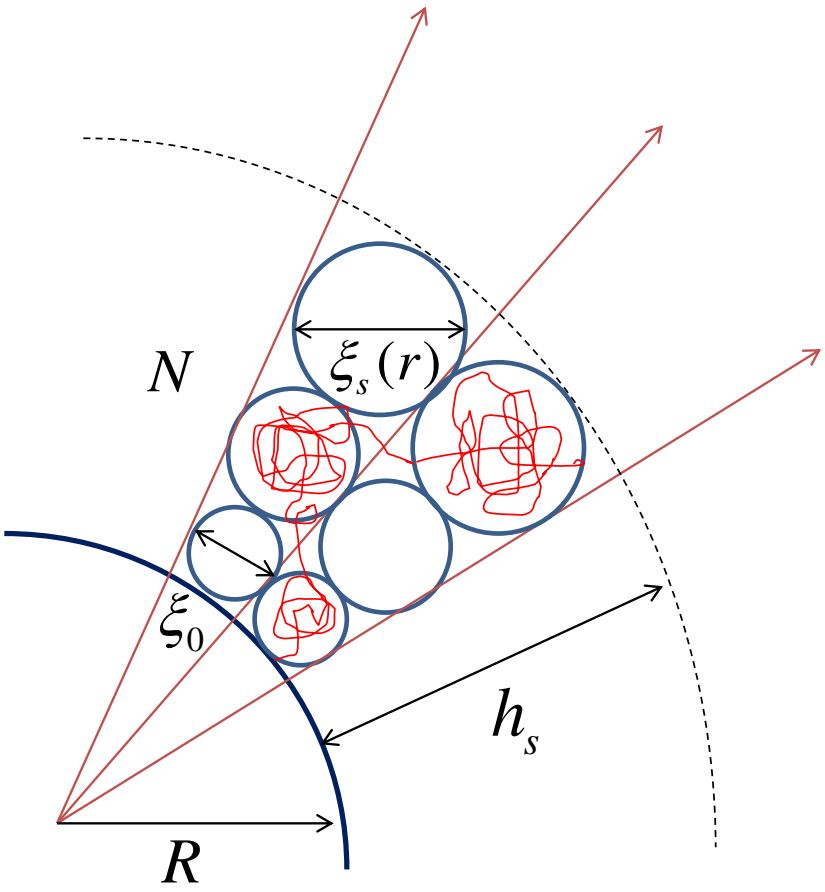

FIGURE 3.6: Scaling picture of a polymer brush on a sphere of radius R. The height of the brush layer on the spherical surface is $h_s(R)$, and each blob contains N segments. The distance between two nearest blobs are $\xi_s(r)$.

For a sphere of radius R shown in Fig. 3.6, $S(r) = 4\pi r^2$ and $X = 4\pi R^2/\xi_0^2$, where ξ_0 means the distance between anchored points on the spherical surface. By using these relations, we obtain the blob size as

$$\xi_s(r) = \frac{\xi_0 r}{R} \tag{3.39}$$

If the brush height on spherical surface is h_s, then it is implicitly given by

$$N = \int_R^{R+h_s} dr \left(\frac{\xi_s(r)}{R}\right)^{1/\nu} \left(\frac{1}{\xi_s(r)}\right) \tag{3.40}$$

This leads to

$$h_0 = \nu R \left[\left(1 + \frac{h_s(R)}{R}\right)^{1/\nu} - 1\right] \tag{3.41}$$

Solving this equation for h_s, we have

$$h_s = R\left[\left(1+\frac{h}{\nu R}\right)^{\nu} - 1\right] \tag{3.42}$$

Similar to the spherical surface, the surface area of a cylinder is $S(r) = 2\pi Dr$ and $X = 2\pi DR/\xi_0^2$, therefore

$$\xi_c(r) = \frac{\xi_0 r^{1/2}}{R^{1/2}} \tag{3.43}$$

Then the brush height on cylindrical surface h_c is obtained as

$$h_c = R\left[\left(1+\frac{(1+\nu)h}{2\nu R}\right)^{2\nu/(1+\nu)} - 1\right] \tag{3.44}$$

In the scaling picture, the free energy per polymer chain is proportional to the number of blob, so it can generally be calculated as

$$F = k_B T \int_R^{R+h} dr 1/\xi(r) \tag{3.45}$$

where F represents free energies F_0, F_s, F_c per unit area on the flat surface, spherical surface and cylindrical surface, and h represents heights h_0, h_s, h_c on the flat surface, spherical surface and cylindrical surface, respectively.

Following this procedure, the free energies F_0, F_s, F_c per unit area on the flat surface, spherical surface and cylindrical surface can be obtained, respectively, as

$$F_0 = k_B T \Gamma^{1/2} h_0/b \tag{3.46}$$

$$F_s = \left(\frac{k_B T \Gamma^{1/2} R\nu}{b}\right) \ln\left(1+\frac{h_0}{\nu R}\right) \tag{3.47}$$

$$F_c = \left(\frac{2k_B T \Gamma^{1/2} R}{b}\right)\left[\left(1+\frac{(1+\nu)h_0}{2\nu R}\right)^{\nu/(1+\nu)} - 1\right] \tag{3.48}$$

The differences of the brush free energy per polymer on the curved surfaces (of sphere and cylinder) and a flat surface at a fixed polymer density are

$$\Delta F_s = F_0 f_s\left(h_0/R\right) \tag{3.49}$$

with

$$f_{\mathrm{s}} = \frac{\nu}{x} \ln\left(1 + \frac{x}{\nu}\right) - 1$$

and

$$\Delta F_{\mathrm{c}} = F_0 f_{\mathrm{c}} \left(h_0/2R\right) \tag{3.50}$$

with

$$f_{\mathrm{c}} = \frac{1}{x}\left[\left(1 + \frac{1+\nu}{\nu}x\right)^{\nu/(1+\nu)} - 1\right] - 1$$

The excess free energy of the polymer brush ΔF is balanced by the bending energy of a membrane patch. Here the the corresponding membrane patch is measured by the polymer segment b and can be written as $A = b^2\Gamma^{-1}$. The bending energy is written

$$\Delta E_{\mathrm{b}} = 2\kappa\Gamma^{-1}\left(bH\right)^2 + \bar{\kappa}\Gamma^{-1}b^2K \tag{3.51}$$

up to the second order in the principal curvatures.

For a cylindrical surface, the Gaussian curvature $K = 0$, and the mean curvature $H = 1/2R$. Thus, ΔF_{c} depends only on H and spontaneous curvature c_0 can be obtained by minimizing ΔF_{c} with respect to H. It leads to an implicit equation

$$\frac{f_{\mathrm{c}}(x)}{x} + \frac{4\kappa_0 x}{k_{\mathrm{B}}TN^3\Gamma^{3/2\nu}} = 0 \tag{3.52}$$

where $x = h_0c_0$.

When the anchored polymer density is low for excluded-volume polymer chains, we assume the deformation of membrane surface is small, so we can expand the excess free energies for spherical and cylindrical surfaces by small curvature h_0H up to the second order. This leads to

$$\Delta F_{\mathrm{s}} = F_0\left[-\frac{1}{2\nu}\left(h_0H\right) + \frac{1}{3\nu^2}\left(h_0H\right)^2 + \mathcal{O}\left(\left(h_0H\right)^3\right)\right] \tag{3.53}$$

and

$$\Delta F_{\mathrm{c}} = F_0\left[-\frac{1}{2\nu}\left(h_0H\right) + \frac{\nu+2}{6\nu^2}\left(h_0H\right)^2 + \mathcal{O}\left(\left(h_0H\right)^3\right)\right] \tag{3.54}$$

By minimizing the expression for the cylindrical case, we obtain $h_0H = 3\nu/(2\nu+4)$. Therefore, the expression must break down for $h_0H \lesssim 3\nu/(2\nu+4)$.

By combining the expressions (3.51), (3.53), and (3.54), we obtain

$$\kappa_{\text{eff}} = \kappa_0 + \frac{\nu+2}{12\nu^2} N^3 \Gamma^{3/2\nu} k_{\text{B}} T \tag{3.55}$$

and

$$\bar{\kappa}_{\text{eff}} = \bar{\kappa}_0 - \frac{1}{6\nu^2} N^3 \Gamma^{3/2\nu} k_{\text{B}} T \tag{3.56}$$

By using an approximate effective bending rigidity κ_{eff} of Eq. (3.55), we can obtain an approximate spontaneous curvature expression from Eq. (3.52)

$$bc_0 = \frac{1}{8\nu} N^2 \Gamma^{(\nu+2)/2\nu} \frac{k_{\text{B}} T}{\kappa_{\text{eff}}} \tag{3.57}$$

A very detailed derivation of all the equations above is shown in Appendix A.

Chapter 4

Simulation of Biomembranes

In this thesis, we employ a coarse-grained meshless membrane model with anchored linear polymer chains [42, 46]. One membrane particle possesses only a translational degree of freedom. The membrane particles form a quasi-two-dimensional (2D) membrane according to a curvature potential based on the moving least-squares (MLS) method [42]. The meshless membrane model can simulate many universal properties at a quite large scale, that is, which is a discrete off-lattice version of triangular lattice membrane model and has the same ability to simulate the same large scale. By using the meshless membrane model, geometric and topological properties of membranes can be conveniently controlled. Then we constructed a minimal biomembrane model based on this meshless model by adding anchored polymers to investigate the properties of biomembranes. Polymer particles are linked by a harmonic potential, and freely move as a self-avoiding chain with a soft-core repulsion. One end of each polymer chain is anchored on a single membrane particle with a harmonic potential and a soft-core repulsion [46].

4.1 Meshless biomembrane model

We consider a single- or multi-component membrane composed of N_{mb} membrane particles. Among them, N_{chain} membrane particles are anchored by polymer chains. Each polymer chain consists of N_{p} polymer segments with an anchored membrane particle. The membrane and polymer particles interact with each other via a potential

$$U_{\mathrm{tot}} = U_{\mathrm{rep}} + U_{\mathrm{mb}} + U_{\mathrm{p}} + U_{\mathrm{AB}}, \tag{4.1}$$

where U_{rep} is an excluded-volume potential, U_{mb} is a membrane potential, U_{p} is a polymer potential, and U_{AB} is a repulsive potential between different species of membrane particles in two-component membranes.

To simulate self-assembly dynamics and control topological structures of membranes or vesicles at large scales, we employ a most coarse-grained degree of solvent free MD simulation, called meshless (mls) membrane model, combining with linear Gaussian polymer chains, to simulate various phenomena occurring on biomembranes at the mesoscopic scale. One particle typically represents a patch of membrane bilayers.

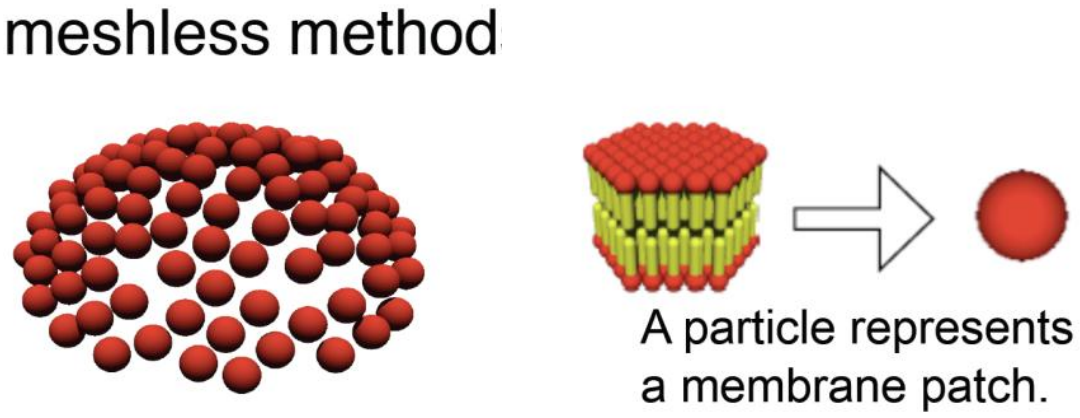

FIGURE 4.1: Coarse-grained meshless membrane model is shown here, where one particle represents a patch of bilayer.

4.1.1 Soft-core repulsive potential

In our simulation, a modified Stillinger-Weber type potential is applied to play the role of soft-core repulsion. Since our simulation does not consider the contribution from bond angle to the repulsive potential, we only revise a two-body term of Stillinger-Weber (SW) potential to produce a pairwise repulsive force. Nevertheless, SW potentials based on the concepts (using only geometrical quantities such as distances and bond angles as variables) are also currently used in simulations of organic systems, where they are usually called force fields. In spite of the limited transferability, which makes it difficult to change the topology of a molecule by breaking and reforming bonds, or to work at high temperatures or pressures, they are capable of modeling with a very high precision the structural and dynamical properties of a large variety of molecules, and are therefore vastly used in research and industry. Here we take a most successful example that SW potentials are widely used in the LAMMPS program package. In the SW potentials, the interaction energies become negligibly small at atomic separations substantially less than the theoretical cutoff distances. This advantage of SW potential itself has no need to be truncated as Leonnard-Jones potential at cutoff distances.

All particles have a soft-core excluded-volume potential with a diameter of σ.

$$U_{\text{rep}} = \varepsilon \sum_{i<j} \exp\left[-20(r_{ij}/\sigma - 1) + B\right] f_{\text{cut}}(r_{ij}/\sigma) \tag{4.2}$$

in which r_{ij} is the distance between membrane (or polymer) particles i and j. The diameter σ is used as the length unit, $B = 0.126$, and $f_{\text{cut}}(s)$ is a C^{∞} cutoff function

$$f_{\text{cut}}(s) = \begin{cases} \exp\left\{A\left[1 + \frac{1}{(|s|/s_{\text{cut}})^n - 1}\right]\right\} & (s < s_{\text{cut}}) \\ 0 & (s \geqslant s_{\text{cut}}) \end{cases} \tag{4.3}$$

with $n = 12$ denotes a 12th order smooth function, $A = 1$, and $s_{\text{cut}} = 1.2$.

4.1.2 Multi-body attraction for solvent free

Typical solvent free (or implicit solvent) models eliminate the explicit occurrence of solvent (usually water) in the models and replace it by effective interactions between the existing solute particles, thus dramatically decreasing the number of degrees of freedom one needs to simulate. The implicit solvent is a common trick in coarse-grained polymer simulations, but it took longer time to be adopted in the simulations of membranes. Different from polymers, membranes are self-assembled aggregates, for which the forces that keep them together originate from the very component ones want to dismiss [116]. Although this is not impossible or forbidden, one needs more care when choosing the effective interactions, as will be seen in a moment.

Water plays a crucial role in the formation of membranes since water provides hydrophobic effect to produce membrane. In the absence of water, coarse-grained lipids need another source of cohesive force in order to form a condensed phase [116].

This unknown effective force field should be a very complicated function, but obviously not a simply linear superposition of pairwise Lennard-Jones interactions because the attractive force range of standard 12-6 Lennard-Jones potential is too short. Thus, we need to find strong enough phenomenological attractive interactions so that it can suppress lipids out of a three-dimensional gas phase into a two-dimensional condensed liquid phase.

A liquid phase requires both sufficient cohesion so as to compete with the much larger entropy of the gas phase, as well as simultaneously requires a sufficient amount of entropy to compete with the free energy of the solid phase. Not all interaction potentials meet these requirements. A natural idea is to apply some kinds of many-body potentials instead of the solvent degrees of freedom. It has to satisfy some nontrivial constraints

that ones have never see when they studied polymeric systems by using solvent-free method [94, 116].

To replace water to produce a source of cohesion in order to form a condensed phase produce, an attractive multibody potential with a relatively simple expression is employed here to mimic the "hydrophobic" interaction.

$$U_{\mathrm{att}}(\rho_i) = 0.25 \ln \{1 + \exp[-4(\rho_i - \rho^*)]\} - C, \tag{4.4}$$

which is a function of the local density of membrane particles

$$\rho_i = \sum_{j \neq i}^{N_{\mathrm{mb}}} f_{\mathrm{cut}}(r_{ij}/\sigma), \tag{4.5}$$

with $n = 12$, $s_{\mathrm{half}} = 1.8$, and $s_{\mathrm{cut}} = s_{\mathrm{half}} + 0.3$, where $f_{\mathrm{cut}}(s_{\mathrm{half}}) = 0.5$, which implies $A = \ln(2)(s_{\mathrm{cut}}/s_{\mathrm{half}})^n - 1$. The constant $C = 0.25 \ln[1 + \exp(4\rho^*)]$ is chosen so that $U_{\mathrm{att}} = 0$ at $\rho_i = 0$. Here we set $\rho^* = 6$ in order to simulate a 2D fluid membrane. For $\rho_i < \rho^*$, U_{att} acts as a pairwise potential with $U_{\mathrm{att}} = -2\sum_{j>i} f_{\mathrm{cut}}(r_{ij}/\sigma)$. For $\rho_i \gtrsim \rho^*$, this potential saturates to the constant $-C$. Thus, it is a pairwise potential with a cutoff at densities higher than ρ^*.

Our multi-body potential can enhance the molecular diffusion in the membrane and to obtain a wide range of stability of a fluid phase. Additionally, there is a second reason for employing a density cutoff, which can suppress 3D aggregates to 2D planar aggregates. For example, every particle has 12 nearest neighbors in a face-centered cubic crystal, while each particle has only six nearest neighbors in a two-dimensional hexagonal crystal. The density cutoff ρ^* retains the attraction for two-dimensional aggregates, but, in the third vertical direction, suppresses additional attractions for three-dimensional aggregates. If only pairwise attraction potentials are applied, the suppression of three-dimensional structures would require a much stronger curvature potential than for the multibody potential (4.4), which implies that the membrane would have a very large bending rigidity κ. It has been shown that the density-dependent potential allows a wide range of bending rigidities κ of the membrane [42, 117]. To choose the appropriate parameters of the potentials, information from the crystal structure of the ground state (at temperature $T = 0$) is helpful. The two-dimensional system can have two types of crystal structure, hexagonal and square lattices. The hexagonal crystal has six nearest neighbors and six next nearest neighbors at distances r_1 and $r_2 = \sqrt{3}r_1$, respectively. The square crystal has four nearest neighbors and four next-nearest neighbors with

$r_2 = 2r_1$. For example, the ground state for a square-well (or Heaviside step) potential

$$U_{\text{well}}(r_{ij}) = \begin{cases} \infty & (r_{ij} \leqslant \sigma) \\ -1 & (\sigma < r_{ij} \leqslant r_{\text{att}}) \\ 0 & (r_{\text{att}} < r_{ij}) \end{cases} \tag{4.6}$$

is a square lattice for $\sqrt{2} < r_{\text{att}}/\sigma < \sqrt{3}$ and hexagonal lattice otherwise. For our potential (4.4) with $\rho^* = \infty$ (pairwise interactions), the ground state is a square lattice for $1.578 < r_{\text{att}}/\sigma < 1.841$ and a hexagonal lattice otherwise. As ρ^* decreases, the region of fluid phase increases and particle diffusion in fluid membrane becomes faster. We use mainly the parameters $r_{\text{att}}/\sigma = 1.8$ and $\rho^* = 6$. While the robustness of our results to the choice of parameters also has been shown by using $r_{\text{att}}/\sigma = 1.9$ and $\rho^* = 8$ [42].

4.1.3 Aplanarity curvature potential

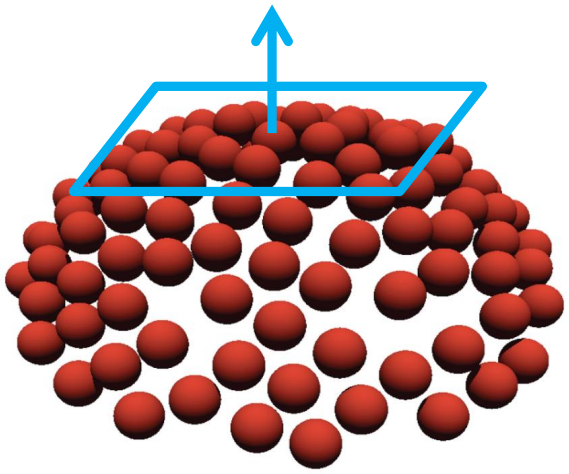

FIGURE 4.2: If a particle deviates from the local plane formed by the neighboring membrane particles, a force along the normal vector to this plane will be applied to this particle. The deviation degree reflects the magnitude of the applied force.

The curvature potential is expressed by the shape parameter called "aplanarity", which is defined by

$$\alpha_{\text{pl}} = \frac{9D_{\text{w}}}{T_{\text{w}}M_{\text{w}}}, \tag{4.7}$$

with the determinant $D_{\text{w}} = \lambda_1\lambda_2\lambda_3$, the trace $T_{\text{w}} = \lambda_1 + \lambda_2 + \lambda_3$, and the sum of the principal minors $M_{\text{w}} = \lambda_1\lambda_2 + \lambda_2\lambda_3 + \lambda_3\lambda_1$. The aplanarity α_{pl} scales the degree of deviation from the planar shape, and λ_1, λ_2, and λ_3 are three eigenvalues of the weighted gyration tensor

$$a_{\alpha\beta}(\mathbf{r}_i) = \sum_{j}^{N_{\text{mb}}} (\alpha_j - \alpha_G)(\beta_j - \beta_G) w_{\text{cv}}(r_{ij}), \tag{4.8}$$

where $\alpha, \beta \in \{x, y, z\}$, and the mass center of a local region of the membrane $\mathbf{r}_G = \sum_j \mathbf{r}_j w_{\rm cv}(r_{ij}) / \sum_j w_{\rm cv}(r_{ij})$. Without loss of generality, we suppose that $\lambda_1 \leqslant \lambda_2 \leqslant \lambda_3$. The minimum eigenvalue λ_1 represents a deviation from the local plane fit by the neighboring membrane particles (as shown in Fig. 4.2), and its corresponding eigenvector is collinear with the normal vector $\mathbf{n}$ of this plane. When the i-th membrane particle has two or fewer neighbor particles within the cutoff distance $r_{\rm cc}$, they could be localized on a certain plane, and therefore, $\alpha_{\rm pl} = 0$. A truncated Gaussian function is employed to calculate the weight of the gyration tensor

$$w_{\rm cv}(r_{ij}) = \begin{cases} \exp\left[\frac{(r_{ij}/r_{\rm ga})^2}{(r_{ij}/r_{\rm cc})^n - 1}\right] & (r_{ij} < r_{cc}) \\ 0 & (r_{ij} \geqslant r_{\rm cc}), \end{cases} \tag{4.9}$$

which is smoothly cut off at $r_{ij} = r_{\rm cc}$. Here we use the parameters $n = 12$, $r_{\rm ga} = 0.5 r_{\rm cc}$, and $r_{\rm cc} = 3\sigma$. The bending rigidity and the line tension of the membrane edges are linearly dependent on k_α and ε, respectively, for $k_\alpha \gtrsim 10$, so that they can be independently varied by changing k_α and ε, respectively.

In terms of the previous work[42], the aplanarity $\alpha_{\rm pl} \sim \lambda_1$ for the smallest eigenvalue $\lambda_1 \ll \lambda_2$,λ_3. In the polar coordinates, locally a patch of a cylindrical membrane can be expressed for small fluctuations in the Monge representation as

$$h = h_0 + \frac{1}{2} C_1 (s - s_0)^2 + \frac{1}{2} C_2 (z - z_0)^2, \tag{4.10}$$

where s and z coordinates are along the cross-section periphery and the symmetric axis of the cylinder, respectively. C_1 and C_2 are the corresponding principal curvatures of the cylindrical membrane patch. In the case of cylindrical membrane, h_0 is the average radius along the normal vector of the local membrane patch. By averaging over the local neighborhood with a weight function $w(r)$ where $r^2 = s^2 + z^2$, we have

$$\lambda_1 = \langle h^2 \rangle - \langle h \rangle^2 = \langle (C_1^2 + C_2^2) \rangle \langle (r^2 - \langle r^2 \rangle)^2 \rangle. \tag{4.11}$$

Since $\langle C_1^2 + C_2^2 \rangle = \langle (C_1 + C_2)^2 \rangle - 2\langle C_1 C_2 \rangle$ and $\langle C_2 \rangle = 0$ for the cylindrical membrane, we easily know

$$k_\alpha \alpha_{pl} \sim k_\alpha \lambda_1 \sim k_\alpha \langle (C_1 + C_2)^2 \rangle. \tag{4.12}$$

Thus, a linear relation between the bending energy in Helfrich's macroscopic model and our mesoscopic parameter is obtained as $\kappa \propto k_\alpha$, which is numerically confirmed in the previous work [42, 117]. The membrane has almost zero spontaneous curvature without polymers.

4.1.4 Chemical affinity potential between different particles

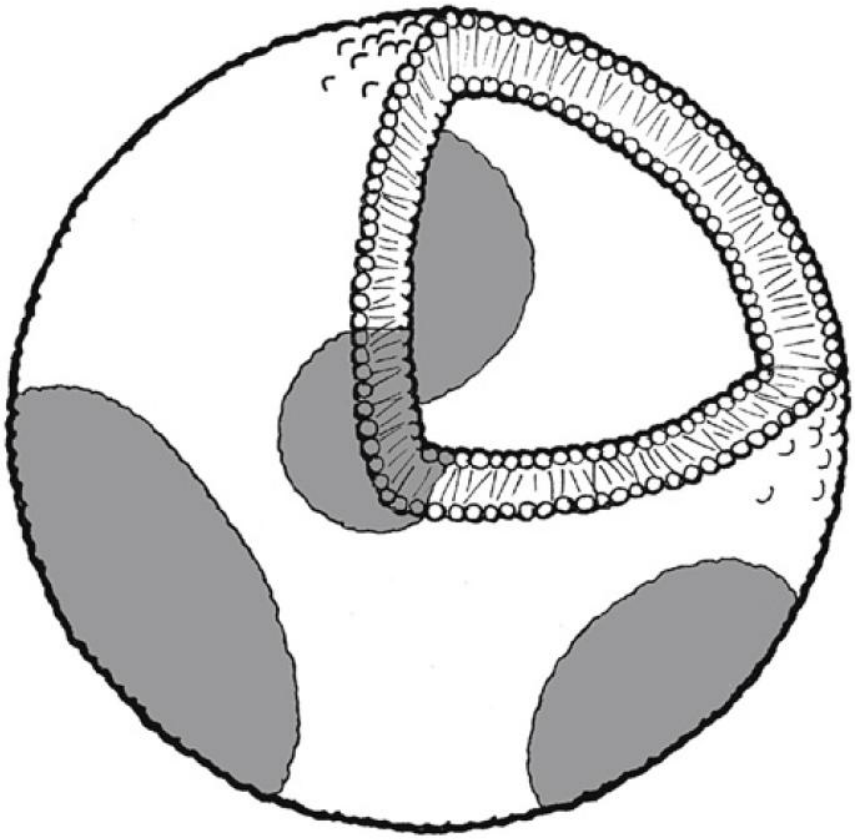

FIGURE 4.3: A biomimetic vesicle can be considered as a thin spherical shell composed of a lipid bilayer, bounded by water on the inside and outside. Coexisting lipid phase domains occur on the bilayer of the typical ternary vesicle. Reprinted with permission from Ref. [8]

For artificial multi-component membrane systems, a biomimetic vesicle can be considered as a thin spherical shell composed of a lipid bilayer, bounded by water on the inside and outside. When the composition of the bilayer is a ternary mixture composed of typically a saturated lipid, an unsaturated lipid, and cholesterol, coexisting liquid phases at micron scale can occur in the bilayer. Biophysicists assume that when the phase separation occurs on the bilayer, the saturated lipid composition has the same distribution on both inner layer and outer layer, which is shown in Fig. 4.3. Based on this starting point, we can conveniently ignore the little difference of lipid composition between the inner and outer leaflets of the bilayer, and for the simplicity assume that the same kind of lipids have the same motion tendency during the process of phase separation. Thus, we can further extend our coarse-grained meshless model to study multi-component membrane systems.

Two types of membrane particles, A and B, are considered in Chapter 7. The number of these particles are N_{A} and N_{B}, respectively. To investigate phase separation, we apply a repulsive term U_{AB} in Eq. (4.1) to reduce the chemical affinity between different types of membrane particles [118]. The potential U_{AB} is a monotonic decreasing function: $U_{\mathrm{AB}} = \varepsilon_{\mathrm{AB}} \sum_{i\in A, j\in B} A_1 f_{\mathrm{cut}}(r_{i,j})$ with $n = 1$, $A_1 = 1$ and $r_{\mathrm{cut}} = 2.1\sigma$, and $A_1 = \exp[\sigma/(r_{\mathrm{cut}} - \sigma)]$ to set $U_{\mathrm{AB}}(\sigma) = 1$.

4.2 Model biomembranes with linear flexible polymers

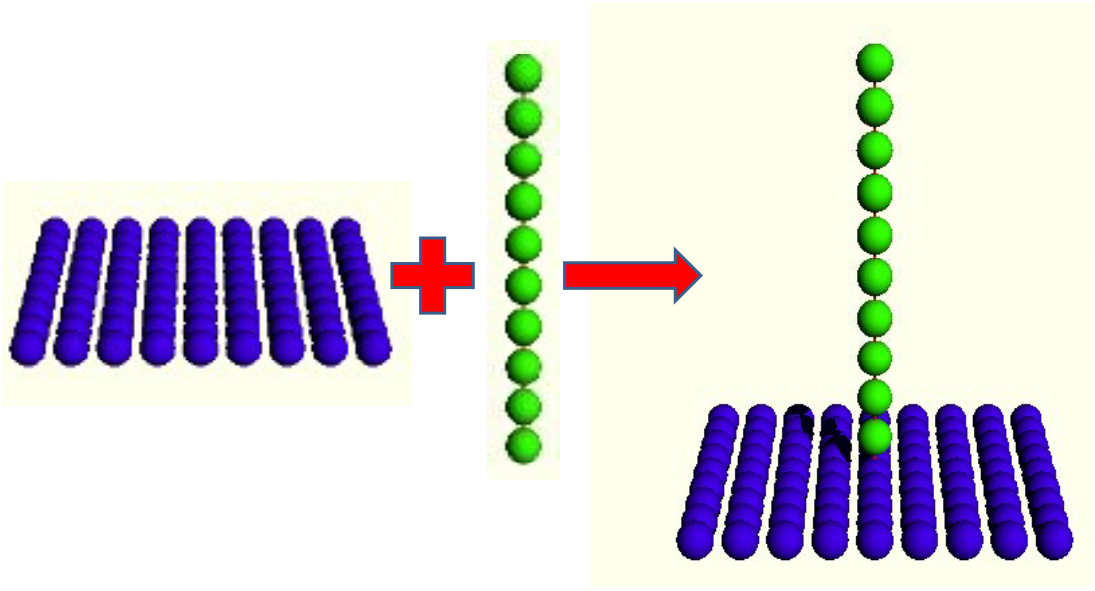

FIGURE 4.4: A coarse-grained lipid membrane anchored with a coarse-grained polymer chain to form a anchored biomembrane system. The blue particle represent membrane particles. A single polymer chain is composed of ten (green) particles which are freely linked as an excluded-volume chain. Reprinted with permission from Ref. [46].

We consider flexible linear polymer chains anchored on the membrane. Polymer particles are connected by a harmonic spring potential,

$$U_{\mathrm{p}} = \frac{k_{\mathrm{bond}}}{2} \sum_{\mathrm{chain}} (r_{i,i+1} - b)^2, \tag{4.13}$$

where k_{bond} is the spring constant for the harmonic potential and b is the Kuhn length of the polymer chain. The summation is taken only between neighboring particles along polymer chains and between the end polymer particles and anchored membrane particles (a total of N_{p} springs in each chain). We choose $b = 1.2\sigma$ here such that a polymer chain stays in the force-free state for $r_{i,i+1} = b$.

We use $N_{\mathrm{p}} = 10$, $\varepsilon = 4$, $k_\alpha = 10$, and $k_{\mathrm{har}} = 10$ through this work. In the absence of anchored polymer chains, the tensinless membranes have the bending rigidity $\kappa_{\mathrm{cv}}/k_{\mathrm{B}}T =$

21 ± 0.5, the line tension of open edges $\Gamma_{\mathrm{ed}}\sigma/k_{\mathrm{B}}T = 4.5$ and the area $a_0 = 1.44\sigma^2$ per membrane particle [**?**]. For single-component membranes, the number of membrane particles are fixed as $N_{\mathrm{mb}} = 1200$ and the number fraction $\phi = N_{\mathrm{chain}}/N_{\mathrm{mb}}$ of polymer-anchored membrane particles is varied.

In cell membranes, there are more types of unsaturated lipids having more flexibility to tune lipid compositions so as to approach many possible critical points [8]. Thus, for a two-component membrane patch the number of the type A membrane particles, which can combine polymer chains, is fixed as $N_{\mathrm{A}} = 400$ as the minority saturated lipids, and the number of the type B particles is chosen as $N_{\mathrm{B}} = 400$ and 2100 as unsaturated lipids with more flexibility for a striped domain and circular domain, respectively. The polymer chains are anchored to the type A particles and the polymer fraction $\phi = N_{\mathrm{chain}}/N_{\mathrm{A}}$ is varied. To confirm the membranes is in thermal equilibrium, we compare the results between two initial states, stretching or shrinking, and check no hysteresis is obtained. We slowly stretch and shrink in axial direction for cylinder or for striped membranes with a speed less than $L_z/dt = 10^{-6}\sigma/\tau$ and then equilibrate them for $t/\tau = 6\times10^4$ before the measurements. For the simulations of circular domains, the membranes equilibriated for the duration of $6\times10^4\tau$ after step-wise changes of ϕ or $\varepsilon_{\mathrm{AB}}$. The error bars are calculated from six independent runs.

4.3 Our simulation method

4.3.1 Leapfrog integration

Leapfrog integration is an integration scheme that does not suffer from the gradually divergent behavior. While it is also a second-order accurate scheme like the Verlet method, and therefore the error at each step is similar, on average the errors in this new scheme tend to cancel out instead of add coherently. Hence this new scheme, called leapfrog integration, is a better choice to evolve systems over many dynamical times.

The reason for this is that leapfrog integration has the property of being "symplectic", which is a property whose definition we will not discuss in detail, but one can broadly think of it as a scheme that is time-reversible; i.e. it is possible to use the same set of equations with time evolved in reverse to recover the initial conditions from the final state. For symplectic integration schemes, higher order errors tend to cancel out on average rather than add coherently, and hence such schemes maintain approximately the proper orbit forever.

In the leapfrog scheme, the positions and velocities are "leapfrogged" over each other, with one being advanced between the full timesteps (i.e. $0 \to 1 \to 2 \to ...$) and the other one being advanced between "halfsteps" (i.e. $\frac{1}{2} \to \frac{3}{2} \to \frac{5}{2} \to ...$). A full timestep thus progresses as follows:

$$x_{i+\frac{1}{2}} = x_i + \frac{1}{2} v_i \Delta t \tag{4.14}$$

$$v_{i+1} = v_i + \frac{1}{2} a_{i+\frac{1}{2}} \Delta t \tag{4.15}$$

$$x_{i+1} = x_{i+\frac{1}{2}} + \frac{1}{2} v_{i+1} \Delta t \tag{4.16}$$

Ones easily that by substituting the first of the three equations into the last, one obtains the formula for x_{i+1} in the Verlet method, and by substituting the last equation into the second, one obtains v_{i+1} in the Verlet method with the exception that the acceleration at the halfstep $a_{i+\frac{1}{2}}$ is used in place of the average acceleration across the step $\frac{1}{2}(a_i + a_{i+1})$. It is straightforward to show that this maintains the same order of accuracy as the Verlet equations.

4.3.2 NVT ensemble

The constant-temperature, constant-volume ensemble (NVT) ensemble (constant number of particles N, volume V, and temperature T) is used with periodic boundary conditions in a simulation box of dimensions $L_x \times L_y \times L_z$. The NVT is also referred to as the canonical ensemble. The ensemble is obtained by controlling the temperature through Langevin thermostat. The volume is kept constant throughout the run. This is the appropriate choice when conformational searches of molecules are carried out in vacuum without periodic boundary conditions. Without periodic boundary conditions, volume, pressure, and density cannot be defined. Constant-pressure dynamics cannot be carried out. Even if periodic boundary conditions are used, if pressure is not a significant factor, the constant-temperature constant-volume ensemble provides the advantage of less perturbation of the trajectory, due to the absence of coupling to a pressure bath.

4.3.3 Brownian dynamics simulation

The Brownian dynamics simulation technique is a mesoscopic method in which explicit solvent molecules are replaced by a stochastic force. The technique takes advantage of the fact that there is a large separation in time scales between the rapid motion of solvent molecules and the more sluggish motion of polymers, lipids, or colloids. The ability to coarse-grain out these fast modes of the solvent allows one to simulate much larger time scales than in a molecular dynamics simulation. At the core of a Brownian dynamics simulation is a stochastic differential equation, called Langevin equation, which is integrated forward in time to create trajectories of molecules. Time enters naturally into the scheme allowing for the study of the temporal evolution and dynamics of complex fluids (e.g. polymers, vesicle self-assembly, large proteins, DNA molecules and colloidal solutions). The Langevin equation generates classical Brownian dynamics which describes the motion of a particle under the influence of random collisions with the surrounding solvent. Brownian dynamics simulations are particularly well suited to studying the structure and rheology of complex fluids in hydrodynamic flows and other nonequilibrium situations.

In Brownian dynamics, atoms in the system are assumed to be embedded in a sea of fictional particles of smaller size, like a buffer region. Thus, in this case the dynamics of particles is described by Langevin equations of motion instead of the Newtons equations. In the Langevin equation, two additional force terms have been added to Newton's second law to approximate the effects of neglected degrees of freedom. One term represents a frictional force, which describes the drag on the particle due to the solvent, the other one represents a random or stochastic force due to thermal fluctuations of the solvent. For example, the effects of solvent molecules is not explicitly present in the system being simulated would be approximated in terms of a frictional drag on the solute as well as random kicks associated with the thermal motions of the solvent molecules. Since friction opposes motion, the first additional force is proportional to the particle's velocity and oppositely directed. For planar membranes, the projected area $L_x \times L_y$ is set for the tensionless state. The dynamics of both membrane and anchored flexible polymers are calculated by using underdamped Langevin dynamics. The Langevin thermostat is used to maintain constant temperature in the course of the simulation. The motions of membrane and polymer particles are governed by

$$m\frac{d^2\mathbf{r}_i}{dt^2} = -\frac{\partial U_{\text{tot}}}{\partial \mathbf{r}_i} - \zeta\frac{d\mathbf{r}_i}{dt} + \mathbf{g}_i(t) \tag{4.17}$$

where m is the mass of a particle (membrane or polymer particle) and ζ is the friction constant. $\mathbf{g}_i(t)$ is a Gaussian white noise, which obeys the fluctuation-dissipation

theorem:

$$\langle g_{i,\alpha}(t)\rangle = 0 \tag{4.18}$$

$$\langle g_{i,\alpha}(t)g_{j,\beta}(t')\rangle = 2k_{\mathrm{B}}T\zeta\delta_{ij}\delta_{\alpha\beta}\delta(t-t') \tag{4.19}$$

where $\alpha, \beta \in \{x, y, z\}$, $k_{\mathrm{B}}T$ is the thermal energy, $\langle \dots \rangle$ denotes statistical average. The temperature of the system being simulated is maintained via this relationship between $\mathbf{g}_i(t)$ and ζ. We employ the time unit $\tau = \zeta\sigma^2/k_{\mathrm{B}}T$ with $m = \zeta\tau$. The Langevin equations are integrated by the leapfrog integration [112] with a time step of $\Delta t = 0.005\tau$. Because the discretization of $\delta(t-t')$ is $1/\Delta t$, Eq. (4.19) is rewritten as

$$\begin{aligned}\langle g_{i,\alpha}(t)g_{j,\beta}(t')\rangle &= \frac{2k_{\mathrm{B}}T\zeta\delta_{ij}\delta_{\alpha\beta}}{\Delta t} \\ &= \langle\frac{\widetilde{g}_{i,\alpha}(t)\widetilde{g}_{j,\beta}(t')}{\Delta t}\rangle\end{aligned} \tag{4.20}$$

By combining the leapfrog integration, we can discrete the Langevin motion equations as

$$m\frac{\Delta\mathbf{v}_i(t)}{\Delta t} = -\zeta\mathbf{v}_i(t+\Delta t/2) + \mathbf{f}_i(t) + \frac{\widetilde{\mathbf{g}}_i(t)}{\sqrt{\Delta t}} \tag{4.21}$$

$$\mathbf{v}_i(t+\Delta t/2) = \frac{\mathbf{v}_i(t)+\mathbf{v}_i(t+\Delta t)}{2} \tag{4.22}$$

$$\Delta\mathbf{v}_i(t) = \mathbf{v}_i(t+\Delta t) - \mathbf{v}_i(t) \tag{4.23}$$

where $\mathbf{f}_i(t) = -\partial U_{\mathrm{tot}}/\partial\mathbf{r}_i$. From the discretization Eqs. (4.21), (4.22), and (4.23), we can easily obtain an applicable discreted algorithm as:

$$\mathbf{v}_i(t+\Delta t) = \mathbf{v}_i(t)\frac{1-\zeta\Delta t/2m}{1+\zeta\Delta t/2m} + \frac{\mathbf{f}_i(t)+\widetilde{\mathbf{g}}_i(t)\sqrt{\Delta t}/m}{1+\zeta\Delta t/2m} \tag{4.24}$$

4.4 Radial distribution function of meshless membrane systems

The radial distribution function (RDF) is an important structural characteristic and also an example of a pair correlation function, which describes how, on average, the particles in a system are radially packed around each other. This proves to be a particularly effective way of describing the average structure of disordered molecular systems such as liquids. Also in systems like liquids, such as fluid membrane systems, where there is continual movement of the particles and a single snapshot of the system shows only the instantaneous disorder, it is extremely useful to be able to deal with the average structure.

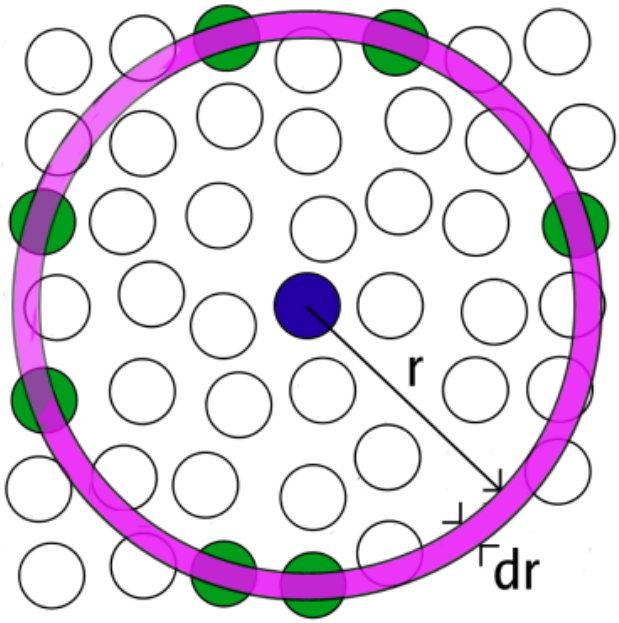

FIGURE 4.5: A schematic picture of the space discretization for the evaluation of the radial distribution function (from the ISAACS website of Central Michigan University).

The RDF is useful in other ways. For example, it is something that can be deduced experimentally from x-ray or neutron diffraction studies, thus providing a direct comparison between experiment and simulation. It can also be used in conjunction with the interparticle pair potential function to calculate the internal energy of the system, usually quite accurately.

To construct an RDF is simple. Because our potentials for meshless membrane model is applied to form a quasi-2D membrane, we will study RDF in our model in the 2D case. For the 2D membrane case, choose a particle in the system and draw around it a series of concentric circles, set at a small fixed distance dr apart (see Fig. 4.5). At regular intervals a snapshot of the system is taken and the number of particles found in each 2D circular shell is counted and stored. At the end of the simulation, the average number of particles in each shell is calculated. This is then divided by the area of each shell and the average density of particles in the system. The result is the RDF. Mathematically the 2D formula is:

$$g(r) = \frac{n(r)}{(N/A_{\mathrm{p}})2rdr} = \frac{n(r)}{\rho 2rdr} \tag{4.25}$$

where $g(r)$ is the RDF, $n(r)$ is the mean number of particles in a 2D circular shell of width dr at distance r, N is the total particle number, A_{p} is the 2D membrane project area, ρ is the mean particle density. The method need not be restricted to one particle. All the particles in the system can be treated in this method, leading to an improved

determination of the RDF as an ensemble average of many particles.

The RDF is usually plotted as a function of the interpaticle separation r. The RDF picture (below) shows a number of important characteristics. Firstly, at short separations ($\leq r$) the RDF is zero. This indicates the effective width of the particles, since they cannot approach any more closely. Secondly, a number of obvious peaks appear, which indicate that the particles pack around each other in 'shells' of neighbours. The occurrence of peaks at long range indicates a high degree of ordering. Usually, at high temperature the peaks are broad, indicating thermal motion, while at low temperature they are sharp. They are particularly sharp in crystalline materials, where particles are strongly confined in their positions. At very long range every RDF tends to a value of 1, which happens because the RDF describes the average density at this range. Here we show a RDF plot in our meshless membrane model for a patch of tensionless membrane in Fig. 4.6. From it, we see that the effects of our meshless potentials can well be normalized. Fig. 4.6 also describes how density of membrane particles varies as a function of distance from a reference particle in our meshless model.

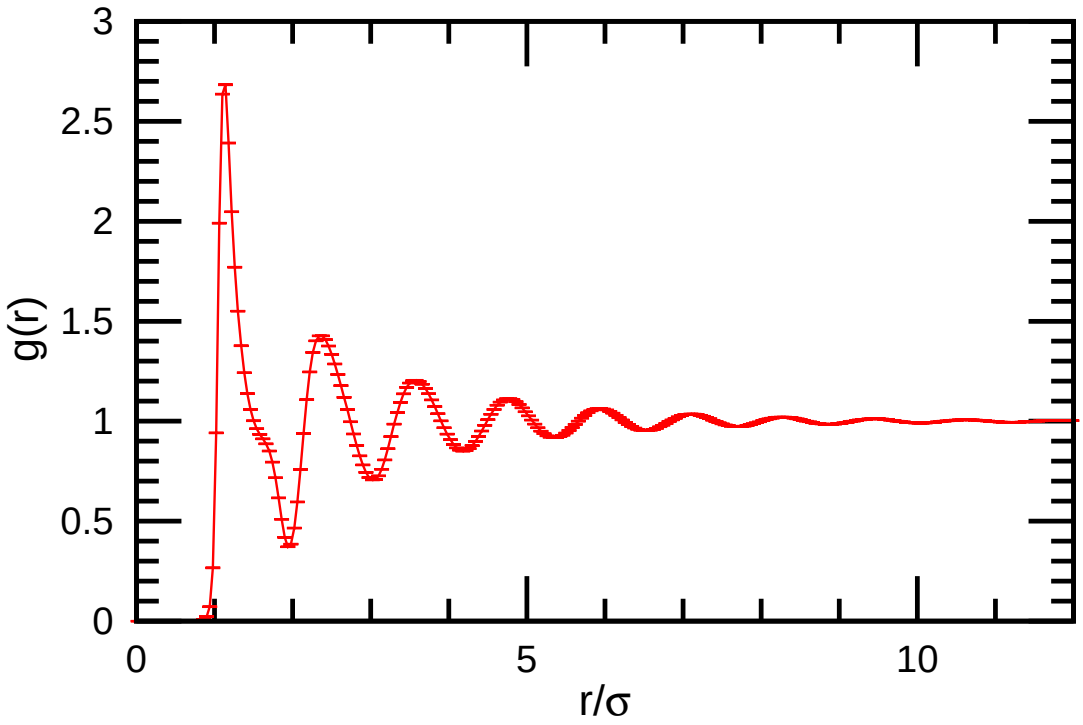

FIGURE 4.6: A plot of radial distribution function for a patch of tensionless membranes is shown.

Chapter 5

Bending Rigidity and Spontaneous Curvature of Biomembranes

In the study of membranes, the bending rigidity κ is widely considered as a most important quantity for characterizing the flexibility of membranes at a mesoscopic level. There are also some other quantities, such as the Gaussian bending rigidity $\bar{\kappa}$ [119–121], important for membrane fusion [122], and the area compressibility modulus K_{A} [123]. However, the centrality of the bending rigidity is irreplaceable, because of the fact that it is the ratio $\bar{\kappa}/\kappa$ that is usually reported rather than $\bar{\kappa}$ alone, and the compressibility modulus K_A is also often measured based on κ [71]. Also, there are relatively few measurements of $\bar{\kappa}$ and κ compared with the ones of κ. In this thesis, let's only focus on κ among them.

For an asymmetric membrane, a second central quantity is the spontaneous curvature C_0, which can be used to phenomenologically determine the local asymmetric degree of membrane patch. When the components of two leaflets of bilayers are exactly the same, the spontaneous curvature is diminished. If there is some reason to cause the difference between two leaflets, then membrane will have a preference to curve to one side than the other side. The existence of the asymmetry of bilayers is very crucial and necessary to the deformation of biomimetic vesicles and some kinds of cells, such as red blood cells.

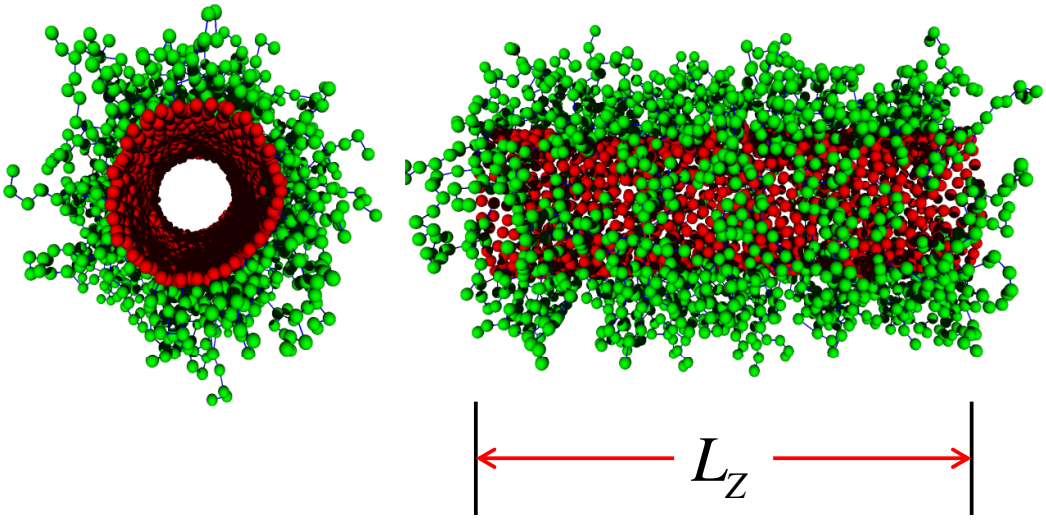

FIGURE 5.1: A snapshot of front and side views of a cylindrical membrane with anchored excluded-volume polymer chains only at the outer surface of the membrane at the polymer density $\phi = 0.167$ and the cylinder axial length $L_z = 45.3\sigma$. The red and green particles represent membrane and polymer particles, respectively. Reproduced from Ref. [47] with permission of The Royal Society of Chemistry.

5.1 Axial force method

A cylindrical membrane with polymer chains anchored at the outer surface of the membrane is used to estimate the polymer-induced spontaneous curvature and bending rigidity (see Fig. 5.1). For a cylindrical membrane with a radius R and a length L_z, Helfrich curvature elastic free energy is given by

$$\begin{aligned} F_{\mathrm{He}} &= \int \left[\frac{\kappa}{2}(C_1 + C_2 - C_0)^2 + \bar{\kappa} C_1 C_2\right] dA \\ &= 2\pi R L_z \left[\frac{\kappa}{2}\left(\frac{1}{R} - C_0\right)^2\right], \end{aligned} \tag{5.1}$$

where C_1 and C_2 are the principal curvatures at each position on the membrane surface, and the membrane area $A = 2\pi R L_z$. The coefficients κ and $\bar{\kappa}$ are the bending rigidity and saddle-splay modulus, respectively, and C_0 is the spontaneous curvature. In the absence of the anchored polymer (we call it a pure membrane hereafter), the membrane has zero spontaneous curvature, $C_0 = 0$. Note that compared with the first term of Eq. (3.4) we find $1/R = 2H$ for the cylindrical case, so $C_0 = 2c_0$.

We also have known that the membrane, with anchored polymers, has the area compression energy $F_{\rm ar}(A)$ that can be expressed as:

$$F_{\rm ar}(A) = \frac{K_A(A-A_0)^2}{A_0}. \tag{5.2}$$

where A_0 is the area of the tensionless membrane, and generally $A - A_0 \ll A_0$. The radius R is determined by the total curvature free-energy minimization $\partial F_{\rm cv}/\partial R|_{L_z} = 0$ for $F_{\rm cv} = F_{\rm He} + F_{\rm ar}(A)$, so that we obtain the relation:

$$\frac{K_A(A-A_0)}{A_0} = \frac{\kappa}{R}\Big(\frac{1}{R} - C_0\Big) - \frac{\kappa}{2}\Big(\frac{1}{R} - C_0\Big)^2. \tag{5.3}$$

Since the total curvature free energy increases with increasing L_z, along the cylindrical axis a general shrinking force, including the contribution of area compressibility, is generated as

$$\begin{aligned} f_z &= \pi\kappa R\Big(\frac{1}{R} - C_0\Big)^2 + 2\pi R\frac{K_A(A-A_0)}{A_0} \\ &= 2\pi\kappa\Big(\frac{1}{R} - C_0\Big). \end{aligned} \tag{5.4}$$

The axial force $f_z = -P_{zz}L_z$ can be calculated from the pressure tensors:

$$P_{\alpha\alpha} = \frac{1}{V}\left\langle Nk_{\rm B}T - \sum_i \alpha_i \frac{\partial U}{\partial \alpha_i}\right\rangle, \tag{5.5}$$

for $\alpha \in \{x, y, z\}$, where the summation is taken over all of membrane and polymer particles, $\langle \dots \rangle$ denotes statistical average. When the potential interaction crosses the periodic boundary, the periodic image $\alpha_i + nL_\alpha$ is employed for $P_{\alpha\alpha}$ calculation, whose specific algorithm in MD simulation is illustrated in the Appendix B in detail.

Then we can plot the pictures of the axial force f_z dependence on the radius $1/R$ of the cylindrical membranes at different anchored polymer densities for ideal chains and excluded-volume chains (see Fig. 5.2), respectively. The force f_z increases linearly with $1/R$ [46]. Thus, C_0 and κ of the anchored membranes can be estimated from a linear fitting method to Eq. (5.4). For both anchored ideal chains and excluded-volume chains, the obtained values of C_0 and κ are shown in Fig. 5.5. For the pure membranes, the value of κ agrees very well with those estimated from the height fluctuations of planar membranes [117] and membrane bucking [124]. The estimated value of C_0 for the pure membrane deviates slightly from the exact value, zero. This small deviation would be caused by a higher-order term of the curvature energy [125] or finite size effects as discussed in Ref. [117].

We measured the axial force with several cylindrical membranes with different stretched (or shrinked) axial lengths, as shown in Fig. 5.2, where the overlapping range of stretched data and shrinked data is less than the error bar. It means that our simulation is very stable. The solid lines are obtained by linear least-squares fits for the last seven points. It can avoid the finite size effect for the cylindrical membrane with a short axial length.

5.2 Anchored linear polymers simulation

In this section, we introduce some fundamental measurements on quantities of large densities of anchored short ideal and excluded volume polymers. As mentioned in Chapter 3, the end-to-end distance is a very important quantity to estimate the effective mechanical properties of biomembranes. For a flexible free polymer chain, it satisfies the theoretical predictions. If it is anchored on a membrane surface, due to the constraint of polymer configuration space, it has to only move oppose to the membrane substrate, and lose a part of configuration entropy. Thus, it is expected that the end-to-end distance of anchored polymers will increase a little bit more than the one of flexible polymers in free space. Our simulation results make sure this conclusion, as shown in Fig. 5.3)

From the simulation, we find that there is no difference of the end-to-end distance of ideal chains with different anchored-polymer densities. However, the end-to-end distance of excluded-volume chains increase with higher anchored-polymer densities, since excluded-volume chains can form brush region due to the strong steric repulsion. Although there are no direct theoretical predictions on the end-to-end distance of anchored polymers to compare with our measurements, theoretical heights of excluded-volume chains, depending on the anchored-polymer densities, in the polymer brush region are often used for calculation.

To make sure that our simulation period is sufficiently long, we track the time-dependent end-to-end distances of any two chains of anchored ideal chains and excluded-volume chains, whose traces are similar to the cases of free chains, which is shown in Fig. 5.4.

5.3 Collective effects of anchored polymer layer

The force f_z increases linearly with $1/R$ [46]. Thus, C_0 and κ of the anchored membranes can be estimated from a linear fitting method to Eq. (5.4). For both anchored ideal chains and excluded-volume chains, the obtained values of C_0 and κ are shown in Fig. 5.5. For the pure membranes, the value for κ agrees very well with those estimated from height fluctuations of planar membranes [117] and membrane bucking [124]. The estimated

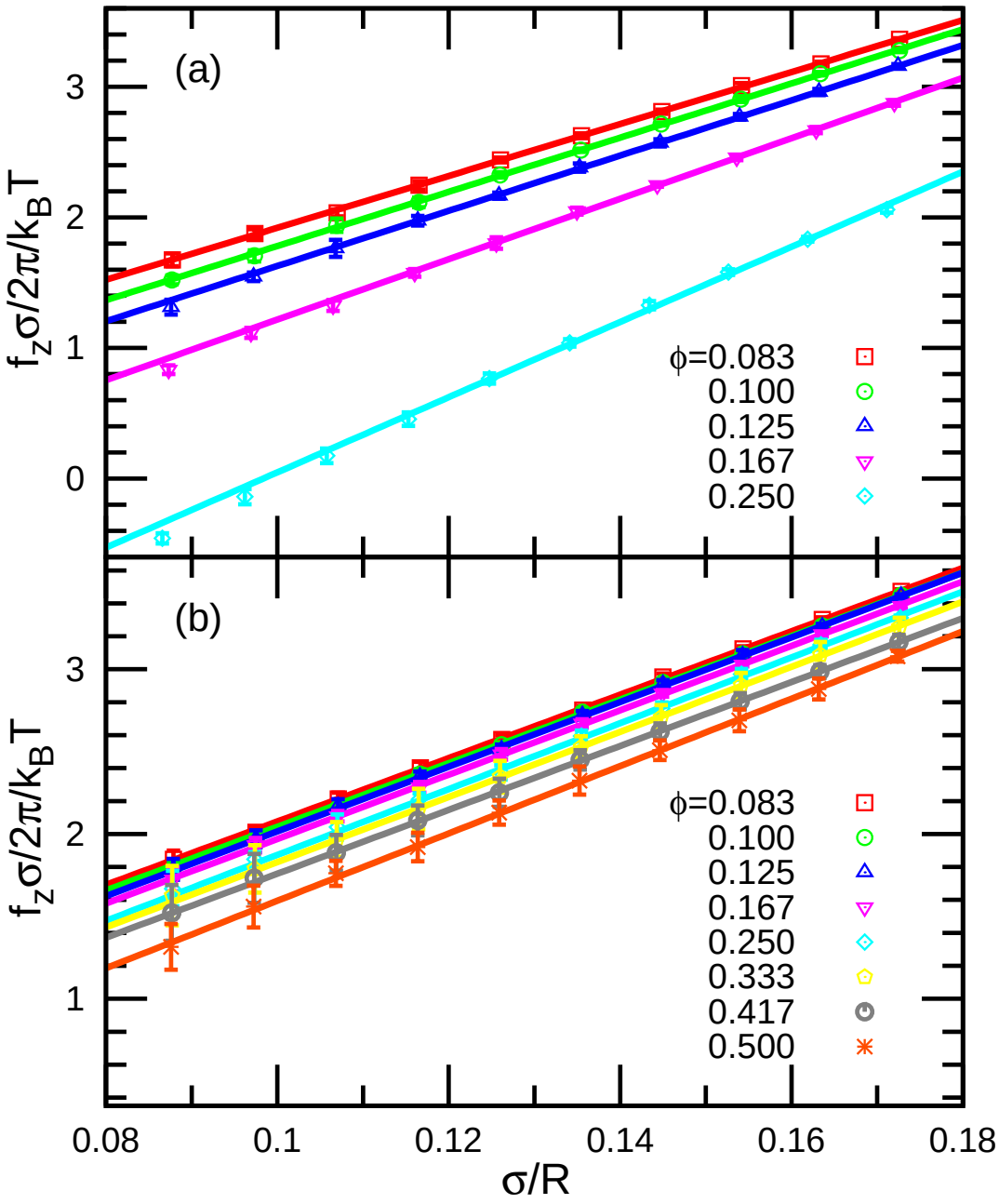

FIGURE 5.2: (a) For the excluded volume chains, the axial force f_z dependence on the radius R of the cylindrical membranes at $\phi = 0.083$, 0.100, 0.125, 0.167, and 0.250. The solid lines are obtained by linear least-squares fits for the last seven points. (b) For the ideal chains, the axial force f_z dependence on the radius R of the cylindrical membranes at $\phi = 0.083$, 0.100, 0.125, 0.167, 0.250, 0.333, 0.417, and 0.500. The solid lines are obtained by linear least-squares fits for the last seven points.

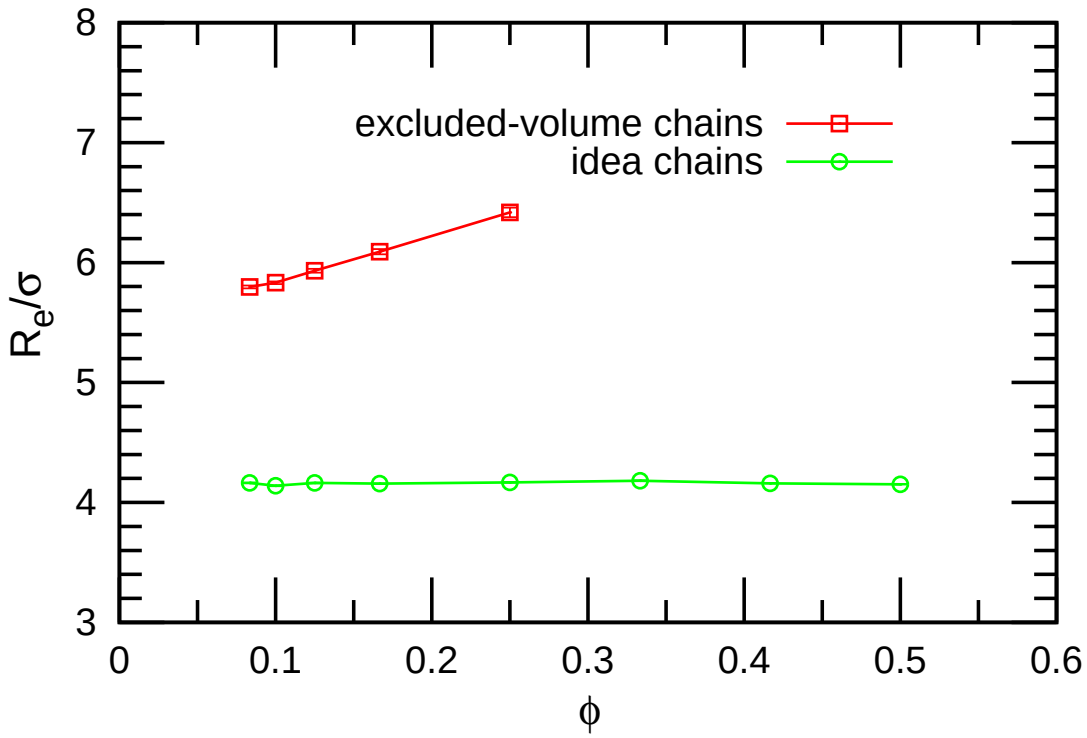

FIGURE 5.3: Simulation results of the end-to-end distances dependent on anchored polymer densities for ideal chains and excluded-volume chains.

value of C_0 for the pure membrane has small deviation from the exact value, zero. This small deviation would be caused by higher order term of the curvature energy or finite size effects as discussed in Ref. [117]. From Fig. 5.5 we found that the accurate C_0 and κ can be obtained compared with the pure membrane case. It means that the polymer-anchored membranes (specially the membranes with anchored excluded-volume chains due to the additional steric repulsion) have the more stable configuration because some big fluctuations (a kind of membrane entropy) of pure membranes are suppressed by the entropy of anchored polymers [46]. Thus, the estimated κ will not decay as shown for the pure membranes in Ref. [117].

The anchored polymer generates a positive (opposite to the anchored surface) spontaneous curvature, and enhances the bending rigidity κ. Both quantities increase with increasing polymer chain density, and for the excluded-volume chains, these increases are enhanced by the repulsive interactions between the neighboring chains.

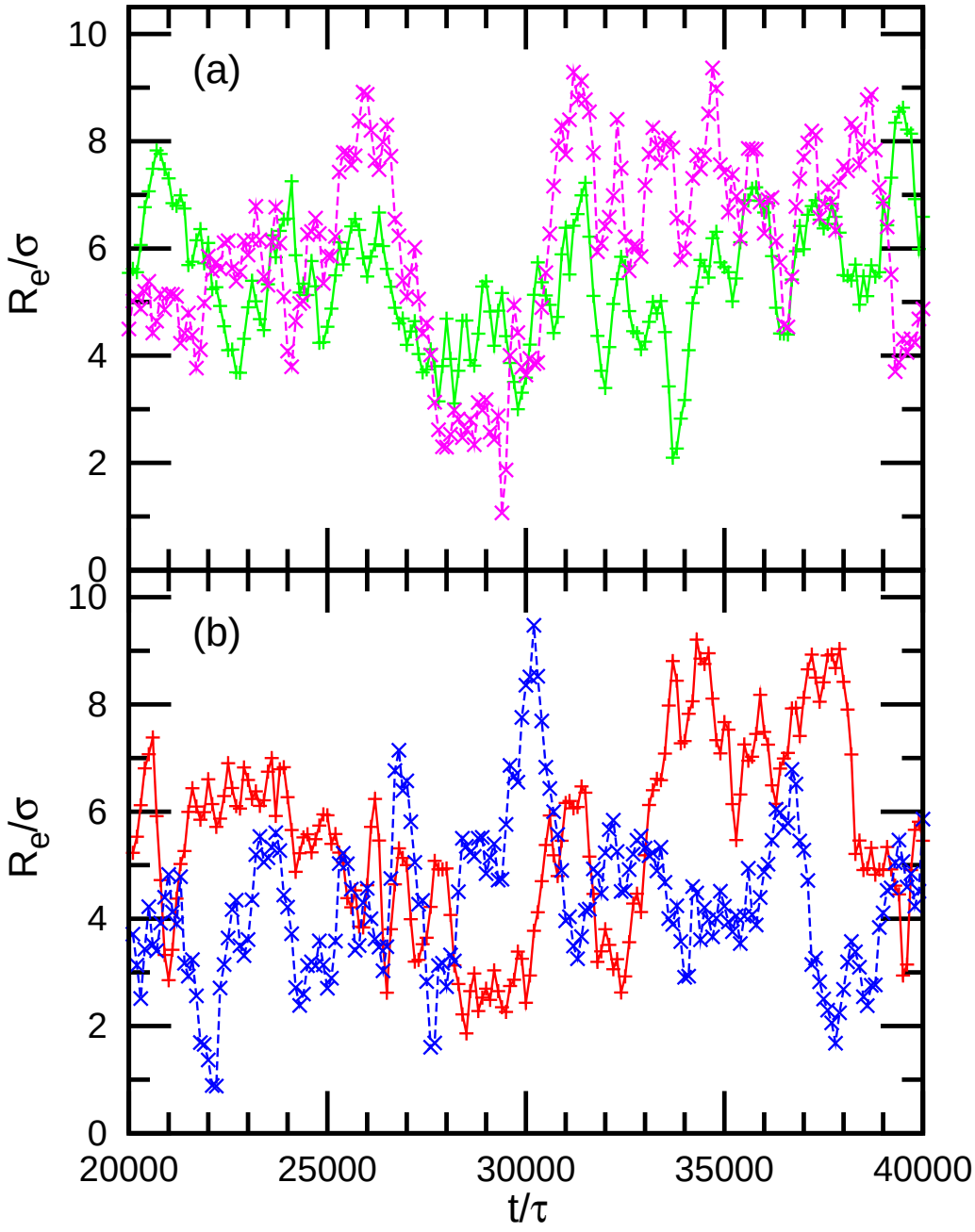

FIGURE 5.4: The time-dependent end-to-end distance of two anchored excluded-volume chains is shown in (*a*). The time-dependent end-to-end distance of two anchored idea chains is shown in (*b*).

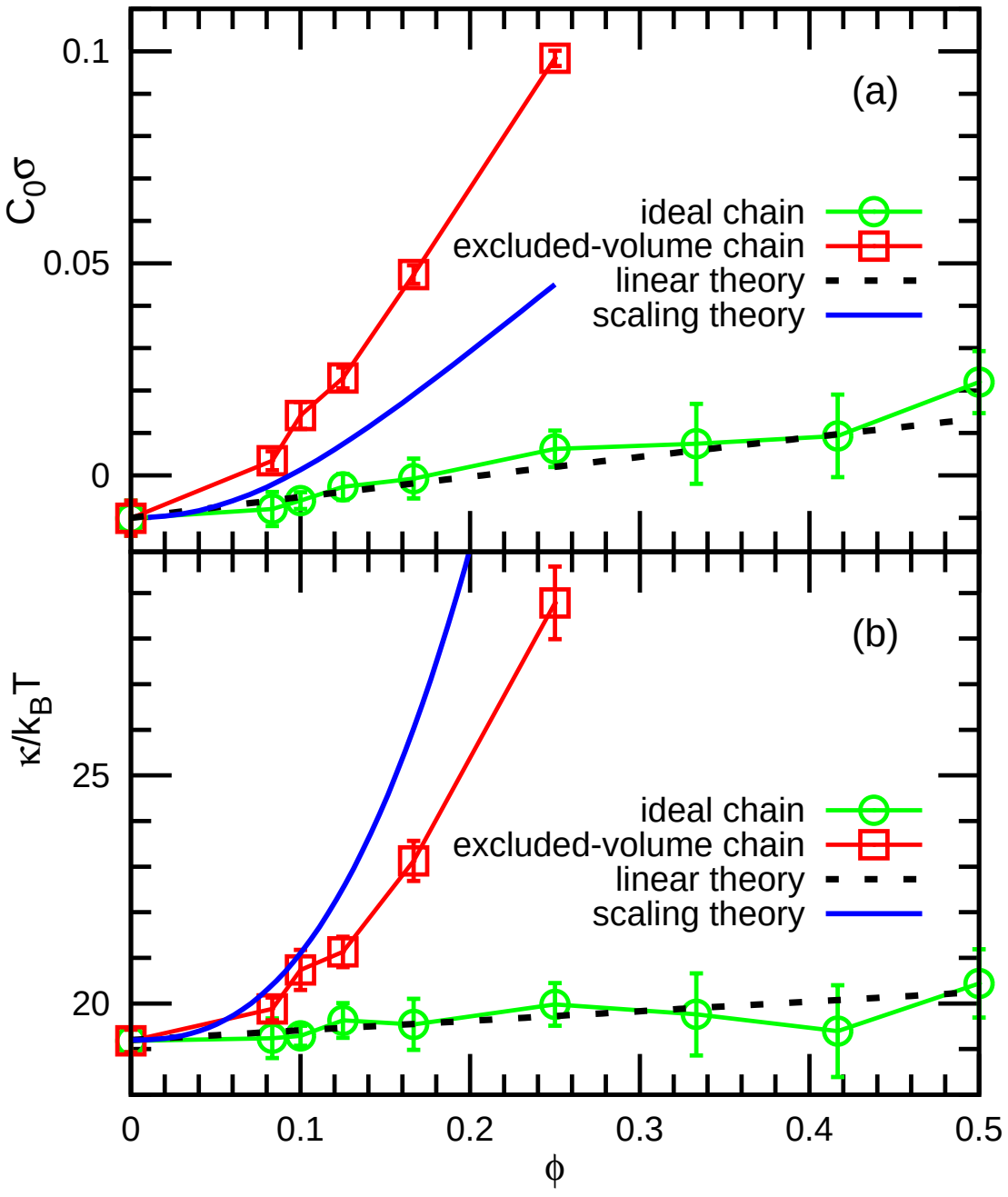

FIGURE 5.5: Polymer density ϕ dependence of (a) the spontaneous curvature C_0 and (b) bending rigidity κ of the membranes with anchored ideal chains and excluded-volume chains. The dashed lines in (a) and (b) represent the prediction of the linear theory (Eqs. (5.6) and (5.7)) for the ideal chains. The solid lines in (a) and (b) represent the prediction of the scaling theory (Eqs. (5.9) and (5.10)) in the brush region.
Reproduced from Ref. [47] with permission of The Royal Society of Chemistry.

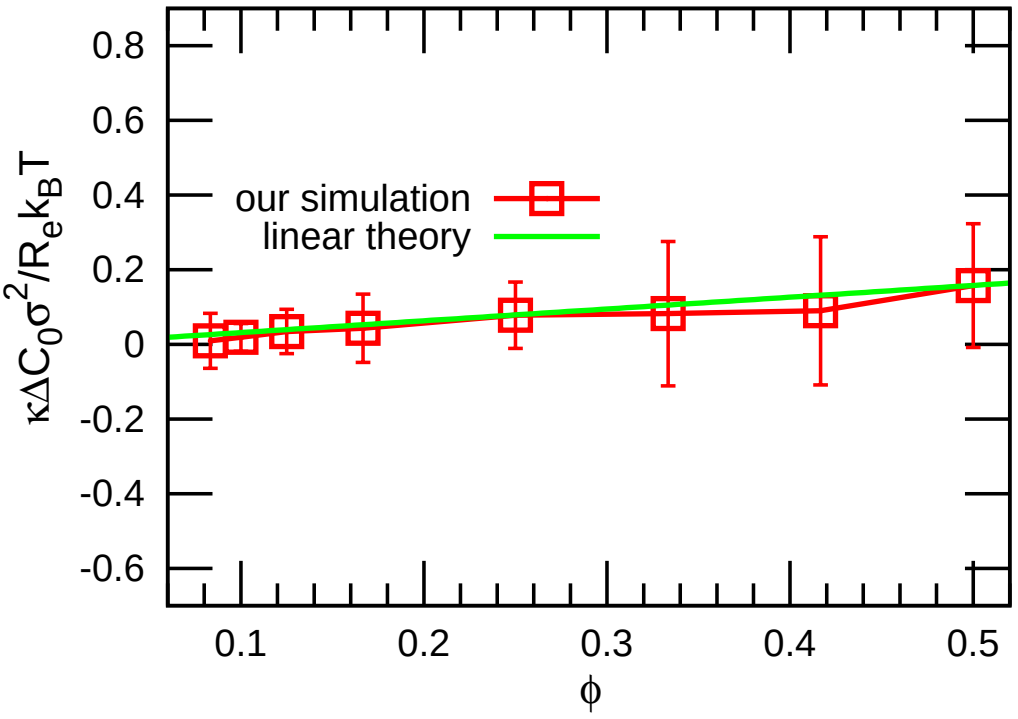

FIGURE 5.6: Comparison of a compound quantity $\kappa C_0/R_e$ theoretically defined by a linear theory in Ref. [26] and its estimation in our simulations for the ideal chains. The green lines represent the linear theory (Eq.(5.6)) in the mushroom region. The red lines represent our simulation results.

5.3.1 Polymer effects in mushroom region

In the mushroom region, the spontaneous curvature and bending rigidity are linearly dependent on the polymer density ϕ. As is mentioned in Section 3.4.2, the linear relations

$$\kappa \Delta C_0 = 2 a_{\rm sp} k_{\rm B} T R_{\rm e} \phi / a_0 \tag{5.6}$$

$$\Delta \kappa = a_\kappa k_{\rm B} T R_{\rm e}^2 \phi / a_0 \tag{5.7}$$

can be obtained, where ΔC_0 and $\Delta\kappa$ are the differences of the spontaneous curvatures and bending rigidities between the polymer-decorated membrane and the pure membrane, respectively, and $R_{\rm e}$ is the mean end-to-end distance of the polymer chain. The factor 2 in Eq. (5.6) appears because in our definition of the spontaneous curvature in Eq. 5.1 is twice as large as that in the previous theoretical formula in Chapter 3. The reason is explained in Sec. 5.1. The coefficients are derived analytically using the Green's function [23, 24] and also estimated by Monte Carlo simulations of single anchored polymer chains [26]: $a_\kappa = 0.21$ and 0.2; and $a_{\rm sp} = 0.18$ and 0.17 for ideal and excluded-volume chains, respectively. Our results for the ideal chains agree very well with these previous predictions (compare the dashed lines and symbols in Figs. 5.5

and 5.6. Note that anchored ideal polymer chains can be considered in the mushroom region for any density ϕ, since the polymer chains do not directly interact with each other.

Supposed Err_{x} is the error bar of one individual quantity, where x represents κ, C_0, R_{e} and so on. In Fig. 5.6, we plot the error bar of a compound quantity $Err_{\kappa C_0/R_{\mathrm{e}}}$ as follows:

$$Err_{\kappa C_0/R_{\mathrm{e}}} = \kappa Err_{C_0} + C_0 Err_{\kappa} \tag{5.8}$$

Since $Err_{R_{\mathrm{e}}}$ is very small, we can ignore it here.

5.3.2 Comparisons with the scaling theory in brush region

For excluded-volume chains, our results deviate from the theoretical prediction (Eq. (5.6)) for the mushroom region at $\phi \gtrsim 0.1$. Thus, in the high density of anchored polymer chains, the interactions between polymer chains are not negligible. We compare our results with a scaling theory based on a blob picture for the brush region in Ref. [24]. We extract the numerical results from the nonlinear equation for a cylindrical surface

$$\frac{\partial f_{\mathrm{c}}(x)}{\partial x} + \frac{4\kappa_0}{k_{\mathrm{B}}T} N_{\mathrm{p}}^{-3} \bar{\Gamma}^{-3/2\nu} x = 0. \tag{5.9}$$

as has already been obtained in Section 3.4.3, where $f_{\mathrm{c}}(x) = [\{1 + (1+\nu)x/\nu\}^{\nu/(1+\nu)} - 1]/x - 1$ and κ_0 is the bending rigidity of the pure membrane. Because of $C_0 = 2c_0$, a reduced spontaneous curvature $x = h_0 C_0/2$ for the height $h_0 = N_{\mathrm{p}} \bar{\Gamma}^{(1-\nu)/2\nu} b$ of a brush on a flat surface. The polymer coverage on the membrane is normalized by the maximum coverage as $\bar{\Gamma} = \Gamma/\Gamma_{\max} = b^2\phi/a_0$, and the exponent $\nu = 0.6$ is used for excluded-volume chains. The bending rigidity is given by

$$\Delta\kappa = \frac{\nu + 2}{12\nu^2} N_{\mathrm{p}}^3 \bar{\Gamma}^{3/2\nu} k_{\mathrm{B}}T \tag{5.10}$$

in the small curvature limit as shown in Appendix A. Our results qualitatively agree with these predictions from the scaling theory (see Fig. 5.5 and 5.7). The deviation is likely due to the polymer length ($N_{\mathrm{p}} = 10$) in the simulation, which is too short to apply the blob picture in the scaling theory. The deviation is likely due to the polymer length ($N_{\mathrm{p}} = 10$) in the simulation, which is too short to apply the blob picture in the scaling theory. However, the application of short polymers only can make the blob picture obscure. It should not lead to so big a difference.

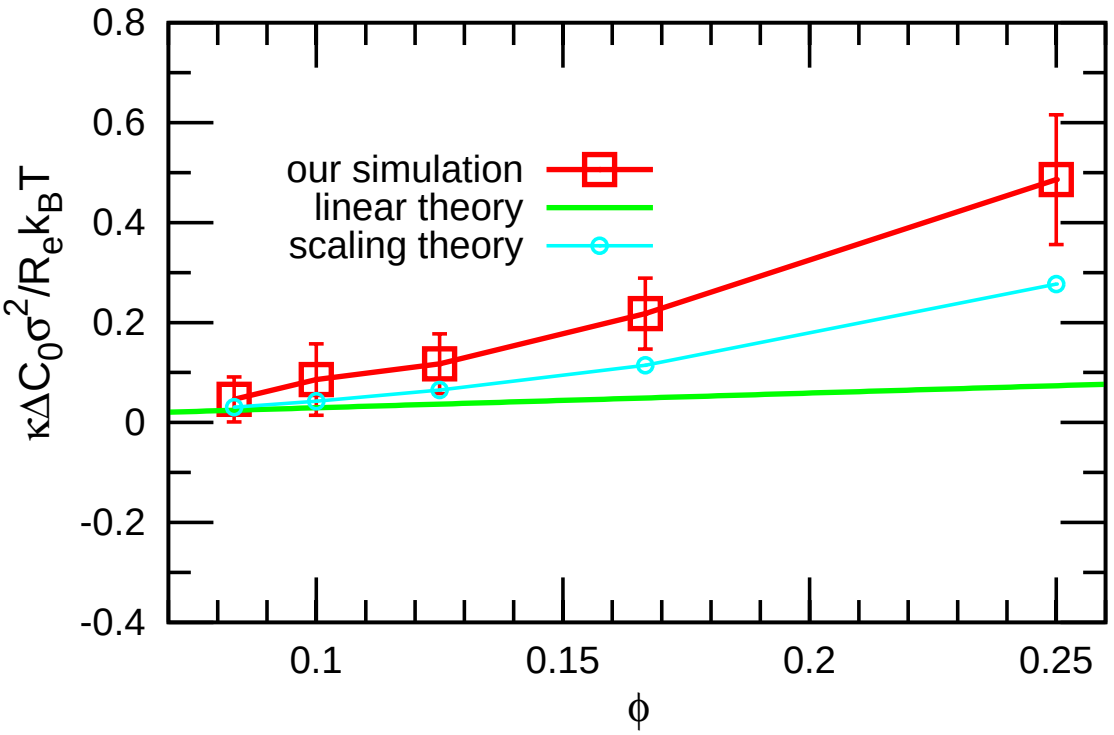

FIGURE 5.7: Comparison of a compound quantity $\kappa C_0/R_e$ theoretically defined by a linear theory in Ref. [26] and its estimation in our simulations for the excluded-volume chains. The green lines represent the linear theory (Eq.(5.6)) in the mushroom region. The red lines represent our simulation results. The light blue line represents the scaling theory (Eq.(5.7)) in the brush region.

The exact theoretical reason for the deviation is from the invalidity of the small curvature expansion formula (5.10) and (3.57). In the reference [24], the small curvature expansion must break down for $h_0/2R \lesssim 3\nu/(2\nu+4)$. But this relation is based on the second order expansions Eqs. (3.53) and (3.54) to the quantity h_0H, respectively, in that paper. But actually in our simulation h_0H is not a small quantity. Let us further expand Eqs. (3.53) and (3.54) up to the fifth order of the curvature as follows:

$$\begin{aligned}\Delta F_s &= F_0\Big[-\frac{1}{2\nu}(h_0H)+\frac{1}{3\nu^2}(h_0H)^2-\frac{1}{4\nu^3}(h_0H)^3+\frac{1}{5\nu^4}(h_0H)^4 \\ &\quad -\frac{1}{6\nu^5}(h_0H)^5+\mathcal{O}\left((h_0H)^6\right)\Big] \end{aligned} \tag{5.11}$$

and

$$\begin{aligned}\Delta F_{\mathrm{c}} &= F_0\Bigg[-\frac{1}{2\nu}(h_0H)+\frac{\nu+2}{6\nu^2}(h_0H)^2-\frac{(\nu+2)(2\nu+3)}{24\nu^3}(h_0H)^3 \\ &\quad+\frac{(\nu+2)(2\nu+3)(3\nu+4)}{120\nu^4}(h_0H)^4 \\ &\quad-\frac{(\nu+2)(2\nu+3)(3\nu+4)(4\nu+5)}{720\nu^5}(h_0H)^5 \\ &\quad+\mathcal{O}\left((h_0H)^6\right)\Bigg] \end{aligned} \tag{5.12}$$

For our cylindrical biomembranes in simulation, we have $\nu = 0.6$ and $h_0H = h_0/2R \approx 0.35$ in Eq. (5.12). Then we can theoretically estimate that the third term is about 0.61 of the value of the second term, the fourth one is about 0.68 of the one of the third term, and the fifth term is about 0.72 of the value of the fourth term. Thus, it means that when the polymer length is comparable to the cylinder radius, the small curvature expansion is invalid. To rescue it, we have to expand to enough order terms until the last term is less than 0.01 of the second order term so that we can safely omit higher order terms after it. Here we understand that intuitively the small curvature expansion only can be applied to the spherical or cylindrical surface with a very large radius compared with the polymer contour length.

5.4 Vesicle formation from stretched cylindrical biomembranes

For the case for excluded-volume chains, we found that due to the steric repulsion the anchored polymers can induce a neck shape along the the cylindrical axis. When the anchored polymer density is more than 0.333 for excluded-volume chains and if we gradually increase the axial force fz by increasing L_z along the axial direction, the neck part can become thinner and thinner. This finally leads to the vesiculation of the cylindrical biomembranes. We observed that the stretched cylindrical biomembrane patch self-assemblies into one vesicle under the densities $\phi = 0.333$ and 0.417, while the broken membrane patch self-assemblies into two vesicles at a higher density $\phi = 0.500$. It means that a large vesicle is able to separate into several small vesicles with the anchored polymer density increasing. But for the vesicles of the smaller size, even if the anchored polymer density is higher, it still keeps itself, not separates into several. This conclusion is very similar the one we obtained by investigating microdomain separation in 2D membrane patch described in Chapter 7.

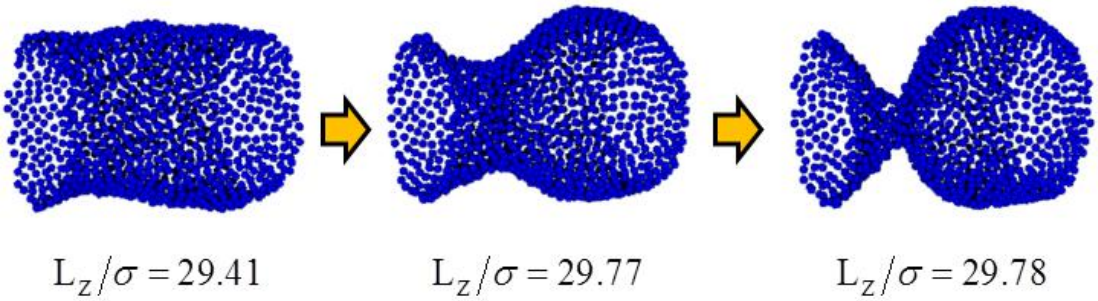

FIGURE 5.8: A snapshot of polymer-anchored vesicle formation process is shown for the cylindrical biomembranes with the anchored excluded-volume polymer density $\phi = 0.417$. To observe the process of vesicle transformation clearly, polymer particles are not displayed.

Fig. 5.8 shows a process for biovesicle formation from the stretched cylindrical biomembranes with the anchored excluded-volume polymer density $\phi = 0.417$. We found that a neck part is first created instead of the stretched pore in the case of stretched cylindrical biomembranes before the vesicle is formed finally. From Fig. 5.8 we found that the biomembrane stretching for the cylindrical case is different from the pure membrane stretching for the planar case [42]. The latter first forms a pore and then form a vesicle. Instead of any pore formation for the cylindrical biomembranes, pearling instabilities of membrane tubes have been verified by our simulation due to curvature-driven by anchored polymers. The reason is that the anchored excluded-volume polymers can form the brush region which has the strong steric effect to induce curvature before so that a neck shape can be formed in the stretched membrane part.

Fig. 5.9 shows that if the anchored polymer density is low (between 0.333 and 0.417), only one vesicle can be formed, while two vesicles can be formed if the anchored polymer density approach 0.5. It tells us that the number of the formed vesicles depends on the anchored polymer density. More details and conclusions still need further research in the future.

5.5 Summary for cylindrical biomembranes

In this chapter, we mainly used cylindrical geometry to estimate bending rigidity and spontaneous curvature of biomembranes. Most of previous studies paid attention to effects of polymer length or linear effects of many polymers (many ideal chains or many excluded-volume chains in the low density region) to mechanical properties of membranes. Here we mainly focus on effects of polymer density on mechanical properties of membranes, not only in linear region, but also in nonlinear region formed by a high

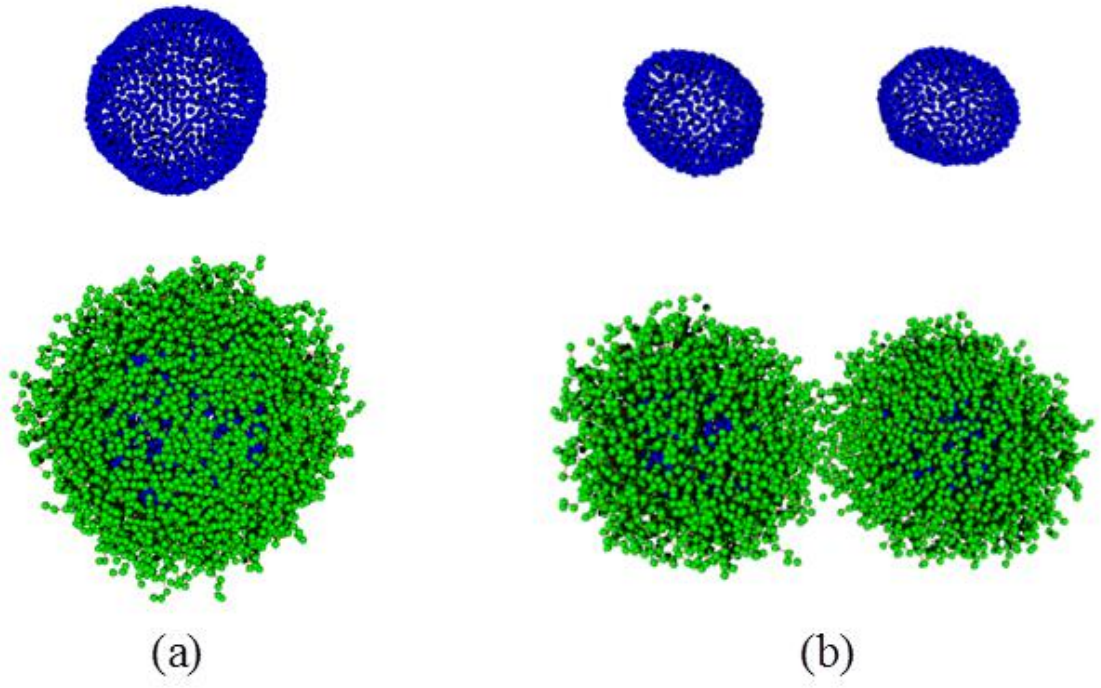

FIGURE 5.9: (a) shows that a single polymer-anchored vesicle is formed under the polymer density $\phi = 0.417$ after the cylindrical biomembranes overstretching. Only membrane particles are displayed in the upper graph, while both membrane and polymer particles are displayed in the lower graph. (b) shows that two polymer-anchored vesicles are formed under the polymer density $\phi = 0.500$ after the cylindrical biomembranes overstretching. Only membrane particles are displayed in the upper graph, while both membrane and polymer particles are displayed in the lower graph.

density of excluded-volume chains by simulation for the first time. Our simulation results agree very well with previous linear theory and scaling theory for ideal chains and excluded-volume chains in the low density. And our results qualitatively agree with the scaling theory in the high density. The reason was analyzed in Section 5.3.2. We also confirmed that end-to-end distance of anchored ideal polymer chains does not depend on anchored polymer density, but the one of anchored excluded-volume chains increases with anchored polymer density.

The vesiculation process is observed from stretched cylindrical biomembranes. Polymers tend to induce the spontaneous curvature and distribute uniformly. Such tendencies prefer to isotropically bend the cylindrical membrane and distribute uniformly at last. So we can find that biovesicles are finally formed from the snapshots 5.9. A higher density of anchored polymers can induce a bigger spontaneous curvature so that more vesicles are formed with bigger curvatures.

Experimentally, the κ increase of polymer-anchored membranes has been observed and measured [21, 29]. In addition, some experiments also have confirmed our simulation

results that pearling instabilities of membrane tubes can be driven by curvature induced by anchored polymers [126, 127].

Chapter 6

Edge Line Tension of Biomembranes

6.1 Simulation of strip biomembranes with two edges

Previous theoretical work mainly focuses on the mechanical properties of isotropic infinite membrane with/without anchored polymers in the thermodynamic limit [23, 24, 26]. In this chapter, we consider a realistic biomembrane system under the constraint condition of the finite boundary, that is, a strip of biomembrane with open edges so that we can study boundary effects and finite size effects of biomembranes in a more real situation.

A strip of a single-component membrane with anchored linear polymers is used to estimate the line tension Γ_{ed} of the membrane edges (see Fig. 6.1). In this chapter, we will investigate the line tension of membrane edges with various anchored polymer densities for both ideal chains and excluded-volume chains. And we also propose a phenomenological mean field theory to explain our simulation results on ideal chains.

6.1.1 The effective line tension on the edge

The line tension Γ_{ed} on the edge can be calculated by [117, 128, 129]

$$\Gamma_{\mathrm{ed}} = \frac{\partial F}{2\partial L_y} = \left\langle \frac{P_{xx} + P_{zz}}{2} - P_{yy} \right\rangle \frac{L_x L_z}{2}, \tag{6.1}$$

since the total edge length is $2L_y$. The pressure $P_{xx} = P_{zz} \approx 0$ for solvent-free simulation with a negligibly low critical micelle concentration. We checked that the line tension

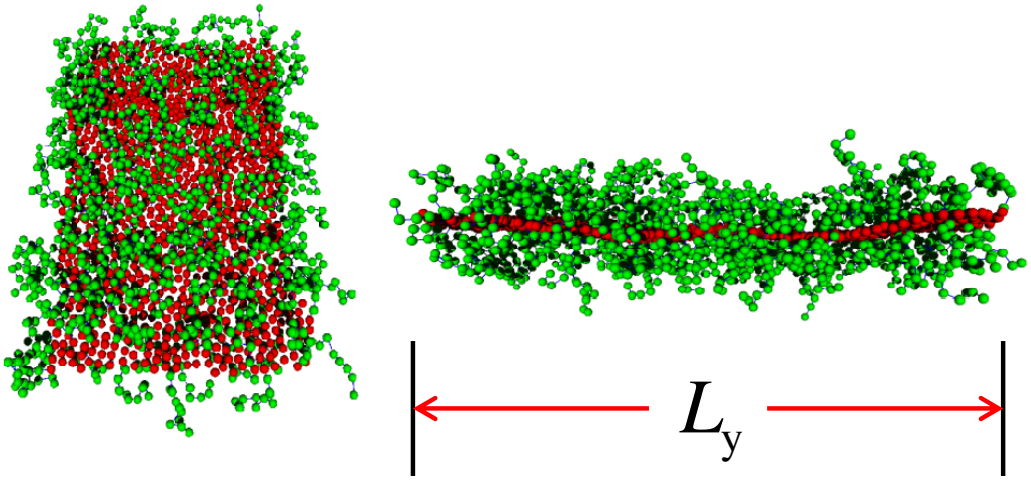

FIGURE 6.1: A snapshot of top and side views of a membrane strip with anchored excluded-volume chains at $\phi = 0.15$ and the length $L_y = 57.6\sigma$ of each membrane edge. Reproduced from Ref. [47] with permission of The Royal Society of Chemistry.

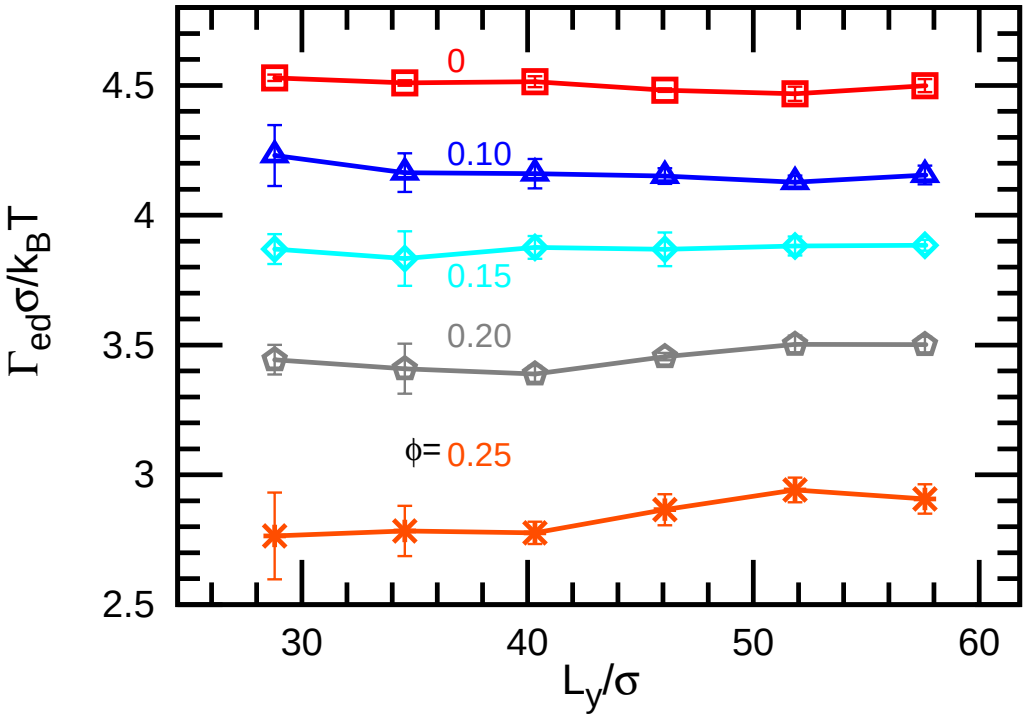

FIGURE 6.2: Line tension Γ_{ed} on the open edge of a membrane strip with anchored excluded-volume chains estimated for different edge lengths L_y at $\phi = 0$, 0.1, 0.15, 0.2, and 0.25. Reproduced from Ref. [47] with permission of The Royal Society of Chemistry.

is independent of the length of the membrane edge for pure membranes as well as for polymer-decorated membranes (see Fig. 6.2).

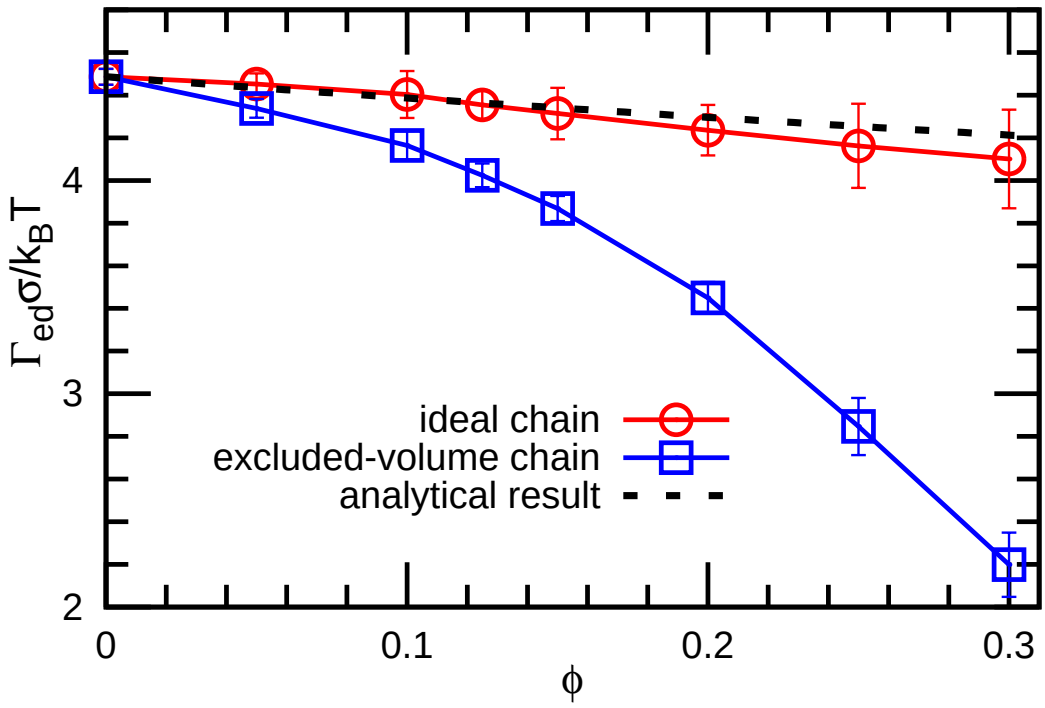

FIGURE 6.3: Polymer density dependence ϕ of the line tension of the membrane edges for ideal and excluded-volume chains. The blue line represents our theoretical prediction by Eq. (6.10). Reproduced from Ref. [47] with permission of The Royal Society of Chemistry.

Fig. 6.3 shows that the line tension Γ_{ed} decreases with increasing polymer density ϕ. The reduction for excluded-volume chains is much larger than that for ideal chains, similar to polymer effects on the bending rigidity. The polymer chains prefer staying on the edge, since there is more space to move so that they can gain entropy. Fig. 6.4 (a) shows that the polymer density distribution $\rho_{\rm chain}$ is nonuniform at the distance $d_{\rm w}$ from the strip's central axis. High peaks of $\rho_{\rm chain}$ are found close to the edges for both ideal chains and excluded-volume chains, while the density $\rho_{\rm mb}$ of all membrane particles has only very small peak. The relative polymer density $\rho_{\rm chain}/\rho_{\rm mb}$ more rapidly increases at the edges for larger mean density ϕ [see Fig. 6.4 (b)]. The mean polymer density ϕ_1 at the edges is calculated as an average $\langle \sum_{d_{\rm w}\geq d_{\rm w}^{\rm max}} \rho_{\rm chain} / \sum_{d_{\rm w}\geq d_{\rm w}^{\rm max}} \rho_{\rm mb} \rangle$ for the right region of the peak ($d_{\rm w}^{\rm max}$) of $\rho_{\rm mb}$ in Fig. 6.4 (a). The density difference from the mean value $\Delta\phi = \phi_1 - \phi$ increases with increasing ϕ as shown in Fig. 6.11. The excluded volume chains induce higher polymer concentration at the edges than the ideal chains.

6.1.2 Anchored polymers on the strip of biomembranes

6.1.2.1 Polymer distribution on the strip of biomembranes

In the case of self-assembled biomembrane system, ones have to notice that the excess anchored polymer density $\Delta\phi$ is not fixed, but adjusts itself to minimize the total free energy in the equilibrium state [93]. Thus, it is meaningful to see how the anchored polymers distribute when the biomembrane system approach the equilibrium state.

In Fig. 6.4, we show that most of anchored polymers always try to occupy the edge part of the strip membrane. Because the polymers can obtain more space to move on the edges so that they can obtain more configuration entropy. When the entropy of polymers compete with the free energy of membranes, the entropic effect can reduce the line tension of the strip membrane as shown in Fig. 6.3.

6.1.2.2 End-to-end distance of anchored polymers on the strip of biomembranes

In Chapter 5, we found that due to the constraints of the membrane part, anchored polymers exhibit the average end-to-end distance different from free polymer chains. the average end-to-end distance becomes longer than the free case. The strip shape is different from the cylindrical shape. For the cylindrical shape, any part has the same geometric constraint, while there is an obvious difference between the edge part and the middle part of the strip shape. Thus, it is quite interesting to study how the strip shape of membrane influences the end-to-end distance of anchored polymers and what is the difference between the edge parts and the middle part of membranes.

In this subsection, we study the changes of end-to-end distances with different distance from the central axis of the strip shape for the ideal chains and excluded-volume chains, respectively. The cases are shown in Fig. 6.5 and Fig. 6.6, respectively. We found that the anchored polymers in the middle part have the same end-to-end distance, while they have a short one at the edge parts of the strip biomembranes. A peak for the end-to-end distance comes up when the anchored polymers stays in the transition zone between the middle part and the edge part. It may be caused by the peak for the membrane particle distribution, which is shown in Fig. 6.5 (a) and Fig. 6.6 (a). There are basically no membrane particles outside the edge part, so the multi-body attractive potential decides a little bit higher distribution of membrane particle number close to the edge part than the one in the middle part. As explained in Chapter 5, the membrane part with the steric repulsion effect will elongate the end-to-end distance of anchored

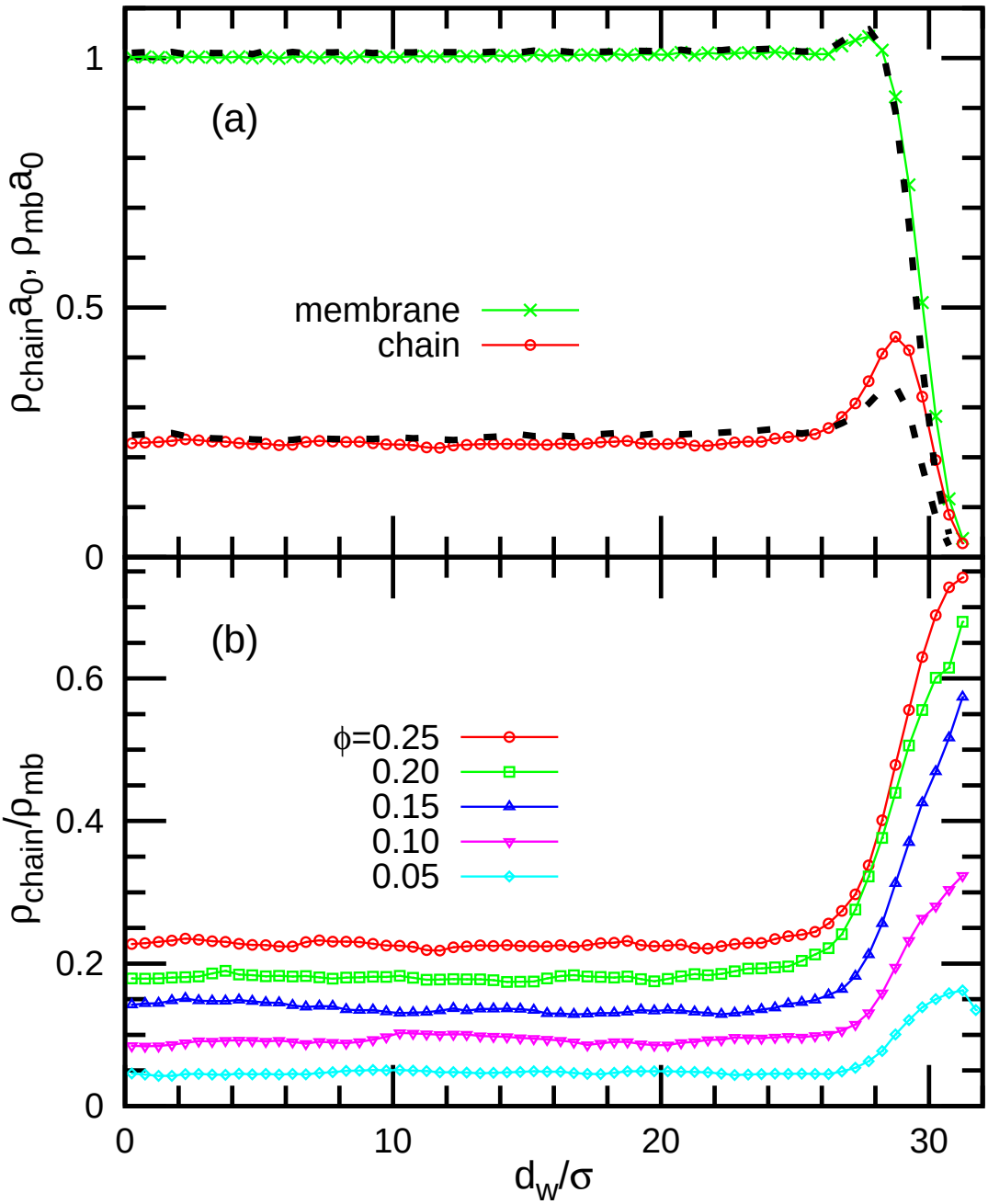

FIGURE 6.4: Density distribution on the membrane strip. (a) Density of polymer-anchored membrane particles $\rho_{\rm chain}$, and total density $\rho_{\rm mb}$ at $\phi = 0.25$. The solid lines with symbols and dashed lines represent the data for the excluded-volume chains, and ideal chains, respectively. (b) Density ratio $\rho_{\rm chain}/\rho_{\rm mb}$ for the excluded-volume chains. The distance $d_{\rm w}$ from the center of the strip is taken in the direction perpendicular to the edge. The membrane lengths are $L_{\rm st} = 60\sigma$ perpendicular to the edge and $L_y = 28.8\sigma$ along the edge. Reproduced from Ref. [47] with permission of The Royal Society of Chemistry.

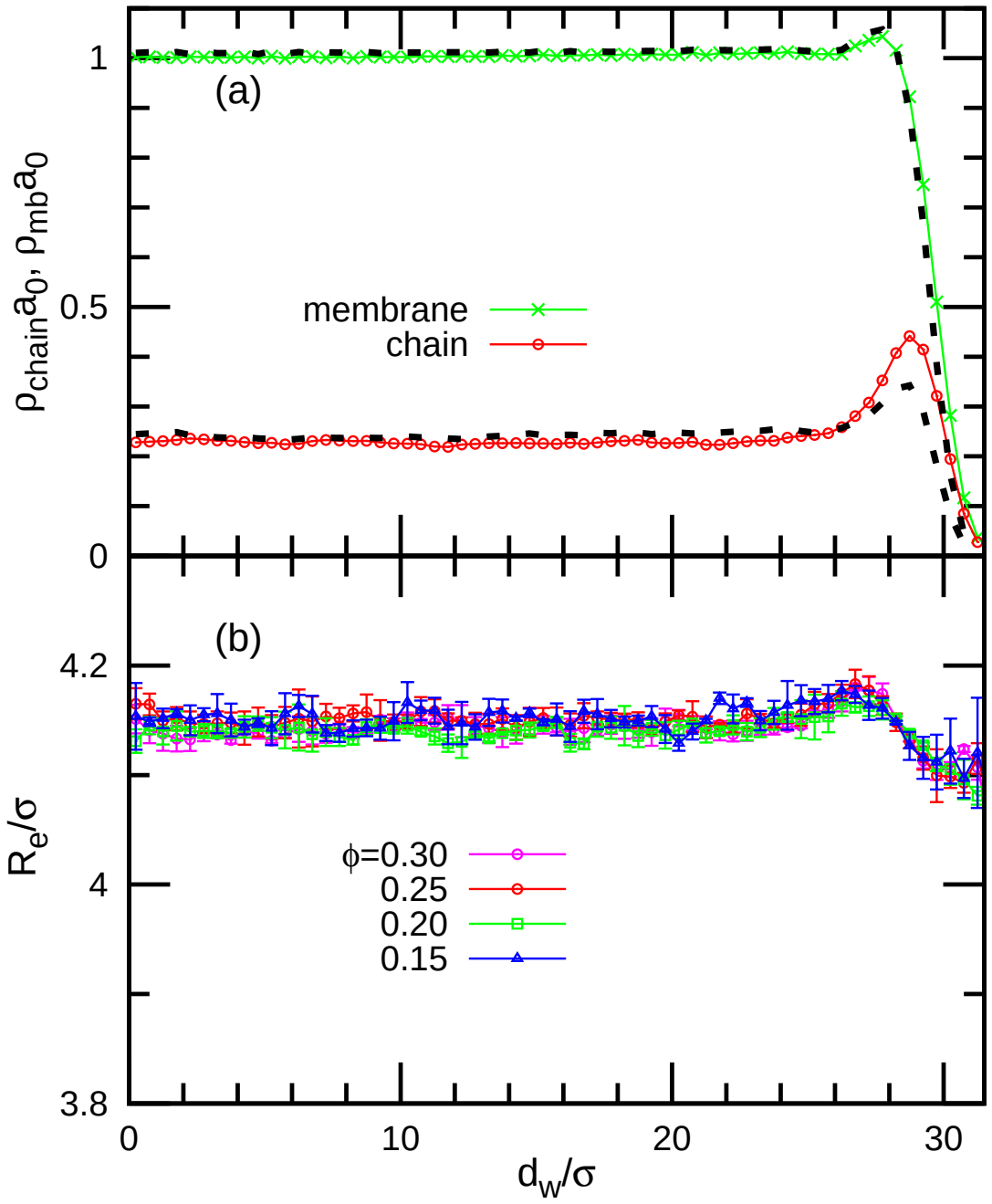

FIGURE 6.5: End-to-end Distance Distribution for Ideal Chains on the membrane strip. (a) Density of polymer-anchored membrane particles $\rho_{\rm chain}$, and total density $\rho_{\rm mb}$ at $\phi = 0.25$. The solid lines with symbols and dashed lines represent the data for the excluded-volume chains, and ideal chains, respectively. (b) End-to-end Distance $R_{\rm e}$ for the ideal chains is shown. The distance $d_{\rm w}$ from the center of the strip is taken in the direction perpendicular to the edge. The membrane lengths are $L_{\rm st} = 60\sigma$ perpendicular to the edge and $L_y = 28.8\sigma$ along the edge.

polymers, so a higher distribution of membrane particle number leads to a bit larger end-to-end distance of the anchored polymers close to the edge part.

By comparing Fig. 6.5 and Fig. 6.6, we found that the excluded-volume chains can stabilize the strip biomembranes and gives us stable results with the small error bars. This conclusion is very similar to the one made in Chapter 5, where we found that the excluded-volume chains can stabilize the cylindrical biomembranes by suppressing the big fluctuations of membranes.

6.2 Theory for anchored ideal chains

As mentioned in Chapter 3, chemists spend much of their time developing polymer with specific chemical or physical properties, which are determined by their linked monomers or mutual bindings. But physicists pay attention to universal properties which depend only on the fact that the polymer is a long linear molecule, and determined by 'large scale quantities' such as the quality of the solvent in which the polymer is immersed, the temperature, the presence of surfaces, and so on. Keeping these in mind, we can introduce a description of polymers in terms of random and self avoiding walks for ideal polymers and excluded-volume polymers, respectively. When we add a large number of monomers to form a long polymer, one can understand that the correlation between bond orientations emerging on the monomer level will decay on larger length scales, until beyond a certain persistence length l_{p}, which is called as Kuhn length, the orientations between bonds become completely uncorrelated. This concept of persistence length is sufficient for us to work with the above intuitive idea to introduce our model for polymer chains [130].

6.2.1 Lattice model for a restricted ideal chain

Polymers can show many interesting mesoscopic properties which can be adequately represented by using coarse-grained models. Lattice models, which have a history of about six decades, are old, but particularly useful since they employ integer coordinates which can be quickly processed. Another advantage is the possibility of checking the occupancy of the discrete number of sites and store it in an array. Therefore, overlapping or not between beads can be easily executed or avoided. Many early simulations were usually performed with the simple cubic lattices, employing different algorithms.

Based on the independence of bond directions when ones consider a polymer on length scales above the persistence length leads to the simplest model for an isolated polymer.

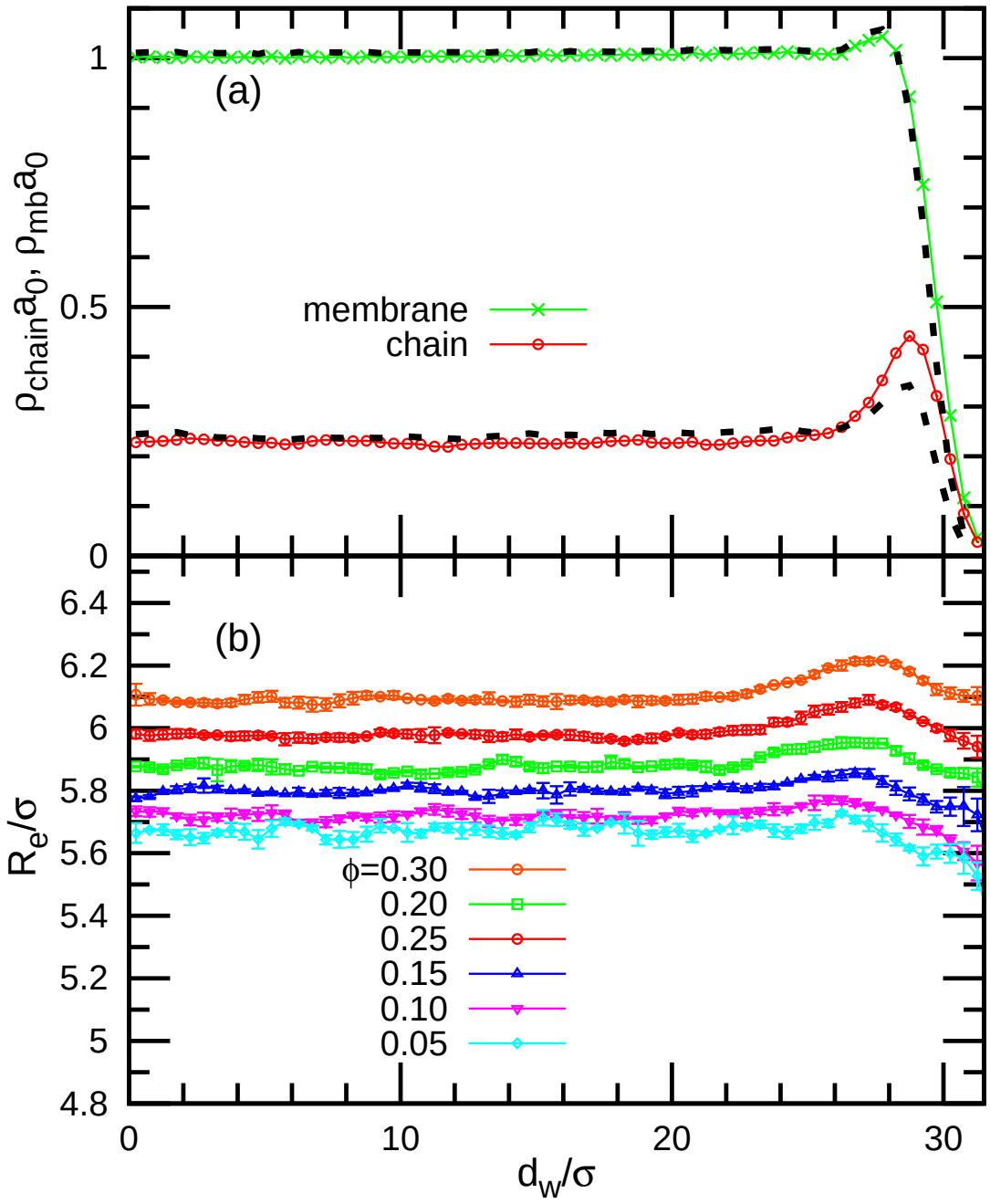

FIGURE 6.6: End-to-end Distance Distribution for Ideal Chains on the membrane strip. (a) Density of polymer-anchored membrane particles $\rho_{\rm chain}$, and total density $\rho_{\rm mb}$ at $\phi = 0.25$. The solid lines with symbols and dashed lines represent the data for the excluded-volume chains, and ideal chains, respectively. (b) End-to-end Distance $R_{\rm e}$ for the excluded-volume chains is shown. The distance $d_{\rm w}$ from the center of the strip is taken in the direction perpendicular to the edge. The membrane lengths are $L_{\rm st} = 60\sigma$ perpendicular to the edge and $L_y = 28.8\sigma$ along the edge.

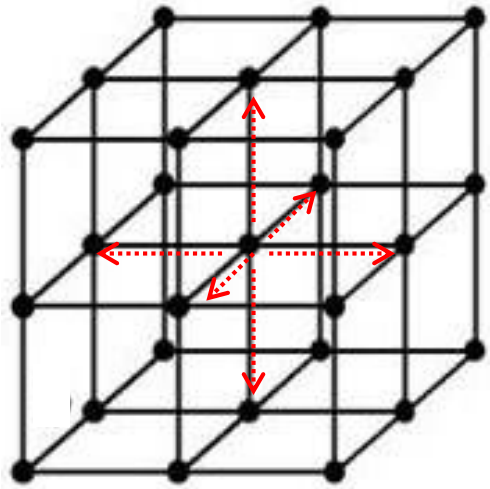

FIGURE 6.7: A simple lattice model is plotted for modeling a 3D free polymer. There are six independent directions for the next step of every end monomer in the 3D lattices.

In this model, the polymer is modeled as a random walk, which has a long history for detailed discussions. Here we only focus on 3D lattice random walks. As shown in Fig. 6.7, there are six independent directions (six nearest neighbor points) for the next step motion of every end monomer in the 3D lattices. For random walks for ideal polymer chains, the segments of the polymer chain are allowed to overlap with each other. So for each polymer segment in 3D free space, we have the configuration distribution probability of the polymer with N segments, that is, the reduced polymer weight (or partition function) $W = 6^N$. To be generalized, consider a hypercubic lattice $\mathbb{Z}^d$ in d dimensions. A random walker goes at each step with equal probability, then we have a generalized reduced weight $(2d)^N$ for a free polymer.

In this thesis, we extend the pervious lattice polymer model to the restricted half space case and the restricted edge case, which are, respectively, shown in Fig. 6.8.

For counting the reduced weight of a restricted ideal polymer above a plane, we know that the polymer cannot move down or touch on the plane because of the constraint. Thus, the first segment of an ideal polymer has only one probability, that is, the motion upwards. Supposed the plane is the zeroth layer, once the segment end move up to the first layer of lattice, the next segment has 5 probable directions for motion, while once the segment move up to the layers higher than the first layer, the case goes back the one for a free polymer, that is, the next segment always has 6 probable directions for motion. From this analysis, we can divide a half space lattice random walk into three cases to calculate the probabilities: one probability is to move upward, four probabilities is to move horizontally, and one probability is to move downward, which, however, is restricted in term of whether its last step is in the first layer or not. Thus, we can easily

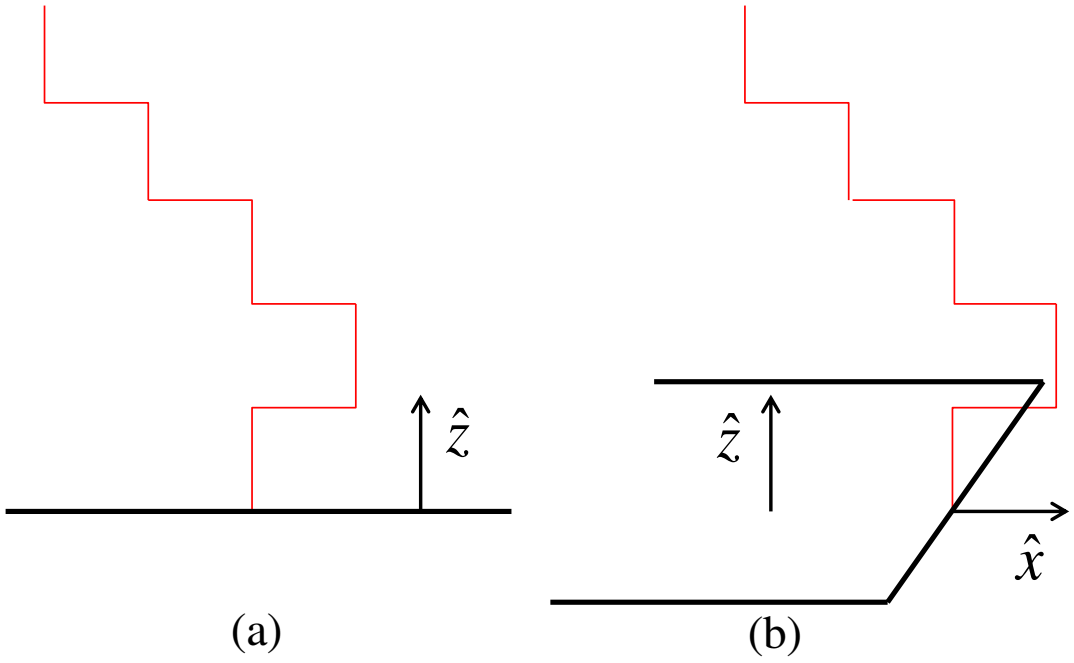

FIGURE 6.8: Our improved Lattice models for the ideal polymers restricted on the half space above the plane (a) and at the edge of a plane (b). The normal vector to the plane is defined as **z** direction, and the horizontal direction is defined as **x** direction.

deduce a general procedure to calculate the reduce weight of the ideal chain restricted on a plane as follows:

$$\begin{aligned} W_{\rm hs}(N,Z) &= W_{\rm hs}(N-1,Z+1)+4W_{\rm hs}(N-1,Z)+W_{\rm hs}(N-1,Z-1), \\ W_{\rm hs}(N) &= \sum_{Z=-N}^{N} W_{\rm hs}(N,Z). \end{aligned} \tag{6.2}$$

with the initial conditions:

$$\begin{aligned} W_{\rm hs}(1,1) &= 1, \\ W_{\rm hs}(1,-1) &= 1, \\ W_{\rm hs}(1,0) &= 0, \\ W_{\rm hs}(N,Z) &= 0 \ (|Z|>N). \end{aligned} \tag{6.3}$$

where $W_{\rm hs}(N)$ is the reduced weight of an ideal polymer chain restricted on a half space by an anchored plane, $W_{\rm hs}(N,Z)$ is the reduced weight of an ideal polymer with the length N in the Zth layer which depends on that of the previous $(N-1)$th polymer segment.

To follow a similar procedure, we also can obtain the calculation way to the case of the

ideal chain anchored at the edge of a plane. In this case, besides considering different layers in $\hat{z}$ direction, ones also have to consider the horizontal $\hat{x}$ direction proportional to the edge line as well as $\hat{z}$ direction. This $\hat{x}$ is applied to judge whether the lattice polymer end moves back onto the plane or outside plane. Suppose the edge line has the coordinate $X = 0$ and the segments outside the plane have $X > 0$, if the polymer end moves back onto the plane, that is $X < 0$, then the case goes back to the last half-plane case, while if the polymer end moves outside the plane, then the case is the free-space case. Thus, we can easily deduce the feasible calculation procedures as follows:

$$\begin{aligned} W_{\rm ed}(N,Z,X) &= W_{\rm ed}(N-1,Z,X-1) + 2W_{\rm hs}(N-1,Z,X) + W_{\rm hs}(N-1,Z,X+1) \\ &\quad + W_{\rm ed}(N-1,Z-1,X) + W_{\rm hs}(N-1,Z+1,X), \\ W_{\rm ed}(N) &= \sum_{Z=-N}^{N}\sum_{X=-N}^{N} W_{\rm hs}(N,Z,X). \end{aligned} \tag{6.4}$$

with the initial conditions:

$$\begin{aligned} W_{\rm ed}(1,-1,0) &= 1, \\ W_{\rm ed}(1,1,0) &= 1, \\ W_{\rm ed}(1,0,1) &= 1, \\ W_{\rm ed}(N,0,X) &= 0 \ (X \leqslant 0), \\ W_{\rm ed}(N,Z,X) &= 0 \ (|Z| > N, |X| > N). \end{aligned} \tag{6.5}$$

where $W_{\rm ed}(N)$ is the reduced weight of an ideal polymer chain restricted at the edge of an anchored plane, $W_{\rm hs}(N,Z,X)$ is the reduced weight of an ideal polymer with the length N in the Zth layer inside or outside the plane, which depends on the coordinate value of the polymer segment in $\hat{x}$ direction.

From the above deduction, we can esitmate $W_{\rm hs}(N)$ and $W_{\rm ed}(N)$, which are abbreviated to $W_{\rm hs}$ and $W_{\rm ed}$, for different polymer contour lengths N. Then the restricted partition functions $Z_{\rm hs}$ and $Z_{\rm ed}$ can easily be obtained by the integration over all possible positions of the free end of the lattice polymer: $Z_{\rm hs} = q^N W_{\rm hs}$ and $Z_{\rm ed} = q^N W_{\rm ed}$, where $q = 6$ is for the cubic lattice model. In this work, we are interested in the partition function ratio $Z_{\rm ed}/Z_{\rm hs} = W_{\rm ed}/W_{\rm hs}$, which is the key quantity to measure the excess configuration entropy ΔS, because $\Delta S = \ln(W_{\rm ed}/W_{\rm hs})$. Generally the polymer at the edge has more configuration entropy than the one anchored on the plane because of less restriction). We can plot the change of the ratio $W_{\rm ed}/W_{\rm hs}$ with the polymer length N, which is shown in Fig. 6.9.

In this thesis, only $N_{\rm p} = 10$ is employed. In Fig. 6.9, we easily know $W_{\rm ed}/W_{\rm hs} \simeq 2$ for $N_{\rm p} = 10$.

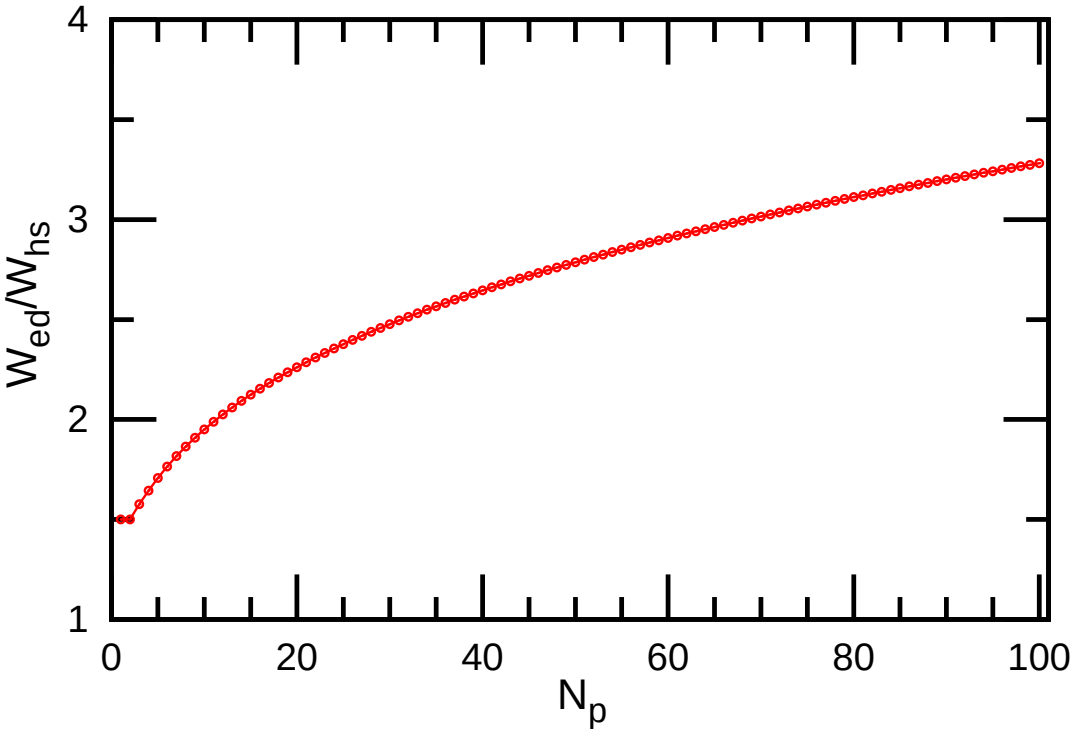

FIGURE 6.9: Probability Ratio $W_{\rm ed}(N_{\rm p})/W_{\rm hs}(N_{\rm p})$ of a linear Restricted Ideal Chain changes with different polymer length N.

6.2.2 Mean field theory for strip biomembranes with ideal chains

Based on the above 3D polymer lattice model, we further propose a mean field theory for the line tension induced by the anchored polymers in the mushroom region. According to the nonuniform polymer distribution on the membrane strip, we divide the membrane into two regions, the edge (blue part, region 1) and middle region (yellow part, region 2) as shown in Fig. 6.10. The polymer density is assumed to be uniform in each region. The area fractions of the two regions are n_1 and n_2 with $n_1 + n_2 = 1$, and the polymer densities are ϕ_1 and ϕ_2 with $\phi = n_1\phi_1 + n_2\phi_2$. The width of region 1 is considered the radius of gyration of polymer $R_{\rm g}$, so that the area fraction is given by

$$n_1 = \frac{2L_y R_{\rm g}}{N_{\rm mb} a_0}. \tag{6.6}$$

The free energy of the membrane strip is written as

$$\begin{aligned} \frac{F_{\rm ed}}{N_{\rm mb} k_{\rm B} T} &= n_1\phi_1 \ln\phi_1 + n_1 (1-\phi_1) \ln(1-\phi_1) \\ &\quad + n_2\phi_2 \ln\phi_2 + n_2 (1-\phi_2) \ln(1-\phi_2) \\ &\quad - n_1\phi_1 \Delta S + f_0 \end{aligned} \tag{6.7}$$

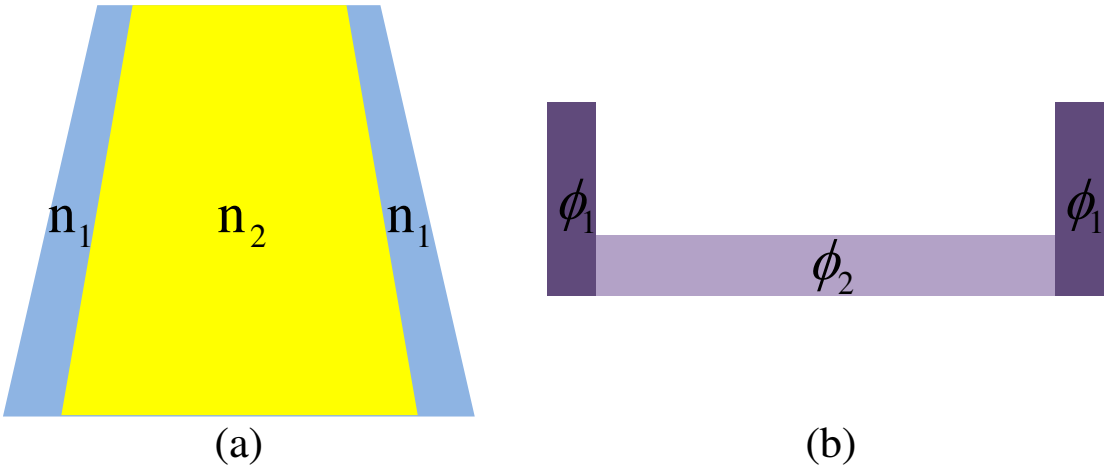

FIGURE 6.10: (a) shows that a strip shape of biomembranes can be simply divided into two regions: the edge region and the middle region with the area fractions of n_1 (blue part, region 1) and n_2 (yellow part, region 2). (b) shows the anchored polymer distribution on the strip biomembranes, the high columns with dark purple represent the high polymer density ϕ_1 at the edges, while the low column with light purple represents the low polymer density ϕ_2 in the middle part of the strip biomembranes.

where f_0 is the free energy contribution of the membrane without polymer grafting. The first four terms are the mixing entropy for regions 1 and 2. When a polymer chain moves from the middle region to the open edges, it gains the excess conformational entropy ΔS.

The partition function of a single anchored polymer chain is expressed as $Z_{\rm p} = q^{N_{\rm p}} W$, where q is the number of the nearest neighbors in the lattice model ($q = 6$ in a cubic lattice). The restricted weight of a polymer anchored on the flat membrane is $W_{\rm hs} = \mathrm{erf}\left[\frac{\sqrt{q} l_{\rm an}}{2R_{\rm e}}\right]$, where $\mathrm{erf}(x)$ is the error function and $l_{\rm an}$ is the anchor length [23, 24]. On the other hand, the free end of a polymer anchored on the edge can also move the other half space, and has a larger value of weight $W_{\rm ed}$. We numerically counted the weights $W_{\rm ed}$ and $W_{\rm hs}$ in a cubic lattice. The ratio $W_{\rm ed}/W_{\rm hs}$ increases with increasing $N_{\rm p}$, and $W_{\rm ed}/W_{\rm hs} \simeq 2$ for $N_{\rm p} = 10$. Thus, the excess entropy is estimated as $\Delta S = \ln\left(W_{\rm ed}/W_{\rm hs}\right) \simeq \ln 2$ for our simulation condition.

Using minimization of $F_{\rm ed}$, the polymer density ϕ_1 in the edge region is analytically derived as

$$\begin{aligned} \phi_1 &= \frac{2Q\phi}{s + \sqrt{s^2 - 4Q(Q-1)\phi n_1}} \\ &= \frac{Q\phi}{1+(Q-1)\phi}\left(1 - \frac{(Q-1)(1-\phi)}{\{1+(Q-1)\phi\}^2} n_1\right) + O(n_1^2) \end{aligned} \tag{6.8}$$

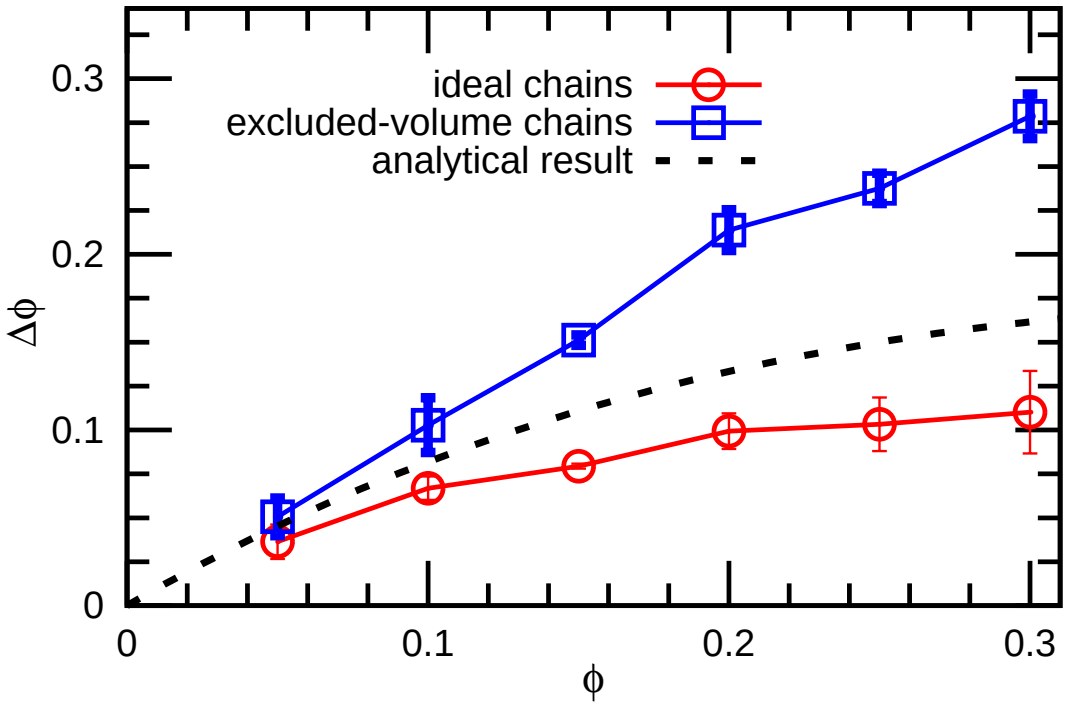

FIGURE 6.11: Excess polymer density $\Delta\phi \equiv \phi_1 - \phi$ at the membrane edge as a function of the mean polymer density ϕ. The solid lines with circles and squares represent our simulation results for the ideal chains (red) and excluded volume chains (blue), respectively. The dashed line represents our theoretical prediction for the ideal chains by Eq. (6.8). Reproduced from Ref. [47] with permission of The Royal Society of Chemistry.

where $Q = \exp(\Delta S)$ and $s = 1 + (Q-1)(\phi + n_1)$. At $Q = 2$ and $n_1 \ll 1$, the density difference is simply $\Delta\phi \equiv \phi_1 - \phi = \phi(1-\phi)/(1+\phi)$, which agrees very well with the simulation results as shown in Fig. 6.11.

In Fig. 6.11, our simulation result for ideal chains (red solid line) is lower than the theoretical prediction because our mean field theory naively consider that one strip patch of biomembranes can be simply divided into two types of rectangular parts with different anchored polymer densities as shown in Fig. 6.10, while our simulation result for excluded-volume chains (blue solid line) is higher than the theoretical prediction because our mean field theory is proposed for anchored ideal chains, but excluded-volume chains have stronger steric repulsive interaction among different polymer chains, then more polymers are pushed to the edge parts of the biomembrane strip.

The line tension is derived as $\Gamma_{\rm ed} = \partial F_{\rm ed}/\partial L_{\rm ed}$, where $L_{\rm ed}$ is the total edge length $L_{\rm ed} = 2L_y$. Thus, the polymer-induced line tension $\Delta\Gamma_{\rm ed}$ is given by

$$\begin{aligned}\frac{\Delta\Gamma_{\rm ed}a_0}{R_{\rm g}k_{\rm B}T} &= \ln(1-n_1) + \phi_1 \ln\frac{\phi_1}{Q(\phi-\phi_1 n_1)} \\ &\quad +(1-\phi_1)\ln\frac{1-\phi_1}{1-\phi-(1-\phi_1)n_1}.\end{aligned} \tag{6.9}$$

At $Q = 2$, the Taylor expansion gives

$$\frac{\Delta\Gamma_{\rm ed}a_0}{R_{\rm g}k_{\rm B}T} = -\ln(1+\phi) + \frac{\phi(1-\phi)}{(1+\phi)^2}n_1 + O(n_1^2). \tag{6.10}$$

Thus, the line tension $\Gamma_{\rm ed}$ decreases with increasing ϕ and is independent of the edge length L_y for $n_1 \ll 1$. Figure 6.3 shows the comparison of line tensions between our simulation and the theoretical results for ideal chains; The agreement is excellent. As the membrane strip becomes narrower (n_1 increases), the polymer effect on the line tension $\Gamma_{\rm ed}$ is reduced by the loss of mixing entropy in region 2, and $\Gamma_{\rm ed}$ increases with increasing edge length L_y. This conclusion is consistent with our results on the reduced interfacial line tension 7, since the non-edge polymers have more contributions to reduce the line tension. When the edge length increases, more non-edge polymers move to the edge to obtain more entropy. This leads that the percentage of edge polymers increases, while that of non-edge polymers decreases, so the line tension increases.

6.3 Summary for strip biomembranes

In this chapter, we employed strip geometry to calculate edge line tension of biomembranes by simulation and theory for the first time. Here we mainly paid attention to effects of polymer density on edge line tension of membranes. The reduction of edge line tension caused by anchored polymers has been confirmed by simulation. The reason is that polymers prefer to stay on the edges of strip biomembranes because of polymer configuration entropy. Based on polymer distribution on the strip membranes, we proposed a mean field theory for anchored ideal polymer chains. Our simulation results agree very well with our theoretical predictions for ideal chains. Excluded-volume chains can reduce edge line tension more than ideal chains due to the steric repulsion. We also confirmed that end-to-end distance and its distribution of anchored ideal polymer chains does not depend on anchored polymer density, but the ones of anchored excluded-volume chains increases with anchored polymer density. The results on end-to-end distance are similar to the ones obtained from cylindrical cases.

In the experiments, people found that polymer anchoring induces the formation of large vesicles [39] and spherical or discoidal micelles [40]. Since the ratio between the edge tension and the bending rigidity determines the vesicle radius $R_{\rm ves}$ formed by the membrane disks as $R_{\rm ves} \sim (2\kappa+\bar{\kappa})/\Gamma_{\rm ed}$, the reduction in the edge tension increases the vesicle radius. Our results are consistent with these experimental observations.

Chapter 7

Interfacial Line Tension and Microdomain Separation on Biomembranes

The investigation on domains in multi-component membranes with anchored polymer chains is the most exciting topic in this thesis. In this section, we focus on the effects of polymer-grafting-induced interfacial tension. First, in Sec. 7.1 we estimate the line tension of polymer-anchored membrane domains, and then in Sec. 7.2 we investigate the polymer effects on domain separation and domain shape transformation. Here, we investigate only the membranes with excluded-volume chains, since the effects of the ideal chains are considered to be very small. As described in Chapter 5, polymers can induce an effective spontaneous curvature in the membrane. In order to diminish the influence of the induced spontaneous curvature, we symmetrically graft polymer chains on both sides of the membrane as shown in Fig. 7.1. Half of the chains ($N_{\rm chain}/2$) are anchored on the upper (lower) side of the membrane, and each chain is anchored on one membrane particle. Then, the net curvature effects induced on both sides of the membrane cancel each other out. Our handling is also consistent with the assumption from the experimental observations as shown in Fig. 4.3.

7.1 Interfacial line tension between two coexisting domains

7.1.1 The case of a strip domain

The line tension $\Gamma_{\rm AB}$ between the type A and B domains is estimated by two methods using a striped domain and a circular domain. For the striped domain shown in

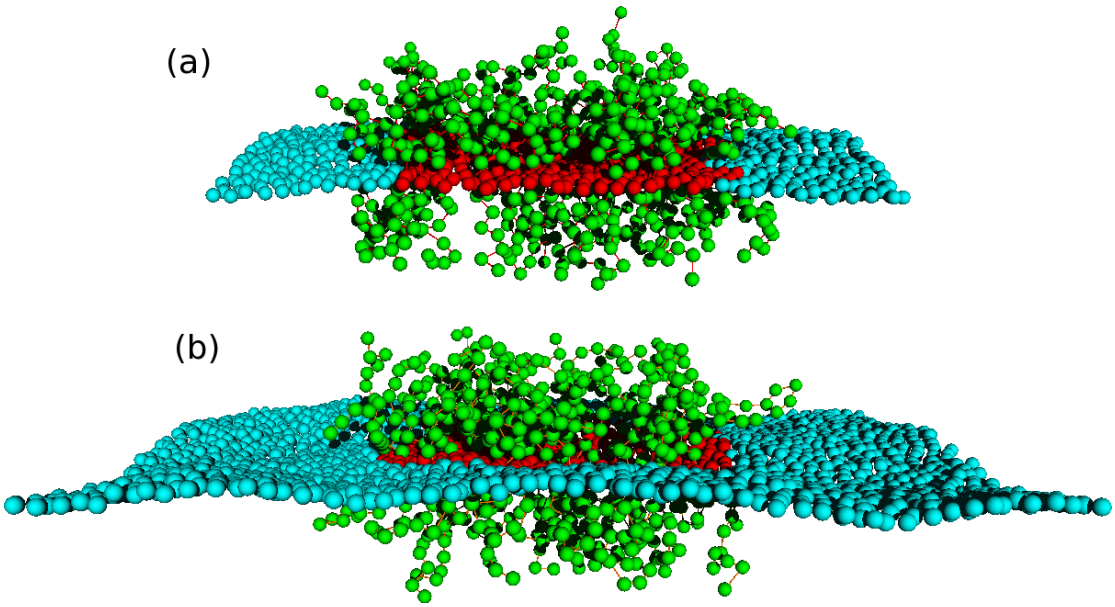

FIGURE 7.1: Snapshots of (a) striped and (b) circular domains with anchored excluded-volume chains in two-component planar membranes at $N_A = 400$ and $\phi = 0.3$. Type A and B membrane particles are displayed in red and blue, respectively. Reproduced from Ref. [47] with permission of The Royal Society of Chemistry.

Fig. 7.1(a), the line tension is calculated by

$$\Gamma_{AB} = \langle P_{xx} - P_{yy} \rangle L_x L_z / 2. \tag{7.1}$$

The obtained line tension for tensionless membranes is shown by solid lines in Fig. 7.2. We ensured that Γ_{AB} is independent of the boundary length L_y for $24 < L_y/\sigma < 48$. The line tension Γ_{AB} decreases with increasing ϕ, while Γ_{AB} increases with increasing ε_{AB}. Thus, the same value of Γ_{AB} can be obtained for the different polymer density ϕ by adjusting ε_{AB}.

7.1.2 The case of a circular domain

Before investigating polymer effects on the domain shapes in the next subsection, we also estimate Γ_{AB} from the circular domain shown in Fig. 7.1(b). Because the free energy G of the whole circular domain is composed of surface free energy and line free energy as follows:

$$G = \Delta\gamma \pi \bar{R}^2 - \Gamma_{AB} 2\pi \bar{R}, \tag{7.2}$$

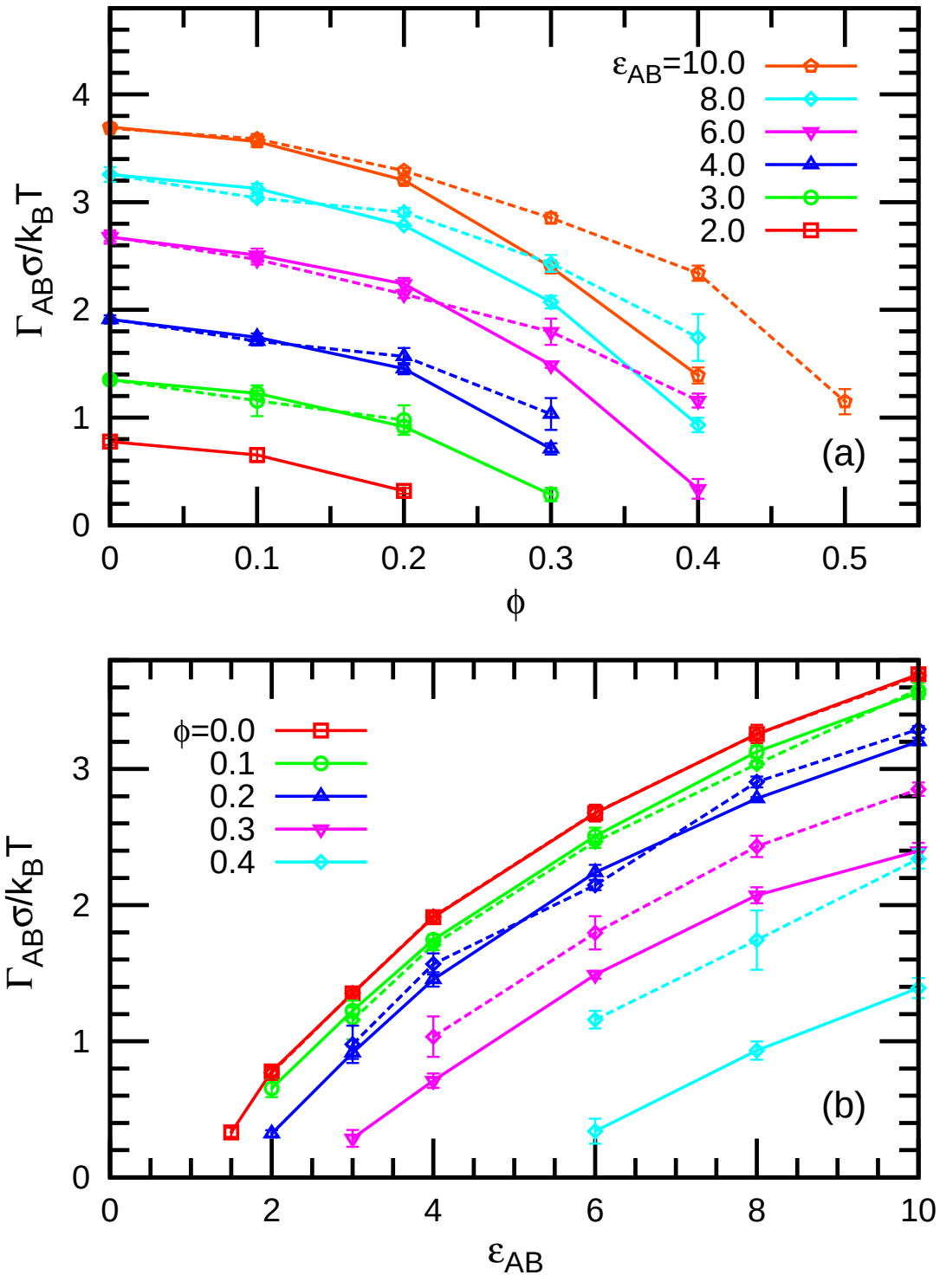

FIGURE 7.2: Interfacial line tension Γ_{AB} between membrane domains as a function of (a) ϕ and (b) ε_{AB}. The solid and dashed lines represent Γ_{AB} estimated from the striped domain and the circular domain, respectively. Reproduced from Ref. [47] with permission of The Royal Society of Chemistry.

where the negative sign indicates that the line energy always resists surface area shrinking. Because the whole domain lies in a fluctuating fluid environment and the domain boundary is dynamic, we have to use an average radius $\bar{R}$ to measure the domain size.

By minimizing the free energy G, one obtains a 2D Laplace equation so that the line tension $\Gamma_{\rm AB}$ can be calculated by the 2D Laplace pressure

$$\Gamma_{\rm AB} = \bar{R}\Delta\gamma, \tag{7.3}$$

where $\bar{R}$ is the average radius of the domain, and $\Delta\gamma$ is the difference of surface tension between the type A and B domains: $\Delta\gamma = \gamma^{\rm in} - \gamma^{\rm out}$, where $\gamma^{\rm in}$ is the surface tension of the inner (type A) domain and $\gamma^{\rm out}$ is that of the outer (type B) domain. Both of them can be estimated by the pressure tensors of the local regions

$$\gamma^{\alpha} = \langle P^{\alpha}_{zz} - (P^{\alpha}_{xx} + P^{\alpha}_{yy})/2\rangle L_z, \tag{7.4}$$

where α represents "in" or "out"; P^{α}_{xx}, P^{α}_{yy}, and P^{α}_{zz} are the diagonal components of the pressure tensors calculated in the local membrane regions. The outer surface tension $\gamma^{\rm out}$ can also be calculated from the pressure tensors for all regions.

To estimate $\gamma^{\rm in}$ and $\gamma^{\rm out}$, we extract the inner and outer regions as follows. First, domains of type A particles are calculated. The particles are considered to belong to the same cluster (domain) when their distance is less than $r_{\rm cut} = 2.1\sigma$. Then the radius $\bar{R}$ of the largest domain is calculated. Type A particles contacting type B particles (closer than $r_{\rm cut}$) are considered domain boundary particles. The number of boundary particles is $N_{\rm bd}$. In the largest domain, the distance of the domain particles from the center $\mathbf{r}_{\rm G}$ of the domain is averaged by $R_{\rm A} = (1/N_{\rm bd})\sum|\mathbf{r} - \mathbf{r}_{\rm G}|$. For the mean radius of the domain boundary, the half boundary width $\sqrt{a_0}/2 = 0.6\sigma$ is added so that $\bar{R} = R_{\rm A} + 0.6\sigma$. Then, the maximum fluctuation amplitude ΔR around $\bar{R}$ is calculated. The surface tension $\gamma^{\rm in}$ is estimated within the area inside the circular region with radius $\bar{R} - \Delta R - 0.5\sigma$, while $\gamma^{\rm out}$ is estimated within the area outside the circular region with radius $\bar{R} + \Delta R + 0.5\sigma$. Note that a few type B particles can enter the type A domain at small $\Gamma_{AB}\sigma/k_{\rm B}T \sim 1$ so the type A particles neighboring these isolated particles are not taken into account for estimation of $\bar{R}$ and ΔR.

The line tension estimated from the 2D Laplace pressure is shown by dashed lines in Fig. 7.2. For the pure membrane, the obtained values agree with those from the membrane strip very well. However, they are slightly larger for the polymer-anchored membranes. This deviation is likely caused by the relative larger boundary region of the circular domain than the striped domain. It is a similar dependence obtained for the membrane edges (see Eq. (6.10)).

7.2 Polymer-induced microdomain separation

To clarify the anchored polymer effects, we compare the shape changes of the type A membrane domains with increasing ϕ and with decreasing $\varepsilon_{\mathrm{AB}}$. In both cases, the interfacial line tension Γ_{AB} decreases and the low line tension leads to the breakup of domains. However, the resultant states are quite different as shown in Fig. 7.3. As the repulsive interaction between the type A and B particles is reduced with decreasing $\varepsilon_{\mathrm{AB}}$, the obtained phase behavior is similar to that of typical binary fluids. At $\Gamma_{\mathrm{AB}}\sigma \simeq k_{\mathrm{B}}T$ ($\varepsilon_{\mathrm{AB}} = 2$), the domain boundary undergoes large fluctuation and a few (type A or B) particles leave their domain to dissolve in the other domain. As $\varepsilon_{\mathrm{AB}}$ decreases further, the domain breaks up into small domains, and finally the two types of particles are completely mixed.

On the other hand, the anchored polymers induce formation of small stable domains (called microdomains) instead of a mixing state, although it can reduce the line tension to $\Gamma_{\mathrm{AB}}\sigma \lesssim k_{\mathrm{B}}T$ (see Fig. 7.3(g)). At $\phi \leq 0.45$, the type A domain remains as one domain but exhibits an elongated shape at $\phi = 0.45$. At $\phi \geq 0.5$, it starts separating into microdomains. Note that the membrane is considered in a mixed state even at $\phi = 0.45$, if Γ_{AB} for the straight boundary is extrapolated (see Fig. 7.2).

In contrast to the reduction in $\varepsilon_{\mathrm{AB}}$, the boundary of the elongated domain is rather smooth (compare snapshots in Figs. 7.3(c) and (f)). We confirmed that these small domains are also formed from random distribution of initial states. Thus, it is a thermodynamically stable state [47].

Let us discuss the effects of the polymer anchoring on the domain formation. First, we remind that the polymer beads have only repulsive interactions with the other beads and membrane particles except for the membrane-anchored head particles.

The polymer effects seem suppressed for shorter lengths than the polymer size $\sim R_{\mathrm{end}} = 4\sigma$. A smaller boundary undulation than the polymer size does not yield additional space for the polymer brush. A similar suppression in the short length scale was reported on the bending rigidity induced by the polymer anchoring [27]. When the domain size is comparable to the polymer length, most of the particles already stay at the domain boundary, so that an additional increase in the boundary length likely yields much less gain in the average volume per polymer and the polymer conformational entropy. As explained in Sec. 7.1, the line tension of the circular domain is larger than the straight boundary. For the smaller domains, this difference would be enhanced, although the domains are too small for direct estimation of Γ_{AB} by Laplace's law.

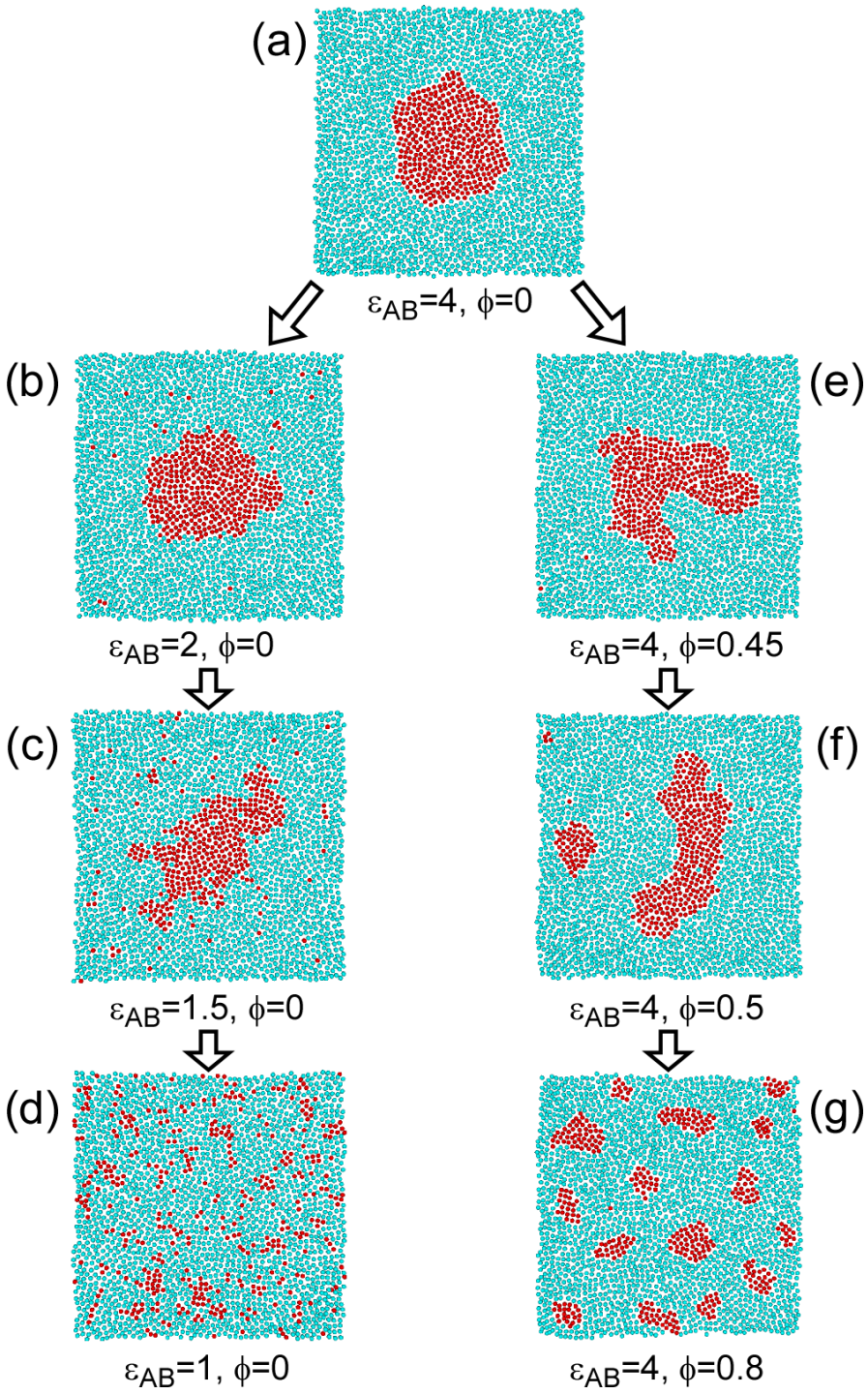

FIGURE 7.3: Sequential snapshots of two-component membranes as (left from (a) to (d)) ε_{AB} increases at $\phi = 0$ or (right from (a) to (g)) polymer density ϕ increases at $\varepsilon_{AB} = 4$. Red and blue particles represent the types of A and B membrane particles, respectively. To observe microdomain separation and shape transformation clearly, polymer particles are not displayed. Reproduced from Ref. [47] with permission of The Royal Society of Chemistry.

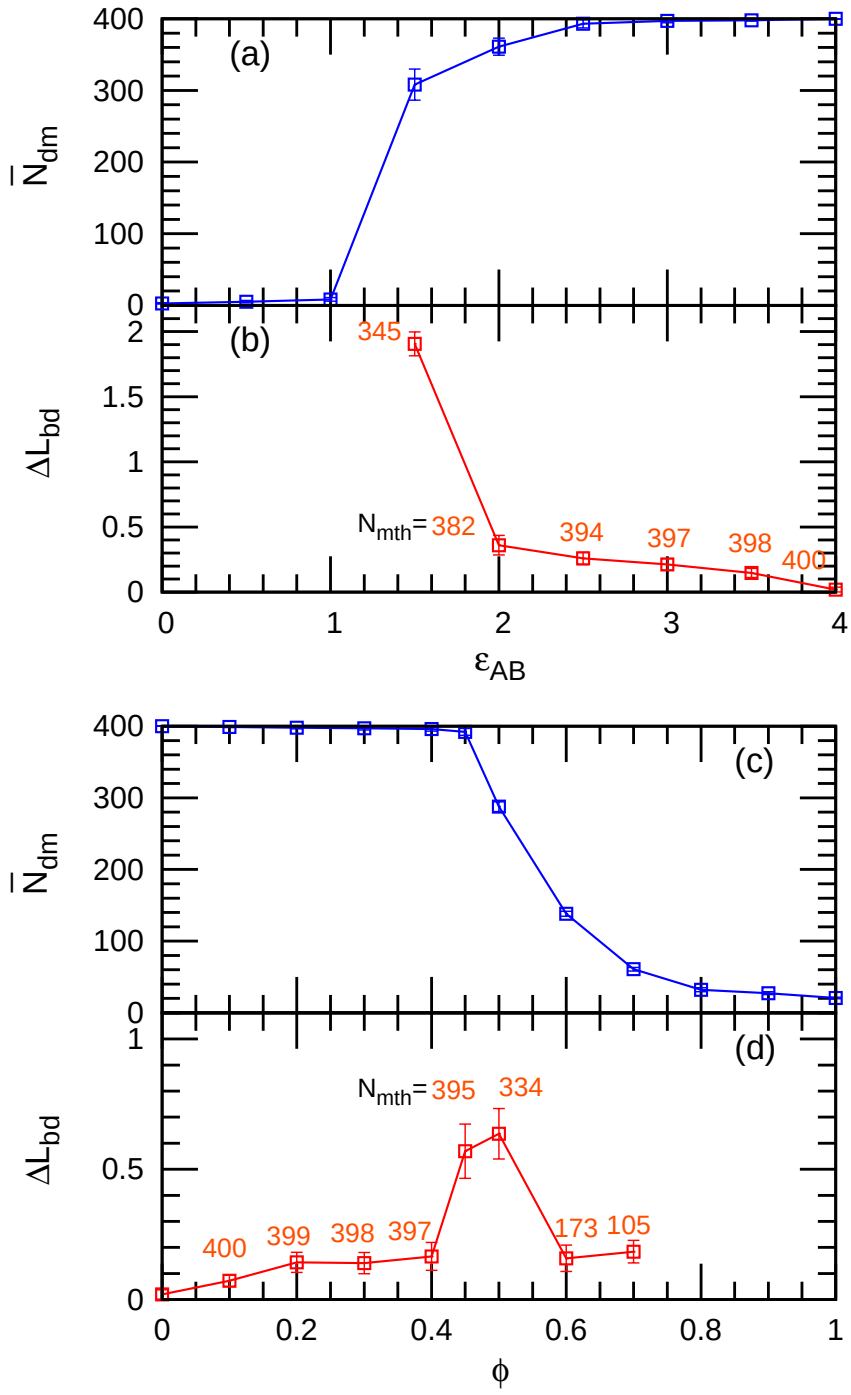

FIGURE 7.4: Domain shape changes and domain separation as (a,b) ε_{AB} decreases at $\phi = 0$ and (c,d) ϕ increases at $\varepsilon_{AB} = 4$. (a,c) The average cluster size $\bar{N}_{dm}$ of the mother (largest) domains and (b,d) the reduced excess domain length ΔL_{bd} of the mother domains. The mean number N_{mth} of the membrane particles in the mother domains at each stage is shown in light red color. Reproduced from Ref. [47] with permission of The Royal Society of Chemistry.

To investigate the changes of domains in greater detail, we calculate the mean cluster size $\bar{N}_{\rm dm}$ and a reduced excess domain length $\Delta L_{\rm bd}$. The cluster size $\bar{N}_{\rm dm}$ is defined as

$$\bar{N}_{\rm dm} = \frac{\sum_{i_{\rm c}=1}^{N_{\rm A}} n_i i_{\rm c}^2}{\sum_{i_{\rm c}=1}^{N_{\rm A}} n_i i_{\rm c}}, \tag{7.5}$$

where n_i is the number of clusters with size $i_{\rm c}$. The reduced excess domain length for the mother (largest) domains $\Delta L_{\rm bd}$ is defined as

$$\Delta L_{\rm bd} = \frac{L_{\rm bd}}{2\sqrt{\pi A_{\rm dm}}} - 1, \tag{7.6}$$

where $L_{\rm bd} = N_{\rm bd}\sqrt{a_0}$ is the boundary length of the mother domains and $A_{\rm dm} = N_{\rm A} a_0$ is the domain area. The length $L_{\rm bd}$ is normalized by the length of a circular domain $2\sqrt{\pi A_{\rm dm}}$ so that $\Delta L_{\rm bd} = 0$ for the circular domain.

Figure 7.4 shows the development of $\bar{N}_{\rm dm}$ and $\Delta L_{\rm bd}$. In the $\varepsilon_{\rm AB}$ reduction, the transition to the mixing state occurs sharply between $\varepsilon_{\rm AB} = 1.5$ and 1. However, for polymer grafting, a gradual decrease in $\bar{N}_{\rm dm}$ represents the formation of microdomains (see Fig. 7.4(c)). Around the transition points, $\Delta L_{\rm bd}$ is increased less by polymer grafting than by lowering $\varepsilon_{\rm AB}$, while both domains are similarly elongated (see Fig. 7.3). This difference is caused by the weaker undulation of polymer-anchored domain boundaries.

We calculated the fraction of polymer chain anchors on the mother domain $\phi_{\rm mth}$ after the microdomain separation (see Fig. 7.5). Interestingly, it is lower than the initial density ϕ. Thus, detached small domains have higher polymer densities than their mother domain. This is caused thermodynamically by the entropy gain of polymers anchored on small domains and also kinetically by a higher density at the domain boundary.

7.3 Summary for multi-component biomembrane patch

In this chapter, we applied binary fluid membranes with anchored polymers to measure interfacial line tension between two coexisting domains by simulation for the first time. We explored effects of polymer density on interfacial line tension of multi-component membranes. We found that interfacial tension between two domains can be reduced by anchoring polymers, and the domain separation occurs when the interfacial tension reduced by anchored polymer density reaches roughly less than $1k_{\rm B}T$, and the boundary length dramatically increases. The domain with the interfacial tension reduced by anchored polymer density has a smoother boundary profile compared with the one reduced by the affinity reduction potential. Two different routes of phase transitions are found

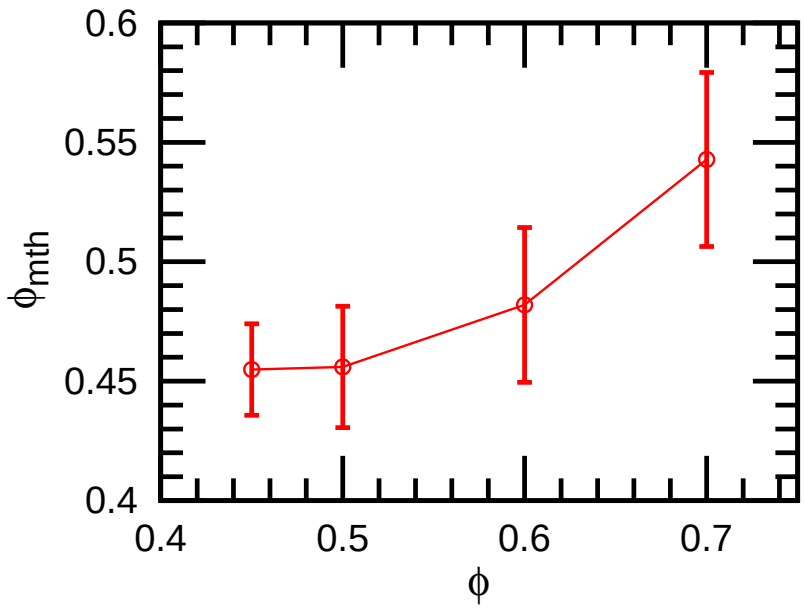

FIGURE 7.5: Mean polymer density ϕ dependence of the number fraction ϕ_{mth} of polymer chain anchors on the mother (largest) domain. Reproduced from Ref. [47] with permission of The Royal Society of Chemistry.

for the cases with/without anchored polymers. It implies that densely anchored polymers can stabilize microdomains to a small size. Our simulation results well reproduced a recent experiment observations on PEG-chain-anchored lipid membranes [20].

However, there is a difference between our simulation and their experimental condition. Since they used DOPC/DPPC/Chol as membrane substrates in the experiment [20], the affinity of DPPC lipids with Chol is weaker than some other saturated lipids, such as eSM [72]. It leads that DOPC lipids can also combine a part of lipids. While PEG chains only can anchor lipids by combining cholesterol first. So it is inevitable that some PEG chains also anchored onto DOPC lipids besides DPPC lipids. But since saturated lipids have stronger affinity to combine cholesterol compared with unsaturated lipids [8, 10, 72–74, 131], thus, for simplicity we can assume that all the cholesterol only combine saturated lipids so that polymer chains are only anchored onto saturated lipids in our simulation. Then we found the similar microdomain separation phenomena observed in their experiment [20]. It implied that only a nonuniform distribution of polymers anchored onto saturated and unsaturated lipids can induce such micro-segregation phenomena.

Chapter 8

Summary and Perspectives

8.1 Summary

We have systematically studied the entropic effects of anchored polymers on various types of mechanical and interfacial properties of biomembranes using particle-based membrane simulations. First, we reconfirm the previous theoretical predictions for spontaneous curvature and bending rigidity by simulating cylindrical membranes. They increase with the anchored polymer density ϕ linearly in the mushroom region, but sharply increase in the brush region.

Second, we investigated the polymer anchoring effects on the line tension of membrane edges for ideal and excluded-volume chains. It is revealed that polymer anchoring significantly reduces the line tension. For ideal polymer chains, it is also investigated by a mean field theory. It is clarified that the entropy gain of polymer conformation at the membrane edge reduces the line tension. Experimentally, it is known that polymer anchoring induces the formation of large vesicles [39] and spherical or discoidal micelles [40]. Since the ratio between the line tension and the bending rigidity determines the vesicle radius $R_{\rm ves}$ formed by the membrane disks as $R_{\rm ves} \sim (2\kappa + \bar{\kappa})/\Gamma_{\rm ed}$, the reduction in the line tension increases the vesicle radius. Our results are consistent with these experimental observations.

Finally, we investigated the polymer anchoring effects on two-component membranes for excluded-volume chains. The line tension of the domain boundary is reduced by anchoring polymers. It is found that densely anchored polymers can stabilize microdomains, whereas large domains are unstable. Although we did not investigate polymer length dependence here, it is expected that the domain size can be controlled by the polymer length. In living cells, lipid rafts contain a large amount of glycosphingolipids [4–7].

Our simulation results suggest that the entropic effects of glycosphingolipids may play a significant role in stabilizing microdomains $\lesssim$ 100 nm. At a moderate polymer density, elongated shapes of membrane domains are obtained. In lipid membranes with PEG-conjugated cholesterol, the domain shapes depend on the anchored polymer density ϕ_{PEG}: at a high ϕ_{PEG}, small domains are scattered, while at a slightly lower ϕ_{PEG}, small elongated domains are connected with each other to form a network [20]. The elongated domains in our simulations may form a network, if much larger domains are simulated. Further study is needed to clarify the polymer-anchoring effects on large-scale domain patterns.

Our present study highlights entropic effects of anchored polymers on the microdomain formation via the reduction in domain boundary tension on quasi-2D biomembranes. It is well known that high line tension can induce budding of membranes. Nonzero spontaneous curvature induced by proteins and anchored polymers can lead to various liposome shapes, such as tube formation and pearling [132–137]. Shape transformation of vesicles induced by polymer-anchored domains is an interesting topic for further studies.

8.2 Perspectives

This thesis provides the quantitative results of various mechanical properties of biomembranes dependent on anchored polymer density. It may be helpful to measure polymer-density-dependent properties of biomembranes. Furthermore, our work shows that binary phase separation with anchored polymers is quite different from the conventional binary phase separation, which can be explained by 2D Ising universality class, because separated microdomains can be finally stabilized in a small size instead of an indistinguishable random mixing. Such polymer-induced phase separation is not related to critical fluctuation, so the microdomain size cannot be explained by the correlation length of critical fluctuation. This provides a possible explanation why in vivo lipid rafts are stable in the range of size about 10 100 nm from the physical viewpoint.

From the biochemical experiments, we know that cholesterol prefer combining with saturated lipids, such as eSM, PSM, and DPPC, rather than unsaturated lipids, such as DOPC and SOPC [8, 10, 14, 20, 72–75, 84, 131]. Compared with ternary membranes composed of DPPC, DOPC, and cholesterol, in the ternary membranes composed of eSM, DOPC, and cholesterol eSM composition have a stronger affinity to hold all the cholesterol composition, as shown in Fig. 8.1. While DPPC composition only can hold most of the cholesterol composition, there is still a part of cholesterol composition combing with DOPC molecules. Thus, we suggest that membrane experimentalists apply a ternary membranes composed of eSM, DOPC and cholesterol with PEG-chol molecules

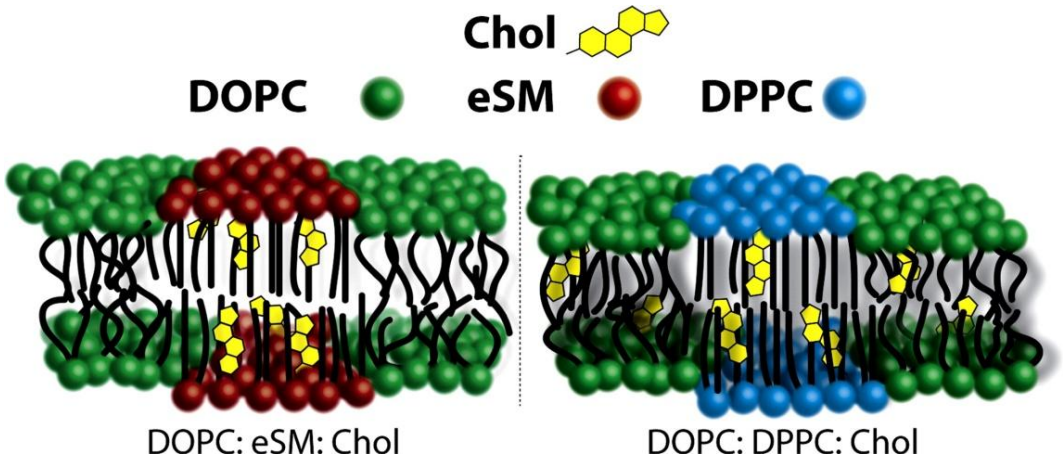

FIGURE 8.1: A schematic picture shows that different affinities in two types of ternary component membranes composed of DOPC/eSM/Chol and DOPC/DPPC/Chol, respectively. Reprinted with permission from Ref. [72].

to do new experiments so that they can prepare well-defined ternary membranes with anchored PEG chains exactly anchored to saturated lipids, such as eSM. This kind of experimental condition might fit to our simulation condition better so that this thesis work can be hopefully verified by such experiments in the near future. Or the experimentalists also may adopt other methods to enforce PEG-Chol molecules only combined with saturated lipids, such as DPPC, eSM, or PSM, in ternary membranes to verify and reproduce our simulation results.

After studying interesting phenomena in the 2D flat multi-component membrane patch, we further hope to extend our study to the 3D case for multi-component vesicles. We hope to understand how the anchored polymers will globally affect the domain pattern on the 3D vesicle and what are the new phenomena there. Does the spherical curvature affect the domain pattern? Are there some different domain shapes from the ones on the 2D planar membrane case by the geometric constraints? What are the preferred shapes of multi-component vesicles with anchored polymers? To clarify such problems, we construct a multi-component vesicle with anchored polymers, which is shown in Fig. 8.2.

Additionally cell membranes are always surrounded by various body fluids, such as blood, lymph, and sap, in real in vivo environment, and almost all the physiological activities cannot be executed without the fluids in the body. We are studying what is the new phenomena when the fluidic effects are considered. Our model can be easy to combine various hydrodynamics simulation methods, such as Dissipative Particle Dynamics [138–142], Multi-Particle Collision Dynamics (also called Stochastic Rotation

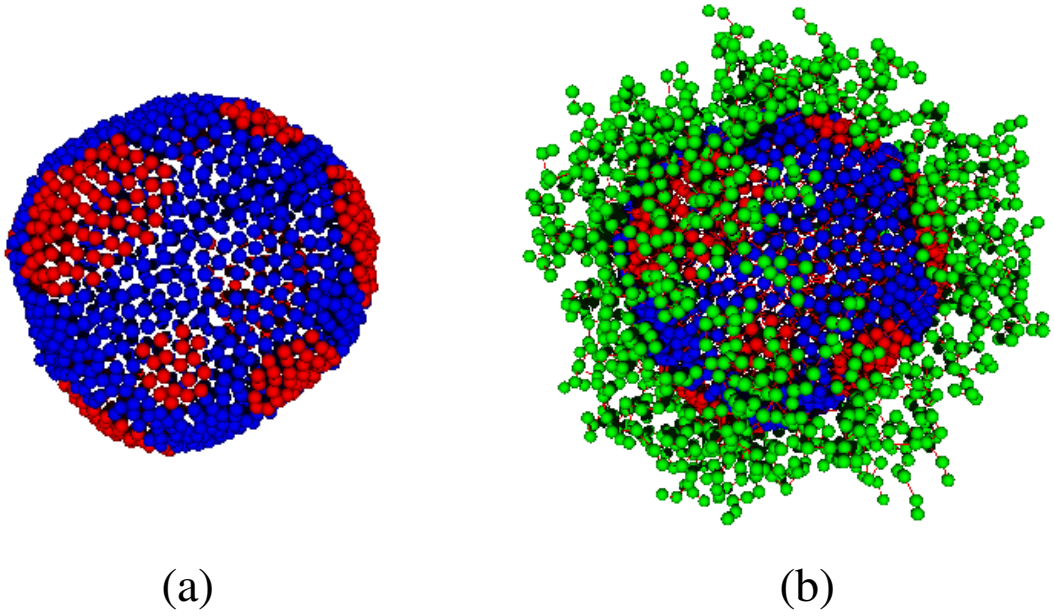

FIGURE 8.2: A snapshot shows that microdomain separation occurs in a 3D multi-component vesicle with anchored polymers.

Dynamics) [143–147] and so on. It is also a fantastic direction of biomembranes worthy to explore in the future.

Our current model may be extended to explain the concept "lipid raft", mainly composed of sphingolipids and sterols, proposed by Simons and his coworkers on the heterogeneity of cell membranes [2]. The presence of lipid rafts has been validated and confirmed by a lot of laboratories. Although many hypotheses have been proposed for the physiological function of these lipid microdomains, the detailed mechanism remains to be further clarified. Some ideas are difficult to be conducted in the experiments, because lipid rafts are too small to be observed by the optic microscopy, and also difficult to be prepared and purified. Some research groups attempted to adopt single-molecule techniques to explore lipid microdomains in the nanoscale world. We may apply theory and simulation to assist the relative researches. We are currently trying to take the first step.

There are many signaling molecules on the scaffold of lipid rafts, ones hope to know the relation among these signaling molecules, as well as whether these signaling molecules and the lipid components involved in signal transduction presented in l_o phase can perform best during phase separation. These promising questions are worthy to be seriously thought about. The issues on signal transduction involve nonlinear dynamics and statistical physics, so this is actually a highly interdisciplinary research field. To investigate lipid rafts, ones not only hope to understand its structure, it is more important to find their important functions in the physiological activities in cells.

Appendix A

Details of Scaling Theory Calculation

In this appendix, we show the details for the scaling theory calculation for the polymer brush regions on the flat surface, the spherical surface, and the cylindrical surface, respectively.

In the case of polymer brush on the flat surface, we assumed that it is the limit case of the spherical surface with an infinite radius. According to Sec. 3.4.3, ones have

$$\begin{aligned} N &= \int_R^{R+h_0} dr N_1 \frac{1}{\xi_0} \\ &= h_0 \left(\frac{\xi_0}{b}\right)^{1/\nu} \frac{1}{\xi_0} \\ &= h_0 b^{-1} \Gamma^{(\nu-1)/2\nu} \end{aligned} \tag{A.1}$$

Thus, we easily obtain the result (3.38).

For a sphere of radius R, we have

$$\begin{aligned} N &= \int_R^{R+h_s} dr N_1 \frac{1}{\xi_s(r)} \\ &= \int_R^{R+h_s} dr \left(\frac{\xi_s(r)}{b}\right)^{1/\nu} \frac{1}{\xi_s(r)} \\ &= \int_R^{R+h_s} dr b^{-1/\nu} \left(\frac{\xi_0 r}{R}\right)^{(1-\nu)/\nu} \\ &= b^{-1/\nu} \left(\frac{\xi_0}{R}\right)^{(1-\nu)/\nu} \left[\nu \left(R+h_s\right)^{1/\nu} - \nu R^{1/\nu}\right] \\ &= \left(\frac{\xi_0}{b}\right)^{1/\nu} \frac{1}{\xi_0} (\nu R) \left[\left(1+\frac{h_s}{R}\right)^{1/\nu} - 1\right] \end{aligned} \tag{A.2}$$

Combining with (3.37), it leads to the result (3.41).

Similar to the spherical surface, for a cylindrical surface of radius R, we have

$$\begin{aligned} N &= \int_R^{R+h_c} dr N_1 \frac{1}{\xi_c(r)} \\ &= \int_R^{R+h_c} dr \left(\frac{\xi_c(r)}{b}\right)^{1/\nu} \frac{1}{\xi_c(r)} \\ &= \int_R^{R+h_c} dr b^{-1/\nu} \left(\frac{\xi_0 r^{1/2}}{R^{1/2}}\right)^{(1-\nu)/\nu} \\ &= b^{-1/\nu} \left(\frac{\xi_0}{R^{1/2}}\right)^{(1-\nu)/\nu} \frac{2\nu}{1+\nu} \left[(R+h_c)^{(1+\nu)/2\nu} - R^{(1+\nu)/2\nu}\right] \\ &= \left(\frac{\xi_0}{b}\right)^{1/\nu} \frac{1}{\xi_0} \left(\frac{2\nu}{1+\nu} R\right) \left[\left(1+\frac{h_c}{R}\right)^{(1+\nu)/2\nu} - 1\right] \end{aligned} \tag{A.3}$$

Combining with (3.37), it leads to the result (3.44).

Next, we calculate three kinds of free energies per polymer on different types of surfaces. Combining with (3.36), the free energy per polymer on the flat surface can be easily obtained as

$$\begin{aligned} F_0 &= k_B T \int_R^{R+h_0} dr \frac{1}{\xi_0} \\ &= k_B T h_0 \frac{1}{\xi_0} \\ &= k_B T \Gamma^{1/2} h_0 / b \end{aligned} \tag{A.4}$$

which is just the result (3.46) for the flat surface.

In the case of a sphere of radius R, the free energy per polymer on the flat surface is

$$\begin{aligned} F_s &= k_B T \int_R^{R+h_s} dr \frac{1}{\xi_s(r)} \\ &= k_B T \int_R^{R+h_s} dr \frac{R}{\xi_0 r} \\ &= k_B T \frac{R}{\xi_0} \left\{ \ln \left[R \left(1 + \frac{h_0}{\nu R}\right)^{\nu} \right] - \ln R \right\} \\ &= \left(\frac{k_B T \Gamma^{1/2} R \nu}{b}\right) \ln \left(1 + \frac{h_0}{\nu R}\right) \end{aligned} \tag{A.5}$$

Thus, the result (3.47) for the spherical surface case is also obtained.

Similar to the spherical surface, for a cylinder of radius R, we have

$$\begin{aligned} F_{\mathrm{c}} &= k_{\mathrm{B}}T\int_{R}^{R+h_{\mathrm{c}}} dr\frac{1}{\xi_{\mathrm{c}}(r)} \\ &= k_{\mathrm{B}}T\int_{R}^{R+h_{\mathrm{c}}} dr\frac{R^{1/2}}{\xi_0 r^{1/2}} \\ &= 2k_{\mathrm{B}}T\frac{R^{1/2}}{\xi_0}\left\{\left[R\left(1+\frac{(1+\nu)h_0}{2\nu R}\right)^{2\nu/(1+\nu)}\right]-R\right\} \\ &= \left(\frac{2k_{\mathrm{B}}T\Gamma^{1/2}R}{b}\right)\left[\left(1+\frac{(1+\nu)h_0}{2\nu R}\right)^{\nu/(1+\nu)}-1\right] \end{aligned} \tag{A.6}$$

which is exactly the same as the result (3.48) for the cylindrical surface.

The excess free energy of the polymer brush on the cylindrical surface is calculated as

$$\begin{aligned} \Delta F_{\mathrm{ex,c}} &= \Delta E_{\mathrm{b}} + \Delta F_{\mathrm{c}} \\ &= 2\kappa_0\Gamma^{-1}(bH)^2 + TN\Gamma^{1/2\nu}f_{\mathrm{c}}(x) \end{aligned} \tag{A.7}$$

with

$$f_{\mathrm{c}}(x) = \frac{1}{x}\left[\left(1+\frac{1+\nu}{\nu}x\right)^{\nu/(1+\nu)}-1\right]-1$$

where $x = h_0H$.

Let us minimize Eq. (A.7), that is, $\partial\Delta F_{\mathrm{ex,c}}/\partial H = 0$, we have

$$\begin{aligned} \frac{\partial\Delta F_{\mathrm{ex,c}}}{\partial H} &= 4\kappa_0\Gamma^{-1}b^2H + \frac{k_{\mathrm{B}}TN\Gamma^{1/2\nu}h_0^2}{b}\frac{\partial f_{\mathrm{c}}(x)}{\partial x} \\ &= 4\kappa_0\Gamma^{-1}bx + k_{\mathrm{B}}TN^3\Gamma^{(3-2\nu)/2\nu}b\frac{\partial f_{\mathrm{c}}(x)}{\partial x} \\ &= 0 \end{aligned} \tag{A.8}$$

Thus, we easily obtain Eq. (3.52).

To estimate the spontaneous curvature and the bending rigidity by using the cylindrical surface, an approximate second order expansion Eq. 3.54 can be substituted into Eq. (3.52). Then we have

$$-\frac{1}{2\nu}+\frac{\nu+2}{3\nu^2}x+\frac{4\kappa_0}{k_{\mathrm{B}}T}N^{-3}\Gamma^{-3/2\nu}x = 0 \tag{A.9}$$

So we obtain a small curvature expansion expression for the cylindrical surface as

$$h_0c_0 = \frac{1}{2\nu}\left[\frac{\nu+2}{3\nu^2}+\frac{4\kappa_0}{k_{\mathrm{B}}T}N^{-3}\Gamma^{-3/2\nu}\right]^{-1} \tag{A.10}$$

Because ones know $H = 1/R$ and $K = 1/R^2$ for the spherical surface, but $H = 1/2R$ and $K = 0$ the cylindrical surface, we can rewrite Eq. (3.53) as

$$\Delta F_{\mathrm{s}} = F_0 \left[-\frac{1}{2\nu}(h_0 H) + \frac{\nu+2}{6\nu^2}(h_0 H)^2 - \frac{1}{6\nu}(h_0 H)^2 + \mathcal{O}\left((h_0 H)^3\right) \right] \tag{A.11}$$

By comparing Eqs. (A.11) and (3.54), we obtain a second order curvature expansion of the excess free energy for a general surface

$$\Delta F_{\mathrm{surf}}(H, K) = F_0 \left[-\frac{1}{2\nu}(h_0 H) + \frac{\nu+2}{6\nu^2}(h_0 H)^2 - \frac{1}{6\nu} h_0^2 K \right] \tag{A.12}$$

By using Eq. (3.38), we can compare the corresponding terms between Eq. (3.51) and (A.12) to obtain the polymer-induced bending rigidities:

$$\Delta\kappa = \frac{\nu+2}{12\nu^2} N^3 \Gamma^{3/2\nu} k_{\mathrm{B}} T \tag{A.13}$$

and

$$\Delta\bar{\kappa} = -\frac{1}{6\nu^2} N^3 \Gamma^{3/2\nu} k_{\mathrm{B}} T \tag{A.14}$$

Again, by using Eq. (3.38), Eq. (A.10) can be written as

$$bN\Gamma^{(1-\nu)/2\nu} c_0 = \frac{1}{2\nu} \left[\frac{\nu+2}{3\nu^2} x + \frac{4\kappa_0}{k_{\mathrm{B}} T} N^{-3} \Gamma^{-3/2\nu} x \right]^{-1} \tag{A.15}$$

Thus, we obtain

$$\begin{aligned} bc_0 &= \frac{1}{2\nu} \left[\frac{\nu+2}{3\nu^2} N\Gamma^{(1-\nu)/2\nu} + \frac{4\kappa_0}{k_{\mathrm{B}} T} N^{-2} \Gamma^{-(\nu+2)/2\nu} \right]^{-1} \\ &= \frac{1}{8\nu} \left[\frac{\nu+2}{12\nu^2} N\Gamma^{(1-\nu)/2\nu} + \frac{\kappa_0}{k_{\mathrm{B}} T} N^{-2} \Gamma^{-(\nu+2)/2\nu} \right]^{-1} \\ &= \frac{1}{8\nu} N^2 \Gamma^{(\nu+2)/2\nu} \frac{k_{\mathrm{B}} T}{\kappa_{\mathrm{eff}}} \end{aligned} \tag{A.16}$$

The last result is obtained by using Eq. (3.55).

Appendix B

Details of Mean Field Theory Calculation

Because n_1 is a small area part, about 5%, compared to the whole membrane strip, we should execute Taylor expansion in terms of it. Let $A = 1 + (Q-1)\phi$, $B = (Q-1)n_1/[1+(Q-1)\phi]$, and $C = 4Q(Q-1)\phi n_1$, then we have

$$\begin{aligned}
\phi_1 &= \frac{2Q\phi}{s + \sqrt{s^2 - 4Q(Q-1)\phi n_1}} \qquad \text{(B.1)} \\
&= \frac{2Q\phi}{A(1+B)[1+\sqrt{1-C/A^2(1+B)^2}]} \\
&= \frac{Q\phi(1-B)}{A[1-C/4A^2(1+B)^2]} + \mathcal{O}\left(n_1^2\right) \\
&= \frac{Q\phi}{A}(1-B)\left[1 + \frac{C}{4A^2(1+B)^2}\right] + \mathcal{O}\left(n_1^2\right) \\
&= \frac{Q\phi}{A}(1-B)\left[1 + \frac{C(1-B)^2}{4A^2}\right] + \mathcal{O}\left(n_1^2\right) \\
&= \frac{Q\phi}{1+(Q-1)\phi}\left[1 - \frac{(Q-1)n_1}{1+(Q-1)\phi}\right]\left(1 - \frac{Q(Q-1)\phi n_1(1-2B)}{[1+(Q-1)\phi]^2}\right) + \mathcal{O}\left(n_1^2\right) \\
&= \frac{Q\phi}{1+(Q-1)\phi}\left(1 - \frac{(Q-1)n_1}{1+(Q-1)\phi} - \frac{Q(Q-1)\phi n_1}{[1+(Q-1)\phi]^2}\right) + \mathcal{O}\left(n_1^2\right) \\
&= \frac{Q\phi}{1+(Q-1)\phi}\left(1 - \frac{(Q-1)(1-\phi)}{\{1+(Q-1)\phi\}^2}n_1\right) + \mathcal{O}\left(n_1^2\right)
\end{aligned}$$

where $s = 1 + (Q-1)(\phi + n_1)$.

Appendix C

Standard Virial Calculation of Pressure in Molecular Dynamics

The usual virial approach to the estimation of the macroscopic pressure P in many standard molecular simulations involves an ensemble average of the instantaneous or microscopic pressure p [112, 148]. For a simulation box containing N particles with a volume V, ones can express the microscopic pressure p as [112]

$$p = \frac{1}{V}\left(\frac{1}{3}\sum_i m_i \mathbf{v}_i^2 + \frac{1}{3}\sum_i \mathbf{r}_i \cdot \mathbf{f}_i\right) \tag{C.1}$$

$$\mathbf{f}_i = -\frac{\partial U}{\partial \mathbf{r}_i} \tag{C.2}$$

where m_i is the mass, $\mathbf{r}_i$ and $\mathbf{v}_i$ is the position vector and the velocity vector of particle i, and $\mathbf{f}_i$ is the force applied on particle i. When external fields vanish, only the intermolecular interactions make the contribution to the forces. The macroscopic pressure P can be easily obtained by the averaging procedure $P = \langle p \rangle$, where the angular brackets means either a time average or an ensemble average. For any system with pairwise interactions, the pressure can be written explicitly in the usual virial form as

$$P = \left\langle \frac{1}{V}\left(\frac{1}{3}\sum_i m_i \mathbf{v}_i^2 + \frac{1}{3}\sum_i \mathbf{r}_i \cdot \mathbf{f}_i\right)\right\rangle \tag{C.3}$$

where $\rho = N/V$ is the particle number density, k_{B} is the Boltzmann constant, T is the temperature. The first term on the right side of Eq. (C.3) is the kinetic (ideal gas) contribution, while the second term, also called as 'internal virial' [112], represents the contribution from the intermolecular interactions.

For the convenience of MD simulation, the internal virial for pressure tensors, the second term in Eq. (C.3), can be algorithmized as

$$\begin{aligned}
\sum_i \mathbf{r}_i \cdot \mathbf{f}_i &= \sum_i \sum_{j \neq i} \mathbf{r}_i \cdot \mathbf{f}_{ij} \\
&= \frac{1}{2} \sum_i \sum_{j \neq i} (\mathbf{r}_i \cdot \mathbf{f}_{ij} + \mathbf{r}_j \cdot \mathbf{f}_{ji}) \\
&= \frac{1}{2} \sum_i \sum_{j \neq i} (\mathbf{r}_i \cdot \mathbf{f}_{ij} - \mathbf{r}_j \cdot \mathbf{f}_{ij}) \\
&= \frac{1}{2} \sum_i \sum_{j \neq i} \mathbf{r}_{ij} \cdot \mathbf{f}_{ij} \\
&= \sum_i \sum_{j > i} \mathbf{r}_{ij} \cdot \mathbf{f}_{ij}
\end{aligned} \tag{C.4}$$

Thus, the component form of Eq. (C.4) can be written as

$$\sum_i \alpha_i f_i^\alpha = \sum_i \sum_{j > i} \alpha_{ij} f_{ij}^\alpha \tag{C.5}$$

where $f_i^\alpha = -\partial U / \partial \alpha_i$, $f_{ij}^\alpha = -\partial U_j / \partial \alpha_i$, and α represents x, y, or z. Thus, we obtain Eq. (5.5) in Section 5.1.

This calculation way of the pressure is widely applied and well suited to various MD simulations, for which the molecular trajectories are determined by the evaluation of the forces [112, 148].

Bibliography

[1] S. J. Singer and G. L. Nicolson. The fluid mosaic model of the structure of cell membranes. *Science*, 175(23):720–731, 1972.

[2] K. Simons and E. Ikonen. Functional rafts in cell membranes. *Nature*, 387(6633): 569, 1997.

[3] E. Ikonen. Roles of lipid rafts in membrane transport. *Curr. Opin. Cell Biol.*, 13 (4):470–477, 2001.

[4] G. Vereb, J. Szöllősi, J. Matko, P. Nagy, T. Farkas, L. Vigh, L. Matyus, T. A. Waldmann, and S. Damjanovich. Dynamic, yet structured: the cell membrane three decades after the singer–nicolson model. *Proc. Natl. Acad. Sci. USA*, 100 (14):8053–8058, 2003.

[5] S. Thomas, R. S. Kumar, and T.-D. Brumeanu. Role of lipid rafts in t cells. *Arch. Immunol. Ther. Exp.*, 52(4):215, 2004.

[6] Z. Korade and A. K. Kenworthy. Lipid rafts, cholesterol, and the brain. *Neuropharmacology*, 55(8):1265–1273, 2008.

[7] L. J. Pike. The challenge of lipid rafts. *J. Lipid Res.*, 50(Supplement):S323–S328, 2009.

[8] A. R. Honerkamp-Smith, S. L. Veatch, and S. L. Keller. An introduction to critical points for biophysicists; observations of compositional heterogeneity in lipid membranes. *Biochim. Biophys. Acta*, 1788:53–63, 2009.

[9] L. Bagatolli and P. B. Sunil Kumar. Phase behavior of multicomponent membrans: Experimental and computational techniques. *Soft Matter*, 5:3234–3248, 2009.

[10] S. L. Veatch and S. L. Keller. Organization in lipid membranes containing cholesterol. *Phys. Rev. Lett.*, 89(26):268101, 2002.

[11] T. Baumgart, S. T. Hess, and W. W. Webb. Imaging coexisting fluid domains in biomembrane models coupling curvature and line tension. *Nature*, 425(6960): 821–824, 2003.

[12] A. T. Hammond, F. A. Heberle, T. Baumgart, D. Holowka, B. Baird, and G. W. Feigenson. Crosslinking a lipid raft component triggers liquid ordered-liquid disordered phase separation in model plasma membranes. *Proc. Natl. Acad. Sci. USA*, 102(18):6320–6325, 2005.

[13] P. I. Kuzmin, S. A. Akimov, Y. A. Chizmadzhev, J. Zimmerberg, and F. S. Cohen. Line tension and interaction energies of membrane rafts calculated from lipid splay and tilt. *Biophys. J.*, 88(2):1120–1133, 2005.

[14] M. Yanagisawa, M. Imai, and T. Taniguchi. Shape deformation of ternary vesicles coupled with phase separation. *Phys. Rev. Lett.*, 100:148102, 2008.

[15] G. G. Putzel and M. Schick. Theory of raft formation by the cross-linking of saturated or unsaturated lipids in model lipid bilayers. *Biophys. J.*, 96(12):4935–4940, 2009.

[16] H. M. McConnell and V. T. Moy. Shapes of finite two-dimensional lipid domains. *J. Phys. Chem.*, 92:4520–4525, 1988.

[17] H. Wu and Z. C. Tu. Theoretical and numerical investigations on shapes of planar lipid monolayer domains. *J. Chem. Phys.*, 130:045103, 2009.

[18] M. Iwamoto, F. Liu, and Z.-C. Ou-Yang. Domain shapes in lipid monolayers studied as polar cholesteric liquid crystals. *Europhys. Lett.*, 91:16004, 2010.

[19] L. J. Pike. Rafts defined: a report on the keystone symposium on lipid rafts and cell function. *J. lipid Res.*, 47(7):1597–1598, 2006.

[20] M. Yanagisawa, N. Shimokawa, M. Ichikawa, and K. Yoshikawa. Micro-segregation induced by bulky-head lipids: formation of characteristic patterns in a giant vesicle. *Soft Matter*, 8(2):488–495, 2012. doi: 10.1039/C1SM06381B.

[21] D. Marsh, R. Bartucci, and L. Sportelli. Lipid membranes with grafted polymers: physicochemical aspects. *Biochim. Biophys. Acta*, 1615(1):33–59, 2003.

[22] S. T. Milner and T. A. Witten. Bending moduli of polymeric surfactant interfaces. *J. Phys.*, 49(11):1951–1962, 1988.

[23] R. Lipowsky. Bending of membranes by anchored polymers. *Europhys. Lett.*, 30 (4):197, 1995.

[24] C. Hiergeist and R. Lipowsky. Elastic properties of polymer-decorated membranes. *J. Phys. II France*, 6(10):1465–1481, 1996.

[25] H.-G. Döbereiner, O. Selchow, and R. Lipowsky. Spontaneous curvature of fluid vesicles induced by trans-bilayer sugar asymmetry. *Euro. Biophys. J.*, 28(2):174–178, 1999.

[26] T. Auth and G. Gompper. Self-avoiding linear and star polymers anchored to membranes. *Phys. Rev. E*, 68(5):051801, 2003.

[27] T. Auth and G. Gompper. Fluctuation spectrum of membranes with anchored linear and star polymers. *Phys. Rev. E*, 72(3):031904, 2005.

[28] M. Werner and J.-U. Sommer. Polymer-decorated tethered membranes under good- and poor-solvent conditions. *Eur. Phys. J. E*, 31:383–392, 2010.

[29] E. Evans and W. Rawicz. Elasticity of"fuzzy"biomembranes. *Phys. Rev. Lett.*, 79 (12):2379–2382, 1997.

[30] D. D. Lasic. Sterically stabillized vesicles. *Angew. Chem. Int. Ed. Engl.*, 33: 1685–1698, 1994.

[31] A. S. Hoffman. The origins and evolution of controlled drug delivery systems. *J. Control. Release*, 132(3):153–163, 2008.

[32] E. W. Kaler, A. K. Murthy, B. E. Rodriguez, and J. A. N. Zasadzinski. Spontaneous vesicle formation in aqueous mixtures of single-tailed surfactants. *Science*, 245:1371–1374, 1989.

[33] T. M. Weiss, T. Narayanan, C. Wolf, M. Gradzielski, P. Panine, S. Finet, and W. I. Helsby. Dynamics of the self-assembly of unilamellar vesicles. *Phys. Rev. Lett.*, 94:038303, 2005.

[34] J. Leng, S. U. Egelhaaf, and M. E. Cates. Kinetic pathway of spontaneous vesicle formation. *Europhys. Lett.*, 59:311–317, 2002.

[35] D. Madenci, A. Salonen, P. Schurtenberger, J. S. Pedersen, and S. U. Egelhaaf. Simple model for the growth behaviour of mixed lecithin-bile salt micelles. *Phys. Chem. Chem. Phys.*, 13:3171–3178, 2011.

[36] K. Bryskhe, S. Bulut, and U. Olsson. Vesicle formation from temperature jumps in a noionic surfactant system. *J. Phys. Chem. B*, 109:9265–9274, 2005.

[37] H. Noguchi and G. Gompper. Dynamics of vesicle self-assembly and dissolution. *J. Chem. Phys.*, 125:164908, 2006.

[38] H. Noguchi. Structure formation in binary mixtures of lipids and detergents: Self-assembly and vesicle division. *J. Chem. Phys.*, 138:024907, 2013.

[39] K. Bressel, M. Muthig, S. Prevost, J. Gummel, T. Narayanan, and M. Gradzielski. Shaping vesicles-controlling size and stability by admixture of amphiphilic copolymer. *ACS Nano*, 6:5858–5865, 2012.

[40] M. Johnsson and K. Edwards. Liposomes, disks, and spherical micelles: Aggregate structure in mixtures of gel phase phosphatidylcholines and poly(ethylene glycol)-phospholipids. *Biophys. J.*, 85:3839–3847, 2003.

[41] A. Schalchli-Plaszczynski and L. Auvray. Vesicle-to-micelle transition induced by grafted diblock copolymers. *Eur. Phys. J. E*, 7:339–344, 2002.

[42] H. Noguchi and G. Gompper. Meshless membrane model based on the moving least-squares method. *Phys. Rev. E*, 73(2):021903, 2006.

[43] H. Noguchi. Membrane simulation models from nm to um scale. *J. Phys. Soc. Jpn.*, 78(1):041007, 2009.

[44] S. A. Pandit, E. Jakobsson, and H. L. Scott. Simulation of the early stages of nano-domain formation in mixed bilayers of sphingomyelin, cholesterol, and dioleylphosphatidylcholine. *Biophys. J.*, 87(5):3312–3322, 2004.

[45] Hao Wu, Hayato Shiba, and Hiroshi Noguchi. Mechanical properties and microdomain separation of polymer-grafted fluid membranes. *arXiv preprint arXiv:1306.4271*, 2013.

[46] H. Wu and H. Noguchi. Effects of anchored flexible polymers on mechanical properties of model biomembranes. *AIP Conf. Proc.*, 1518:649–653, 2013.

[47] H. Wu, H. Shiba, and H. Noguchi. Mechanical properties and microdomain separation of fluid membranes with anchored polymers. *Soft Matter*, 2013. doi: 10.1039/C3SM51680F.

[48] J. Lewis M. Raff K. Roberts B. Alberts, A. Johnson and P. Walter. *Molecular Biology of the Cell, 4th ed.* New York: Garland Science Publishing, 2007.

[49] R. Lipowsky and E. Sackmann. *Structure and Dynamics of Membranes: I. From Cells to Vesicles/II. Generic and Specific Interactions*, volume 1. North Holland, 1995.

[50] S. F. Sui. *Molecular Biology of Membrances.* Higher Education Press, Beijing, 2003.

[51] F. R. Maxfield. Plasma membrane microdomains. *Curr. Opin. Cell Biol.*, 14(4): 483–487, 2002.

[52] M. Edidin. Lipids on the frontier: a century of cell-membrane bilayers. *Nat. Rev. Mol. Cell Biol.*, 4(5):414–418, 2003.

[53] D. Chiras. *Human Biology: Health, Homeostasis, and the Environment, 4th ed.* Jones and Bartlett Publishers, Boston, 2002.

[54] P. Nelson. *Biological Physics: Energy, Information, Life*. W.H. Freeman Company Publishing, 2004.

[55] C. J. Fielding. *Lipid Rafts and Caveolae : From Membrane Biophysics to Cell Biology*. Wiley-VCH, Weinheim, 2006.

[56] S. Thomas, A. Preda-Pais, S. Casares, and T.-D. Brumeanu. Analysis of lipid rafts in t cells. *Mol. Immunol.*, 41(4):399–409, 2004.

[57] J. F. Nagle and H. L. Scott. Biomembrane phase transitions. *Physics Today*, 31: 38, 1978.

[58] P. Uppamoochikkal, S. Tristram-Nagle, and J. F. Nagle. Orientation of tie-lines in the phase diagram of dopc/dppc/cholesterol model biomembranes. *Langmuir*, 26(22):17363–17368, 2010.

[59] S. Munro. Lipid rafts: elusive or illusive? *Cell*, 115(4):377–388, 2003.

[60] G. Garbès Putzel and M. Schick. Phenomenological model and phase behavior of saturated and unsaturated lipids and cholesterol. *Biophys. J.*, 95(10):4756–4762, 2008.

[61] A. Radhakrishnan and H. M. McConnell. Condensed complexes in vesicles containing cholesterol and phospholipids. *Proc. Natl. Acad. Sci. USA*, 102(36):12662–12666, 2005.

[62] P. F. F. Almeida. Thermodynamics of lipid interactions in complex bilayers. *Biochim. Biophys. Acta Biomembr.*, 1788(1):72–85, 2009.

[63] G. W. Feigenson. Phase behavior of lipid mixtures. *Nat. Chem. Biol.*, 2(11): 560–563, 2006.

[64] M. L. Frazier, J. R. Wright, A. Pokorny, and P. F. F. Almeida. Investigation of domain formation in sphingomyelin/cholesterol/popc mixtures by fluorescence resonance energy transfer and monte carlo simulations. *Biophys. J.*, 92(7):2422–2433, 2007.

[65] M. L. Berkowitz. Detailed molecular dynamics simulations of model biological membranes containing cholesterol. *Biochim. Biophys. Acta Biomembr.*, 1788(1): 86–96, 2009.

[66] S. J. Marrink, H. J. Risselada, S. Yefimov, D. P. Tieleman, and A. H. de Vries. The martini force field: coarse grained model for biomolecular simulations. *J. Phys. Chem. B*, 111(27):7812–7824, 2007.

[67] B. J. Reynwar, G. Illya, V. A. Harmandaris, M. M. Müller, K. Kremer, and M. Deserno. Aggregation and vesiculation of membrane proteins by curvature-mediated interactions. *Nature*, 447(7143):461–464, 2007.

[68] S. Izvekov and G. A. Voth. A multiscale coarse-graining method for biomolecular systems. *J. Phys. Chem. B*, 109(7):2469–2473, 2005.

[69] J. Huang and G. W. Feigenson. A microscopic interaction model of maximum solubility of cholesterol in lipid bilayers. *Biophys. J.*, 76(4):2142–2157, 1999.

[70] G. W. Feigenson. Phase boundaries and biological membranes. *Ann. Rev. Biophys. Biomol. Struct.*, 36:63, 2007.

[71] J. F. Nagle. Introductory lecture: Basic quantities in model biomembranes. *Faraday Discuss.*, 161:11–29, 2013. doi: 10.1039/C2FD20121F.

[72] K. J. Fritzsching, J. Kim, and G. P. Holland. Probing lipid–cholesterol interactions in dopc/esm/chol and dopc/dppc/chol model lipid rafts with dsc and 13c solid-state nmr. *Biochim. Biophys. Acta*, 1828(8):1889–1898, 2013.

[73] S. L. Veatch, I. V. Polozov, K. Gawrisch, and S. L. Keller. Liquid domains in vesicles investigated by nmr and fluorescence microscopy. *Biophys. J.*, 86(5):2910–2922, 2004.

[74] S. L. Veatch and S. L. Keller. Seeing spots: complex phase behavior in simple membranes. *Biochim. Biophys. Acta*, 1746(3):172–185, 2005.

[75] S. L. Veatch, O. Soubias, S. L. Keller, and K. Gawrisch. Critical fluctuations in domain-forming lipid mixtures. *Proc. Natl. Acad. Sci. USA*, 104(45):17650–17655, 2007.

[76] F. M. Goñi, A. Alonso, L. A. Bagatolli, R. E. Brown, D. Marsh, M. Prieto, and J. L. Thewalt. Phase diagrams of lipid mixtures relevant to the study of membrane rafts. *Biochim. Biophys. Acta*, 1781(11):665–684, 2008.

[77] J. Zhao, J. Wu, F. A. Heberle, T. T. Mills, P. Klawitter, G. Huang, G. Costanza, and G. W. Feigenson. Phase studies of model biomembranes: complex behavior of dspc/dopc/cholesterol. *Biochim. Biophys. Acta Biomembr.*, 1768(11):2764–2776, 2007.

[78] J. H. Davis, J. J. Clair, and J. Juhasz. Phase equilibria in dopc/dppc-d¡ sub¿ 62¡/sub¿/cholesterol mixtures. *Biophys. J.*, 96(2):521–539, 2009.

[79] A. K. Smith and J. H. Freed. Determination of tie-line fields for coexisting lipid phases: An esr study? *J. Phys. Chem. B*, 113(12):3957–3971, 2009.

[80] N. Bezlyepkina, R. S. Gracià, P. Shchelokovskyy, R. Lipowsky, and R. Dimova. Phase diagram and tie-line determination for the ternary mixture dopc/esm/cholesterol. *Biophys. J.*, 104(7):1456–1464, 2013.

[81] A. Parker, K. Miles, K. H. Cheng, and J. Huang. Lateral distribution of cholesterol in dioleoylphosphatidylcholine lipid bilayers: cholesterol-phospholipid interactions at high cholesterol limit. *Biophys. J.*, 86(3):1532–1544, 2004.

[82] A. R. Honerkamp-Smith, P. Cicuta, M. D. Collins, S. L. Veatch, M. den Nijs, M. Schick, and S. L. Keller. Line tensions, correlation lengths, and critical exponents in lipid membranes near critical points. *Biophys. J.*, 95(1):236–246, 2008.

[83] S. L. Veatch and S. L. Keller. Miscibility phase diagrams of giant vesicles containing sphingomyelin. *Phys. Rev. Lett.*, 94(14):148101, 2005.

[84] T. Portet, S. E. Gordon, and S. L. Keller. Increasing membrane tension decreases miscibility temperatures; an experimental demonstration via micropipette aspiration. *Biophys. J.*, 103(8):L35–L37, 2012.

[85] F. M. Thakkar and K. G. Ayappa. Effect of polymer grafting on the bilayer gel to liquid-crystalline transition. *J. Phys. Chem. B*, 114(8):2738–2748, 2010.

[86] S. Belsito, R. Bartucci, G. Montesano, D. Marsh, and L. Sportelli. Molecular and mesoscopic properties of hydrophilic polymer-grafted phospholipids mixed with phosphatidylcholine in aqueous dispersion: Interaction of dipalmitoyl n-poly (ethylene glycol) phosphatidylethanolamine with dipalmitoylphosphatidylcholine studied by spectrophotometry and spin-label electron spin resonance. *Biophys. J.*, 78(3):1420–1430, 2000.

[87] D. Marsh. Elastic constants of polymer-grafted lipid membranes. *Biophys. J.*, 81 (4):2154–2162, 2001.

[88] C. Hiergeist, V. A. Indrani, and R. Lipowsky. Membranes with anchored polymers at the adsorption transition. *Europhys. Lett.*, 36(7):491, 1996.

[89] M. Breidenich, R. R. Netz, and R. Lipowsky. Adsorption of polymers anchored to membranes. *Euro. Phys. J. E*, 5(4):403–414, 2001.

[90] H. G. Döbereiner, A. Lehmann, W. Goedel, O. Selchow, and R. Lipowsky. Membrane curvature induced by sugar and polymer solutions. In *Mat. Res. Soc. Symp. Proc.*, volume 489, pages 101–106. Cambridge Univ Press, 1998.

[91] H. E. Warriner, S. H. J. Idziak, N. L. Slack, P. Davidson, and C. R. Safinya. Lamellar biogels: fluid-membrane-based hydrogels containing polymer lipids. *Science*, pages 969–972, 1996.

[92] U. Seifert. Configurations of fluid membranes and vesicles. *Adv. Phys.*, 46(1): 13–137, 1997.

[93] S. A. Safran. *Statistical Thermodynamics of Surfaces, Interfaces, and Membranes*. Addison-Wesley Reading, MA, 1994.

[94] M. Müller, K. Katsov, and M. Schick. Biological and synthetic membranes: What can be learned from a coarse-grained description? *Phys. Rep.*, 434(5):113–176, 2006.

[95] K. V. Damodaran, K. M. Merz Jr, and B. P. Gaber. Structure and dynamics of the dilauroylphosphatidylethanolamine lipid bilayer. *Biochemistry*, 31(33):7656–7664, 1992.

[96] H. Heller, M. Schaefer, and K. Schulten. Molecular dynamics simulation of a bilayer of 200 lipids in the gel and in the liquid crystal phase. *J. Phys. Chem.*, 97 (31):8343–8360, 1993.

[97] D. Frenkel and B. Smit. Understanding molecular simulation: from algorithms to applications, 2nd ed. 2002.

[98] B. Smit, K. Esselink, P. A. J. Hilbers, N. M. Van Os, L. A. M. Rupert, and I. Szleifer. Computer simulations of surfactant self-assembly. *Langmuir*, 9(1): 9–11, 1993.

[99] R. Goetz and R. Lipowsky. Computer simulations of bilayer membranes: Self-assembly and interfacial tension. *J. Chem. Phys.*, 108:7397, 1998.

[100] R. Goetz, G. Gompper, and R. Lipowsky. Mobility and elasticity of self-assembled membranes. *Phys. Rev. Lett.*, 82(1):221–224, 1999.

[101] H. Noguchi and M. Takasu. Self-assembly of amphiphiles into vesicles: A brownian dynamics simulation. *Phys. Rev. E*, 64(4):041913, 2001.

[102] H. Noguchi and M. Takasu. Fusion pathways of vesicles: a brownian dynamics simulation. *J. Chem. Phys.*, 115:9547, 2001.

[103] G. Gompper and H. Noguchi. *Coarse-grained and Continuum Models of Membranes*. 37th IFF Spring School: Computational Methods in Condensed Matter Physics, Forschungszentrum Jlich GmbH, 2006.

[104] G. Gompper and D. M. Kroll. Triangulated-surface models of fluctuating membranes. In D. R. Nelson, T. Piran, and S. Weinberg, editors, *Statistical Mechanics of Membranes and Surfaces*. World Scientific, Singapore, 2nd edition, 2004.

[105] H. Noguchi and G. Gompper. Shape transitions of fluid vesicles and red blood cells in capillary flows. *Proc. Natl. Acad. Sci. USA*, 102(40):14159–14164, 2005.

[106] H. Noguchi and G. Gompper. Swinging and tumbling of fluid vesicles in shear flow. *Phys. Rev. Lett.*, 98(12):128103, 2007.

[107] H. Noguchi and G. Gompper. Dynamics of fluid vesicles in shear flow: Effect of membrane viscosity and thermal fluctuations. *Phys. Rev. E*, 72(1):011901, 2005.

[108] H. Noguchi and G. Gompper. Fluid vesicles with viscous membranes in shear flow. *Phys. Rev. Lett.*, 93(25):258102, 2004.

[109] M. Doi. *The Theory of Polymer Dynamics.*, volume 73. oxford university press, 1988.

[110] M. Doi. *Introduction to Polymer Physics*. Oxford University Press on Demand, 1996.

[111] D. A. McQuarrie and J. D. Simon. *Physical Chemistry: A Molecular Approach*. University Science Books, 1997.

[112] M. P. Allen and D. J. Tildesley. *Computer Simulation of Liquids*. Clarendon Press, Oxford, 1987.

[113] P. G. de Gennes. Conformations of polymers attached to an interface. *Macromolecules*, 13(5):1069–1075, 1980.

[114] K. Binder. *Phase Transitions and Critical Phenomena*, volume 8. Academic, New York, 1983.

[115] T. Auth. *Effective Curvature Elastic Constants for Membrane-Polymer Systems*. PhD thesis, Universität zu Köln, 2003.

[116] M. Deserno. Mesoscopic membrane physics: concepts, simulations, and selected applications. *Macromol. rapid comm.*, 30(9-10):752–771, 2009.

[117] H. Shiba and H. Noguchi. Estimation of the bending rigidity and spontaneous curvature of fluid membranes in simulations. *Phys. Rev. E*, 84(3):031926, 2011.

[118] H. Noguchi. Structure formation in binary mixtures of surfactants: vesicle opening-up to bicelles and octopus-like micelles. *Soft Matter*, 8(34):8926–8935, 2012.

[119] M. Hu, J. J. Briguglio, and M. Deserno. Determining the gaussian curvature modulus of lipid membranes in simulations. *Biophys. J.*, 102(6):1403–1410, 2012.

[120] M. Hu, D. H. de Jong, S. J. Marrink, and M. Deserno. Gaussian curvature elasticity determined from global shape transformations and local stress distributions: a comparative study using the martini model. *Faraday Discuss.*, 161:365–382, 2013. doi: 10.1039/C2FD20087B.

[121] M. J. Uline and I. Szleifer. Mode specific elastic constants for the gel, liquid-ordered, and liquid-disordered phases of dppc/dopc/cholesterol model lipid bilayers. *Faraday Discuss.*, 161:177–191, 2013. doi: 10.1039/C2FD20091K.

[122] D. P. Siegel. The gaussian curvature elastic energy of intermediates in membrane fusion. *Biophys. J.*, 95(11):5200–5215, 2008.

[123] M. J. Bruno, R. Rusinova, N. J. Gleason, R. E. Koeppe II, and O. S. Andersen. Interactions of drugs and amphiphiles with membranes: modulation of lipid bilayer elastic properties by changes in acyl chain unsaturation and protonation. *Faraday Discuss.*, 161:461–480, 2013. doi: 10.1039/C2FD20092A.

[124] H. Noguchi. Anisotropic surface tension of buckled fluid membrane. *Phys. Rev. E*, 83:061919, 2011.

[125] V. A. Harmandaris and M. Deserno. A novel method for measuring the bending rigidity of model lipid emmbranes by simulating tethers. *J. Chem. Phys.*, 125: 204905, 2006.

[126] I. Tsafrir, D. Sagi, T. Arzi, M.-A. Guedeau-Boudeville, V. Frette, D. Kandel, and J. Stavans. Pearling instabilities of membrane tubes with anchored polymers. *Phys. Rev. Lett.*, 86(6):1138, 2001.

[127] F. Campelo and A. Hernández-Machado. Polymer-induced tubulation in lipid vesicles. *Phys. Rev. Lett.*, 100(15):158103, 2008.

[128] T. V. Tolpekina, W. K. den Otter, and W. J. Briels. Simulations of stable pores in membranes: System size dependence and line tension. *J. Chem. Phys.*, 121:8014, 2004.

[129] B. J. Reynwar and M. Deserno. Membrane composition-mediated protein-protein interactions. *Biointerphases*, 3(2):FA117–FA124, 2008.

[130] C. Vanderzande. *Lattice Models of Polymers*, volume 11. Cambridge University Press, 1998.

[131] A. R. Honerkamp-Smith, P. Cicuta, M. D. Collins, S. L. Veatch, M. den Nijs, M. Schick, and S. L. Keller. Line tensions, correlation lengths, and critical exponents in lipid membranes near critical points. *Biophys. J.*, 95(1):236–246, 2008.

[132] T. Baumgart, B. R. Capraro, C. Zhu, and S. L. Das. Thermodynamics and mechanics of membrane curvature generation and sensing by proteins and lipids. *Annu. Rev. Phys. Chem.*, 62:483–507, 2010.

[133] R. Phillips, T. Ursell, P. Wiggins, and P. Sens. Emerging roles for lipids in shaping membrane-protein function. *Nature*, 459:379–385, 2009.

[134] A. V. Shnyrova, V. A. Frolov, and J. Zimmerberg. Domain-driven morphogenesis of cellular membranes. *Curr. Biology*, 19:R772–R780, 2009.

[135] I. Tsafrir, T. Sagi, D.and Arzi, M.-A. Guedeau-Boudeville, V. Frette, D. Kandel, and J. Stavans. Pearling instabilities of membrane tubes with anchored polymers. *Phys. Rev. Lett.*, 86:1138–1141, Feb 2001.

[136] K. Akiyoshi, A. Itaya, S. M. Nomura, N. Ono, and K. Yoshikawa. Induction of neuron-like tubes and liposome networks by cooperative e.ect of gangliosides and phospholipids. *FEBS Lett.*, 534:33–38, 2003.

[137] K. Guo, J. Wang, F. Qiu, H. Zhang, and Y. Yang. Shapes of fluid vesicles anchored by polymer chains. *Soft Matter*, 5(8):1646–1655, 2009. doi: 10.1039/B814503B.

[138] P. B. Warren. Dissipative particle dynamics. *Curr. Opin. Colloid Interface Sci.*, 3(6):620–624, 1998.

[139] R. D. Groot and P. B. Warren. Dissipative particle dynamics: Bridging the gap between atomistic and mesoscopic simulation. *J. Chem. Phys.*, 107:4423, 1997.

[140] S. Yamamoto, Y. Maruyama, and S. Hyodo. Dissipative particle dynamics study of spontaneous vesicle formation of amphiphilic molecules. *J. Chem. Phys.*, 116: 5842, 2002.

[141] J. C. Shillcock and R. Lipowsky. Equilibrium structure and lateral stress distribution of amphiphilic bilayers from dissipative particle dynamics simulations. *J. Chem. Phys.*, 117:5048, 2002.

[142] N. A. Spenley. Scaling laws for polymers in dissipative particle dynamics. *Europhys. Lett.*, 49(4):534, 2000.

[143] A. Malevanets and R. Kapral. Mesoscopic model for solvent dynamics. *J. Chem. Phys.*, 110:8605, 1999.

[144] A. Malevanets and J. M. Yeomans. Dynamics of short polymer chains in solution. *Europhys. Lett.*, 52(2):231, 2000.

[145] R. Kapral. Multiparticle collision dynamics: simulation of complex systems on mesoscales. *Adv. Chem. Phys.*, 140:89, 2008.

[146] H. Noguchi, N. Kikuchi, and G. Gompper. Particle-based mesoscale hydrodynamic techniques. *Europhys. Lett.*, 78(1):10005, 2007.

[147] G. Gompper, T. Ihle, D. M. Kroll, and R. G. Winkler. Multi-particle collision dynamics: a particle-based mesoscale simulation approach to the hydrodynamics of complex fluids. *Adv. Polym. Sci.*, 221:1–87, 2009.

[148] E. de Miguel and G. Jackson. The nature of the calculation of the pressure in molecular simulations of continuous models from volume perturbations. *J. Chem. Phys.*, 125:164109, 2006.

Publications

[1] Hao Wu and Hiroshi Noguchi, Effects of anchored flexible polymers on mechanical properties of model biomembranes. AIP Conf. Proc. 1518, pp. 649-653 (2013).

[2] Hao Wu, Hayato Shiba, and Hiroshi Noguchi, Mechanical properties and microdomain separation of fluid membranes with anchored polymers. Soft Matter (2013), DOI: 10.1039/C3SM51680F.